Challenges in dye-sensitised solar cells: a theoretical study

Umberto Terranova

Department of Physics and Astronomy, UCL
A thesis submitted for the degree of PhD

To my family, once again

To Giulia. Until recently I did not imagine I would add this line for someone

I, Umberto Terranova, confirm that the work presented in this thesis is my own. Where information has been derived from other sources, I confirm that this has been indicated in the thesis.

Acknowledgments

I would like to express my deep gratitude to David Bowler, my supervisor. The countless meetings held have been a source of clarifications and new ideas. I am indebted to Angelos Michaelides, my second supervisor, for his continuous support during these years. I feel pleased to have worked closely with Conn O'Rourke, to whom I am very appreciative. I finally thank Lianheng Tong for his precious help with CONQUEST, and Yoshitaka Tateyama, Masato Sumita, and Chunping Hu for the stimulating discussions in Tsukuba.

Abstract

Up to now, the market of solar cells has been dominated by the conventional silicon devices. Recently, a new class of solar cells, known as dye-sensitised solar cells (DSSCs) have emerged. They are based on the hybrid chromophore/TiO_2 semiconductor interface, and the low cost of manufacturing and the flexibility make them a very promising alternative to the traditional silicon cells.

With this thesis, we aim at investigating theoretically, by means of density functional theory atomistic simulations, some of the current challenges in DSSCs. In particular, we will focus on the binding mode of the most common anchoring groups to TiO_2, the coating of TiO_2 with a second oxide such as Al_2O_3 to increase the efficiency, the issues related to the island growth mode during the atomic layer deposition of Al_2O_3 on TiO_2, and the use of the Δ self-consistent field method for the excitations of natural anthocyanidins.

The idea is to provide experimentalists with useful guidelines for the design of devices with improved efficiencies.

Contents

List of Publications

- "Adsorption of catechol on TiO_2 rutile (100): a density functional theory investigation",
  U. Terranova and D. R. Bowler, *J. Phys. Chem. C*, **114**, (2010), 6491-6495

- "Effect of hydration of the TiO_2 anatase (101) substrate on the atomic layer deposition of alumina films",
  U. Terranova and D. R. Bowler, *J. Mater. Chem.*, **21**, (2011) 4197-4203

- "Coating TiO_2 anatase by amorphous Al_2O_3: effects on dyes anchoring through carboxyl groups",
  U. Terranova and D. R. Bowler, *J. Phys. Chem. C*, **116**, (2012), 4408-4415

- "Excitations of natural anthocyanidins by Δ self-consistent field",
  U. Terranova and D. R. Bowler (to be submitted).

List of Figures

List of Tables

Chapter 1

Dye-sensitised solar cells

While the awareness that fuel reserves could finish in the next decades is spreading more and more within the scientific community, it is undoubtedly recognised that the solar supply of energy is by far more than the current human requirements. To satisfy our energy needs, it would be "sufficient" to cover the 0.1% of the earth's surface with solar cells with an efficiency of 10% [1].

The production of solar cells has increased by 30% per annum over the past 15 years [2]. Up to now, the market has been dominated by the conventional first and second generation of solar cells, based respectively on crystalline silicon and semiconductor thin films [3, 4], with efficiencies up to 30 and 20% [5].

Among the new photovoltaic technologies, dye-sensitised solar cells (DSSCs) are most promising [6]. In a DSSC, the process of charge generation and that of charge transport are separate. The first is done by a sensitiser absorbing in the visible, which injects the charge into the semiconductor, while the second is done by the semiconductor and the electrolyte. The separation allows the use of photostable semiconductors (TiO_2, ZnO, SnO_2), which, because of their wide band gaps, are insensitive to the visible solar spectrum.

Despite the low cost of materials and manufacturing makes DSSCs a potential third generation of solar cells, they suffer from efficiencies which are still around 10%. With this thesis, we aim at a theoretical investigation of some

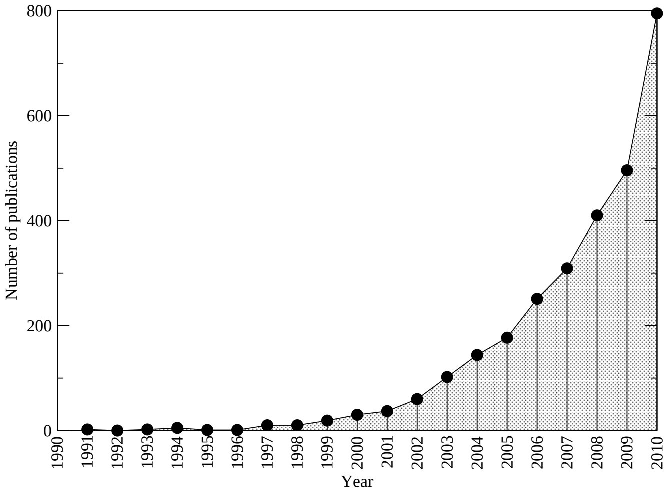

Figure 1.1: Number of publications per year obtained from a literature search using the string "dye-sensitized solar cells".

of the current challenges in DSSCs, with the idea of providing experimentalists with useful guidelines for the design of devices with improved efficiencies.

1.1 Principle of operation

Attempts to develop DSSCs with smooth semiconductor surfaces had already appeared in literature before 1991 [7,8]. However, it was only in that year that the introduction of a high surface area mesoporous TiO_2 film, by O'Regan and Grätzel, boosted the efficiency by an order of magnitude [6]. Since then, the research in the field has grown very rapidly, as evidenced from Figure 1.1, where the number of publications per year obtained from a literature search using the string "dye-sensitized solar cells" is reported.

A schematic with the components of a DSSC is shown in Figure 1.2. The key element is a mesoporous layer of TiO_2 nanoparticles. These are deposited on a mechanical support of glass coated with a transparent conducting oxide (TCO) acting as the anode. A monolayer of a dye is adsorbed on the nanoparticles, which are permeated by an electrolyte solution containing a redox couple, usually the iodide/triiodide couple (I^-/I_3^-), and acetonitrile (CH_3CN) as solvent. The cell is completed by a second conducting glass substrate, coated with a thin layer of platinum catalyst.

Following the photoexcitation of the dye (Figure 1.3, reaction 1), one electron is injected into the conduction band (CB) of TiO_2 (Figure 1.3, reaction 2). This mechanism of electron transfer is known in literature as type I. Another type II mechanism is however possible, in which the injection is direct from the dye to the CB of the semiconductor. Once injected into TiO_2, the electron can recombine with the oxidised dye (Figure 1.3, reaction 4) or with I_3^- in the electrolyte (Figure 1.3, reaction 5). Both pathways represent a loss of efficiency and recombinations at the TiO_2/dye and TiO_2/electrolyte must be minimised. After flowing through the nanoparticles and reaching the anode, the electrons produce some work at the external load and are collected at the cathode. The oxidised dye is restored to its original state by the electrolyte (Figure 1.3, reaction 3), while the I_3^- is in turn reduced to I^- by the electrons at the cathode, completing the regenerative cycle.

Under illumination, the open-circuit photovoltage V_{oc} is determined by the difference between the quasi-Fermi level E_{fn} of TiO_2 and the electrochemical potential μ of the redox couple (with the vacuum as a reference value):

$$eV_{\mathrm{oc}} = E_{\mathrm{fn}} - \mu(\mathrm{I}_3^-/\mathrm{I}^-). \tag{1.1}$$

The electrochemical potential of a (one electron) redox couple can be expressed as [9]:

$$\mu = \mu^0 + kT \ln\left(\frac{c_{\mathrm{ox}}}{c_{\mathrm{red}}}\right), \tag{1.2}$$

where μ^0 is the standard electrochemical potential of the redox system, and c_{ox} and c_{red} are the concentrations of the two oxidised and reduced species

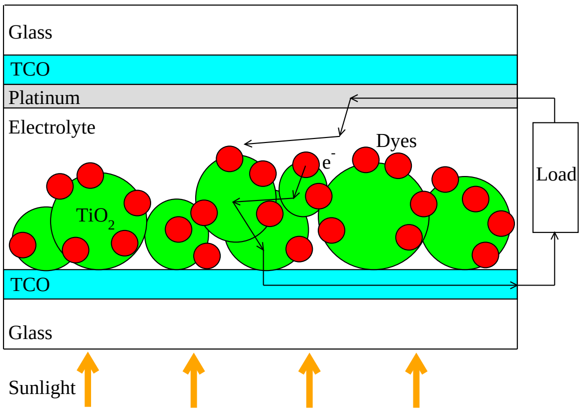

Figure 1.2: Schematic view of a DSSC.

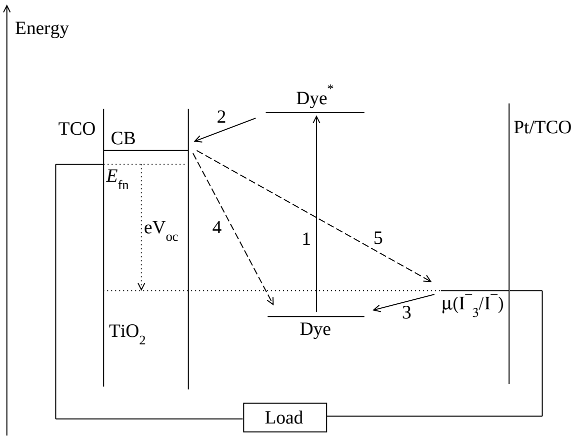

Figure 1.3: Schematic energy level diagram of a type I DSSC. The desired electron transfer reactions are indicated by full arrows (1: dye excitation; 2: electron injection; 3: dye reduction), the undesired by dashed arrows (4: recombination with the dye; 5: recombination with the electrolyte). The open-circuit photovoltage V_{oc} is also shown.

respectively. The solvent, impacting on μ^0, c_{ox}, and c_{red}, can influence the overall μ. In addition, once coadsorbed on the dye-sensitised system, solvent molecules can shift the edge of the $\mathrm{TiO_2}$ CB, and thus altering E_{fn}, through a dipole moment-modulated mechanism [10].

The photocurrent density measured at short-circuit (i.e. when the voltage drop across the solar cell is zero), J_{sc}, is given by:

$$J_{\mathrm{sc}} = \int e\Phi(\lambda)a(\lambda)\phi_{\mathrm{inj}}\phi_{\mathrm{c}}d\lambda, \tag{1.3}$$

where e is the electron charge, $\Phi(\lambda)$ the photon flux that strikes the cell at wavelength λ, $a(\lambda)$ the absorbivity of the dye-sensitised film, and ϕ_{inj} and ϕ_{c} are respectively the injection and the collection efficiency of the electron.

The overall conversion efficiency η of a DSSC is defined by:

$$\eta = \frac{J_{\mathrm{sc}}V_{\mathrm{oc}}\mathrm{FF}}{I}, \tag{1.4}$$

where I is the intensity of the incident light. If P_{max} is the maximum power of the cell per unit area, the fill factor FF, with values bewteen 0 and 1, is defined by:

$$\mathrm{FF} = \frac{P_{\mathrm{max}}}{J_{\mathrm{sc}}V_{\mathrm{oc}}}. \tag{1.5}$$

Another important parameter of a DSSC is its incident photon to current efficiency (IPCE(λ)), i.e. the photocurrent density $J_{\mathrm{sc}}(\lambda)$ produced under monochromatic illumination of wavelength λ divided by the photon flux $\Phi(\lambda)$ that strikes the cell:

$$\mathrm{IPCE}(\lambda) = \frac{J_{\mathrm{sc}}(\lambda)}{e\Phi(\lambda)}. \tag{1.6}$$

1.2 Surfaces and dyes

The nanoparticles employed in DSSCs are usually a mix of the anatase and rutile forms of TiO_2, in a proportion of 4:1. The preference for anatase is due to the larger surface to volume ratio of anatase nanoparticles, as well as the higher CB edge of anatase, which allows larger photovoltages to be achieved than in rutile.

Large anatase crystals are more difficult to obtain than rutile, and consequently less understood. However, in the past few years, remarkable progress has been made. It is now established, for example, that the (101) is the most prevalent face of anatase, constituting more than 94% of the crystal surface [11, 12]. It has also been discovered that defects reside predominantly subsurface [13].

In spite of the traditional preference for anatase, rutile performances in DSSCs have been shown to be comparable [14]. The (110) plane of rutile is the most stable and investigated surface of TiO_2 [15, 16]. Its interaction with water, especially, has been a matter of controversy [17–20]. However, the (110) surface occurs only for about 60% of the crystal, with the remaining part covered equally by the (100) and (101) planes [21]. In order to advance the understanding of TiO_2 in DSSCs, it is therefore important to expand our knowledge of the dye/semiconductor interface also for these minor surfaces.

Based on the principle of operation of DSSCs, the ideal dye should present the following characteristics: an absorption spectrum which matches the solar radiation, a good affinity for the substrate, a quantum yield of unity for the electron injection into the oxide, and a stability after many years of exposure to the sun.

In order for the DSSC to be efficient, the dye must bind strongly to the substrate. The standard anchoring moieties for sensitisers are carboxyl (–COOH) groups, which can bind to TiO_2 in a monodentate or bridging mode. With the purpose of understanding the adsorption of larger chromophores, a significant amount of work has been done to reveal the binding modes of formic acid

(HCOOH) on TiO_2 [22–27].

The adsorption geometries and energies are influenced also by the surrounding solvent molecules. Water, for instance, always contained in a certain amount in DSSCs, can compete with the dye for the same TiO_2 anchoring site [28, 29].

Among the sensitisers, catechol has received considerable attention, mainly because one of the smallest and because it sensitises TiO_2 through a type II mechanism [30–38]. Like formic acid, it can bind both in a monodentate or bridging way via its hydroxyl groups and can be used as an efficient ligand for the attachment of larger dyes [39].

The best photovoltaic properties in DSSCs have been shown by the sensitisers of the class of ruthenium (Ru) complexes, such as the N3 [40], and the N749 dye (also known as “black dye”) [41]. With the latter, a certified record efficiency of 11.4% has recently been reached [42]. In spite of this, the high cost and the limited availability of ruthenium make desirable the use of cheaper dyes. Organic dyes fulfil this requirement, and efficiencies up to 11% have been recently achieved with their use [43]. However, the synthetic route of organic dyes remains expensive, and the disposal of by-products still needs to be addressed [44]. On the contrary, natural dyes are cheap, easy to obtain, and fully biodegradable. Among them, anthocyanins and anthocyanidins are phenolic compounds responsible for the colour of many fruits and vegetables (blueberries, onions, aubergines, amongst others). Since very common in nature, they have been traditionally employed in DSSCs, with low but promising efficiencies up to 1% [45–49].

1.3 Routes to the improvement

One problem of Ru complexes is the poor absorption in the infrared region of the solar spectrum, which results into a low IPCE in this wavelength range. Thus, one route to increase the efficiency is the synthesis of new dyes with improved absorption in the longer wavelength range [50].

Another challenging direction is the replacement of the traditional I^-/I_3^- redox couple with systems having a lower electrochemical potential, which would increase the open-circuit photovoltage V_{oc}. Towards this direction, redox couples based on Co [51], Cu [52], and organic radicals [53] have been explored.

A third route towards higher efficiencies is the coating of the TiO_2 film with an overlayer of a second oxide, such as Al_2O_3 [54–57], Nb_2O_5 [58, 59], MgO [60], $CaCO_3$ [61], and ZrO_2 [62]. The role played by the overlayer is still under debate and at least four mechanisms may take place, even simultaneously [55, 63–65]. Regardless of the mechanism, there is agreement on the finding that a coating which is too thick blocks the photocurrent, with a corresponding loss of efficiency. In order to optimise the efficiency then, it is necessary to employ an overlayer with an optimum thickness, and values ranging from 1 to 120 Å have been reported in the literature [66].

A possible way to grow an overlayer of Al_2O_3 on a nanocrystalline TiO_2 film is to make use of the surface sol-gel process [67]. With this technique, Palomares *et al* have reported an increase of 30% in the efficiency of DSSCs [55]. The sol-gel process, however, has a minimum achievable thickness of 10 Å, which gives poor control in the determination of the optimal thickness.

Compared to the sol-gel technique, atomic layer deposition (ALD) has a higher thickness resolution of 1 Å, and is in principle ideal to deposit uniform and monolayer Al_2O_3 films [68–73]. However, when Al_2O_3 ALD was employed to overcoat anatase nanoparticles in DSSCs, the increase of efficiency was only 14% [74]. The unsatisfactory results have been ascribed to the island growth mode [75], which causes a low coverage of the TiO_2 film after a few cycles of ALD. Understanding the growth mechanism of the Al_2O_3 overlayer is then an essential step towards further efficiency increases in DSSCs.

1.4 Outline of the thesis

The quantum chemistry approach behind our atomistic simulations is density functional theory (DFT). In chapter 2, we will briefly review its foundations and approximations for the modelling of the dye/surface interface in DSSCs. At this interface, we are aware of the relevant role of the solvent, and have mentioned some of the possible implications in sections 1.1 and 1.2. In our case, its inclusion would have tremendously increased the computational effort, making this work unfeasible. However, while we expect that some of the results would vary quantitatively if one took the solvent explicitely into account (e.g. adsorption energies, excitation energies, and DOS), we are confident that the qualitative conclusions that we have drawn at the end of each chapter would remain unaffected.

The strong affinity of catechol towards TiO_2 has suggested that new and more effective chromophores which bind through a catechol ring could be designed. To expand the knowledge of the catechol/TiO_2 interface, in chapter 3, we will characterise the adsorption of catechol on the oxide. We will employ both the minor (100) face of rutile, and the most exposed (101) face of anatase. After characterising both substrates by their surface formation energies and geometries, we will investigate the geometries, binding energies, and electronic structures of different binding modes of catechol.

To better understand the dye/Al_2O_3/TiO_2 interface, in chapter 4, we will investigate the adsorption of formic acid and catechol on TiO_2 anatase (101), addressing the effect of the Al_2O_3 overlayer on the efficiency of DSSCs. Moreover, we will show that the picture derived for formic acid can be extended to the larger N3 dye, binding through –COOH groups.

Since the knowledge of the growth mechanism of the Al_2O_3 overlayer is essential to improve the coverage of the TiO_2 film, in chapter 5, we will present an investigation of the first steps of Al_2O_3 ALD on anatase (101). By comparing the reaction pathways for the surface with those at defects, we capture important insights into the on-growing substrate, and provide a possible explanation to the incomplete coverage of the TiO_2 electrode.

In chapter 6, we will review the intuitive idea behind Δ self-consistent field (ΔSCF) [76, 77], one of the earliest methods for the calculation of excitation energies, which we have implemented in the CONQUEST code [78–80]. We will discuss the effect of hydroxy substitutions and pH on the lowest excitations of a number of anthocyanidins. To reproduce a typical DSSC interface, we will adsorb one anthocyanidin on TiO_2 anatase (101), focussing on the shift of the lowest excitation energy due to the adsorption. Finally, we will show that ΔSCF allows to relax the adsorbed dye in its excited state by simply taking the gradient of the ΔSCF state corresponding to the HOMO $\rightarrow$ LUMO excitation within the dye (HOMOdye $\rightarrow$ LUMOdye).

Chapter 2

Energy calculations

2.1 The many-body Schrödinger equation

The most accurate approach to understanding the behaviour of matter and its interaction with light is quantum mechanics (QM). In QM, given a system of M nuclei and N electrons, described respectively by the coordinates $\mathbf{R} \equiv \mathbf{R}_1, \ldots \mathbf{R}_M$ and $\mathbf{r} \equiv \mathbf{r}_1, \ldots, \mathbf{r}_N$, all the information is contained in the wavefunction $\Psi(\mathbf{r}, \mathbf{R})$ solution of the time-independent Schrödinger's equation (SE):

$$H\Psi(\mathbf{r}, \mathbf{R}) = E\Psi(\mathbf{r}, \mathbf{R}), \tag{2.1}$$

where the Hamiltonian is given by:

$$H = T_N + T_e + V_{ee}(\mathbf{r}) + V_{eN}(\mathbf{r}, \mathbf{R}) + E_{NN}(\mathbf{R}). \tag{2.2}$$

In Eq. 2.2, T_N and T_e are the nuclear and electron kinetic energy operators:

$$T_N = -\sum_{I=1}^{M} \frac{1}{2M_I} \nabla_I^2, \tag{2.3}$$

$$T_e = -\sum_{i=1}^{N} \frac{1}{2} \nabla_i^2, \tag{2.4}$$

where M_I is the ratio of the mass of the nucleus I to the mass of the electron, while $V_{ee}(\mathbf{r})$, $V_{eN}(\mathbf{r}, \mathbf{R})$, and $E_{NN}(\mathbf{R})$ are respectively the electron-electron, electron-nuclear, and nuclear-nuclear interaction potential operators:

$$V_{ee}(\mathbf{r}) = \sum_{i=1}^{N} \sum_{j>i}^{N} \frac{1}{|\mathbf{r}_i - \mathbf{r}_j|}, \tag{2.5}$$

$$V_{eN}(\mathbf{r}, \mathbf{R}) = -\sum_{i=1}^{N} \sum_{I=1}^{M} \frac{Z_I}{|\mathbf{r}_i - \mathbf{R}_I|}, \tag{2.6}$$

$$E_{NN}(\mathbf{R}) = \sum_{I=1}^{M} \sum_{J>I}^{M} \frac{Z_I Z_J}{|\mathbf{R}_I - \mathbf{R}_J|}, \tag{2.7}$$

where Z_I is the charge of the nucleus I.

The Hamiltonian defined by Eq. 2.2 is universal, and if we were able to solve the SE (Eq. 2.1), then we would recover the stationary states and energies of the system. Unfortunately, Eq. 2.1 is impossible to solve exactly, and a series of approximations are necessary.

2.2 The Born-Oppenheimer approximation

The Born-Oppenheimer (BO) is the first among the approximations discussed in this chapter. It is based on the observation that nuclei are much heavier than electrons, hence one can consider the electrons to relax very rapidly in the field generated by the static nuclei. Within this approximation, in Eq. 2.2, the kinetic energy T_N can be neglected, and the repulsion E_{NN} can be considered to be a constant. The remaining terms of Eq. 2.2 form the electronic Hamiltonian

$$H_{el}(\mathbf{r}, \mathbf{R}) \equiv T_e + V_{ee}(\mathbf{r}) + V_{eN}(\mathbf{r}, \mathbf{R}). \tag{2.8}$$

The solution of the SE for the electronic Hamiltonian,

$$H_{el}(\mathbf{r}, \mathbf{R})\psi_n(\mathbf{r}, \mathbf{R}) = \varepsilon_n(\mathbf{R})\psi_n(\mathbf{r}, \mathbf{R}), \tag{2.9}$$

are the electronic wavefunctions, depending, as the electronic energies, only parametrically on the nuclear positions.

As the electrons move on a shorter time scale than nuclei, it makes sense to replace the electronic coordinates in Eq. 2.2 by the values averaged over the electronic wavefunction $\psi_n(\mathbf{r}, \mathbf{R})$. This generates a nuclear Hamiltonian, which describes the motion of the nuclei in the average field of the electrons:

$$H_N(\mathbf{R}) \equiv T_N + E_{NN}(\mathbf{R}) + \varepsilon_n(\mathbf{R}). \tag{2.10}$$

Eq. 2.10 shows that the nuclei move in potential energy surfaces $E_{NN}(\mathbf{R}) + \varepsilon_n(\mathbf{R})$, set up by the electrons, and known as BO surfaces. Thus, the many-electron problem defined by Eq. 2.9 is of utmost importance in quantum chemistry.

2.3 One-electron methods

The solution of the SE for a system of N interacting electrons in a field created by M nuclei is a very difficult problem, which makes necessary to simplify Eq. 2.9. The first approximation, proposed by Hartree, postulated that the electronic wavefunction could be written as the product of one-electron wavefunctions [81]. Each of them satisfies a single-particle SE with an effective potential that takes into account the interaction with the nuclei and the other electrons in a mean-field way.

The Hartree approximation can be improved by introducing the Pauli exclusion principle, which demands that the many-electron wavefunction be antisymmetric with respect to interchange of any two electron coordinates. This can be achieved using an antisymmetrised wavefunction resulting from a Slater determinant, within the Hartree-Fock (HF) approximation [82]. The single-particle HF equations are derived from minimisation of the total energy with respect to the HF orbitals. They include an integral involving only orbitals of the same spin, the so-called exchange term operator, which adds a lot of complexity to the problem. Although many-body correlations are completely neglected, HF is used as a starting point for more accurate approaches where the electronic wavefunction is given by a linear combination of Slater determinants [83].

2.4 Basics of DFT

Rather than using the many-electron wavefunction, DFT tackles the SE 2.9 with the electron density

$$n(\mathbf{r}) = N \int d\mathbf{r}_2 \dots \int d\mathbf{r}_N |\psi(\mathbf{r}, \mathbf{r}_2, \dots \mathbf{r}_N)|^2 \tag{2.11}$$

as the key variable. Thanks to the scheme proposed by Kohn and Sham, which transforms the original many-body problem into an auxiliary independent-particle problem, DFT is today the most popular method to calculate properties of matter.

2.4.1 The Hohenberg and Kohn theorems

The modern formulation of DFT was started by Hohenberg and Kohn [84]. Their two seminal theorems, whose proofs are available in the original paper, can be formulated as follows:

1. The external potential due to the nuclei, $V_{\text{ext}}(\mathbf{r})$, felt by an arbitrary number of electrons N in a large box, is uniquely determined, apart from a trivial additive constant, by the ground state electron density $n_0(\mathbf{r})$. Thus, since $V_{\text{ext}}(\mathbf{r})$ fixes the Hamiltonian, the full many-particle ground state is a unique functional of $n_0(\mathbf{r})$.

2. For a given external potential $V_{\text{ext}}(\mathbf{r})$, an energy functional can be defined

in terms of the density:

$$E[n] = \int V_{\text{ext}}(\mathbf{r})n(\mathbf{r})d\mathbf{r} + F[n] + E_{NN}, \tag{2.12}$$

where

$$F[n] = T[n] + E_{\text{int}}[n] \tag{2.13}$$

includes the kinetic energy $T[n]$, and the interaction energy of the electrons $E_{\text{int}}[n]$. $F[n]$ is a universal functional valid for any number of particles and any external potential. $E[n]$ assumes its minimum value, corresponding to the ground state energy of the system, for the correct density $n_0(\mathbf{r})$. If the form of $F[n]$ was known, the problem of determining the ground state energy and density could be solved rather easily by minimising $E[n]$.

2.4.2 The Kohn-Sham scheme

Kohn and Sham carried further the approach developed with the two previous theorems, replacing the many-electron problem with a set of self-consistent and single-particle equations. In the Kohn-Sham (KS) formulation of DFT [85], we assume the existence of an auxiliary system of N non-interacting electrons, subject to a local effective potential $V_{\text{KS}}(\mathbf{r})$ yielding the same ground state density as that of the interacting electronic system. Then, we express the energy functional of the interacting system in the form:

$$E_{\text{KS}}[n] = T_s[n] + \int n(\mathbf{r})V_{\text{ext}}(\mathbf{r})d\mathbf{r} + E_{\text{H}}[n] + E_{\text{xc}}[n] + E_{NN}. \tag{2.14}$$

In Eq. 2.14, T_s is the kinetic energy of the non-interacting reference system (which must be a unique functional of $n(\mathbf{r})$ by the application of the Hohenberg-

Kohn theorems to the auxiliary system):

$$T_s = -\frac{1}{2}\sum_{i=1}^{N}\langle\psi_i|\nabla^2|\psi_i\rangle, \tag{2.15}$$

E_{H} represents the classical Coulomb self-energy:

$$E_{\mathrm{H}}[n] = \frac{1}{2}\int d\mathbf{r}d\mathbf{r}'\frac{n(\mathbf{r})n(\mathbf{r}')}{|\mathbf{r}-\mathbf{r}'|}, \tag{2.16}$$

and the last term, E_{xc}, defines the exchange and correlation energy. E_{xc} is a unique functional of the density by construction and encloses all the many body effects of exchange and correlation. It is the only term of Eq. 2.14 which can not be evaluated exactly, and we will discuss some approximations in subsection 2.4.3.

The variational principle applied to Eq. 2.14, with the requirement of a constant particle number N associated with the Lagrange multiplier μ, yields:

$$\frac{\delta E_{\mathrm{KS}}}{\delta n(\mathbf{r})} = \frac{\delta T_s}{\delta n(\mathbf{r})} + V_{\mathrm{ext}}(\mathbf{r}) + V_{\mathrm{H}}(\mathbf{r}) + V_{\mathrm{xc}}(\mathbf{r}) = \mu, \tag{2.17}$$

where

$$V_{\mathrm{H}}(\mathbf{r}) = \frac{\delta E_{\mathrm{H}}}{\delta n(\mathbf{r})}, \tag{2.18}$$

and

$$V_{\mathrm{xc}}(\mathbf{r}) = \frac{\delta E_{\mathrm{xc}}}{\delta n(\mathbf{r})}. \tag{2.19}$$

The same equation for the non-interacting system is:

$$\frac{\delta E_{\mathrm{KS}}}{\delta n(\mathbf{r})} = \frac{\delta T_s}{\delta n(\mathbf{r})} + V_{\mathrm{KS}}(\mathbf{r}) = \mu. \tag{2.20}$$

Since the two problems present the same solution if

$$V_{\mathrm{KS}}(\mathbf{r}) = V_{\mathrm{ext}}(\mathbf{r}) + V_{\mathrm{H}}(\mathbf{r}) + V_{\mathrm{xc}}(\mathbf{r}), \tag{2.21}$$

the ground state density $n(\mathbf{r})$ can be found by solving the SEs for the non-interacting particles,

$$H_{\mathrm{KS}}\psi_i(\mathbf{r}) = \left[-\frac{1}{2}\nabla^2 + V_{\mathrm{KS}}(\mathbf{r}) \right] \psi_i(\mathbf{r}) = \varepsilon_i \psi_i(\mathbf{r}), \tag{2.22}$$

and taking sum of the squares of the N orbitals with the lowest eigenvalues ε_i:

$$n(\mathbf{r}) = \sum_{i}^{N} |\psi_i(\mathbf{r})|^2. \tag{2.23}$$

Since $V_{\mathrm{KS}}(\mathbf{r})$ is a functional of the density, the KS equations 2.21–2.23 must be solved in a self-consistent way. Usually, one starts supplying some model density, constructs $V_{\mathrm{KS}}(\mathbf{r})$ from Eq. 2.21, solves Eq. 2.22, and finds a new $n(\mathbf{r})$ from Eq. 2.23. The new density can be used to restart the cycle until a desired convergence is reached. In the simplest linear mixing scheme, the density supplied to the new cycle is a linear combination between the density resulting from Eq. 2.23 and the density of the previous iteration. Yet, more elaborated approaches can be used, in which the new density is formed by taking into account previous densities from several steps [86]. In principle, the final solution should be independent from the initial guess of the density, however, an accurate initial guess can speed up the computational time considerably. For example, for a molecule or a solid state system, a convenient starting density is given by the sum of the atomic densities of the system.

If the exact form of the exchange and correlation energy was known, the solution of the KS equations 2.21–2.23 would lead to the exact ground state energy and density of the interacting system. Since this is not the case, E_{xc} must be approximated by some functional of the density.

2.4.3 Approximations for E_{xc}

In their seminal paper, Kohn and Sham proposed the local density approximation (LDA) for the exchange and correlation energy: at each point $\mathbf{r}$ with density $n(\mathbf{r})$, the exchange and correlation energy per electron, $\epsilon_{\mathrm{xc}}(\mathbf{r})$, is approximated to that of a homogeneous electron gas with the same density, $\epsilon_{\mathrm{xc}}^{\mathrm{hom}}(n)$. The exchange and correlation energy $E_{\mathrm{xc}}^{\mathrm{LDA}}$ is simply an integral over all space:

$$E_{\mathrm{xc}}^{\mathrm{LDA}}[n] = \int d\mathbf{r} n(\mathbf{r}) \epsilon_{\mathrm{xc}}^{\mathrm{hom}}(n) = \int d\mathbf{r} n(\mathbf{r}) \Big(\epsilon_{\mathrm{x}}^{\mathrm{hom}}(n) + \epsilon_{\mathrm{c}}^{\mathrm{hom}}(n) \Big) \tag{2.24}$$

The exchange term $\epsilon_{\mathrm{x}}^{\mathrm{hom}}(n)$ can be expressed in a simple analytic form [83], while the correlation $\epsilon_{\mathrm{c}}^{\mathrm{hom}}(n)$ has been accurately tabulated for several densities using Monte Carlo methods [87], so that a fit can be made.

An obvious approach to improving the LDA is to include gradient corrections, by making E_{xc} a functional of the density and its gradient:

$$E_{\mathrm{xc}}^{\mathrm{GGA}}[n] = \int d\mathbf{r} n(\mathbf{r}) F_{\mathrm{xc}}[n(\mathbf{r}), \nabla n(\mathbf{r})] \tag{2.25}$$

Depending on the form of $F_{\mathrm{xc}}[n, \nabla n]$, one can obtain different generalised-gradient approximations (GGAs). The most common GGAs are the parameter free PBE [88] and PW91 [89], and the empirical BLYP [90].

A different class of functionals are called hybrid, because they mix a fraction of exact exchange used in HF theory (except KS rather than HF orbitals are used) into DFT exchange functionals [91, 92]. A popular hybrid functional is B3LYP, which combines the LYP GGA for correlation [93] with the B3 functional for exchange [94]. Due to the exchange term, calculations with hybrid functionals are more expensive compared to LDA and GGA. The most important success of hybrid functionals is in the prediction of the excitation energies.

2.4.4 Calculation of forces

The force on the nucleus I, $\mathbf{F}_I$, is given by minus the derivative of the total energy with respect to the position of the nucleus:

$$\mathbf{F}_I = -\frac{dE}{d\mathbf{R}_I}. \tag{2.26}$$

The DFT expression for forces contains a term coming from explicit derivation of the energy functional of Eq. 2.12 with respect to the nuclei positions, and a term coming from implicit dependence via the functional derivative of the charge density:

$$\mathbf{F}_I = -\frac{\partial E_{\mathrm{KS}}}{\partial \mathbf{R}_I} - \int \frac{\delta E_{\mathrm{KS}}}{\delta n} \frac{\partial n(\mathbf{r})}{\partial \mathbf{R}_I} d\mathbf{r}. \tag{2.27}$$

However, for the ground state charge density, the second term of Eq. 2.27 vanishes exactly: the functional derivative of E equals a constant (Eq. 2.17) and the remaining integral is zero because of charge conservation.

Since the only terms that depend explicitly upon the positions of the nuclei in Eq. 2.14 are the external potential $V_{\mathrm{ext}}(\mathbf{r})$ and the repulsion E_{NN}, the force on the nucleus I is given by

$$\mathbf{F}_I = -\frac{\partial E_{\mathrm{KS}}}{\partial \mathbf{R}_I} = -\int n(\mathbf{r}) \frac{\partial V_{\mathrm{ext}}(\mathbf{r})}{\partial \mathbf{R}_I} d\mathbf{r} - \frac{\partial E_{NN}}{\partial \mathbf{R}_I}, \tag{2.28}$$

which is the Hellmann-Feynman force theorem.

In practical calculations, a correction term arises when the basis set is not complete and moves with the atoms. These contributions are called Pulay forces and must be computed explicitly [95].

2.5 Periodic solids

DFT replaces the many-electron SE with a system of single-particle KS equations. However, in a periodic solid, the number of electrons is infinite, and we need to make use of the Bloch's theorem to surmount this problem.

Bloch's theorem states that the solutions of the SE for an independent electron subject to an effective potential $V_{\text{eff}}(\mathbf{r})$ with the periodicity of the Bravais lattice,

$$H\psi(\mathbf{r}) \equiv \Big[-\frac{1}{2}\nabla^2 + V_{\text{eff}}(\mathbf{r})\Big]\psi(\mathbf{r}) = \varepsilon\psi(\mathbf{r}), \tag{2.29}$$

can be chosen to have the form of a phase times a function $u_{\mathbf{k}}(\mathbf{r})$ which has the periodicity of the potential:

$$\psi_{\mathbf{k}}(\mathbf{r}) = e^{i\mathbf{k}\cdot\mathbf{r}}u_{\mathbf{k}}(\mathbf{r}). \tag{2.30}$$

Moreover, by imposing periodic boundary conditions to Eq. 2.30, it is possible to show that $\mathbf{k}$ must be of the form:

$$\mathbf{k} = \frac{m_1}{N_1}\mathbf{b}_1 + \frac{m_2}{N_2}\mathbf{b}_2 + \frac{m_3}{N_3}\mathbf{b}_3, \tag{2.31}$$

where m_i are integers, $\mathbf{b}_i$ primitive vectors of the reciprocal lattice, and N_i the number of primitive cells in the crystal along the direction i.

If now we look for the solutions of the form 2.30 for Eq. 2.29, we find that $u_{\mathbf{k}}(\mathbf{r})$ is determined by the equation

$$H_{\mathbf{k}}u_{\mathbf{k}}(\mathbf{r}) = \left[\frac{1}{2}\left(\frac{1}{i}\nabla + \mathbf{k}\right)^2 + V_{\text{eff}}(\mathbf{r})\right]u_{\mathbf{k}}(\mathbf{r}) = \varepsilon_{\mathbf{k}}u_{\mathbf{k}}(\mathbf{r}). \tag{2.32}$$

As $u_{\mathbf{k}}(\mathbf{r})$ must be periodic, Eq. 2.32 can be solved restricted to a single primitive cell of the crystal. Because of the finite volume, for each $\mathbf{k}$-point, we therefore expect to find an infinite set of solutions with discretely spaced eigenvalues, labeled with the so-called band index n. On the contrary, the $\mathbf{k}$-points appear only as a parameter in the Hamiltonian 2.32, and the energy levels vary continuously with $\mathbf{k}$.

In a periodic solid, the problem of calculating an infinite number of wavefunctions can now by replaced by a one of calculating a finite number of wavefunctions at an infinite number of **k**-points. In theory, to compute the DFT ground state density, an integral over all the **k**-points is required. However, it is possible to approximate this integral by a sum at convenient **k**-points, and the error can be reduced by the use of a denser mesh of **k**-points. To this end, a very popular scheme is due to Monkhorst and Pack [96]. We mention that calculations are more difficult with metallic systems, where a finer **k**-point grid is necessary to obtain an accurate sampling of the Fermi surface.

DFT codes are usually developed in the three-dimensional periodic supercell approach. In order to study a surface, one has to construct a periodic array of slabs of a converged thickness, separated by a vacuum region. It is important for the latter to be large enough to avoid spurious interactions between replica atoms. Similarly, a molecule can be represented as a crystal whose unit cells do not interact with each other. When supercells are used to simulate surfaces or molecules, only one **k**-point is needed along the non-interacting direction.

2.6 Basis sets

The KS equations 2.21-2.23 are solved by expanding the orbitals into a convenient set of basis functions and diagonalising the matrix of the Hamiltonian, or minimising the KS energy functional (Eq. 2.14). The two most commonly employed basis sets in quantum chemistry codes are plane waves and atomic orbitals.

2.6.1 Plane waves

Plane waves are the basis set implemented in the DFT code VASP [97, 98]. As stated by the Bloch's theorem, the KS wavefunctions can be written as the product of a plane wave $e^{i\mathbf{k}\cdot\mathbf{r}}$ and a function $u_{\mathbf{k}}(\mathbf{r})$ with the periodicity of the lattice (Eq. 2.30). The latter can be expanded in a discrete set of plane waves whose wavevectors $\mathbf{G}$ belong to the reciprocal lattice:

$$u_{\mathbf{k}}(\mathbf{r}) = \sum_{\mathbf{G}} c_{\mathbf{k},\mathbf{G}} e^{i\mathbf{G}\cdot\mathbf{r}}, \tag{2.33}$$

Therefore, by making use of Eq. 2.33, the wavefunctions of Eq. 2.30 can be written as:

$$\psi_{\mathbf{k}}(\mathbf{r}) = \sum_{\mathbf{G}} c_{\mathbf{k},\mathbf{G}} e^{i(\mathbf{k}+\mathbf{G})\cdot\mathbf{r}}. \tag{2.34}$$

Even though in principle an infinite number of plane waves is needed in Eq. 2.34, the coefficients for the plane waves with small kinetic energy are more important. Therefore, the basis can be truncated to a finite number of plane waves with a kinetic energy less than a chosen cutoff. The truncation of the basis causes an error in the total energy, which however is possible to reduce by increasing the value of the cutoff until a desired convergence is reached.

Plane waves have some good features which make them the most natural choice in solid state physics. For example, they are orthogonal and treat all the points in the space with the same accuracy. In addition, Pulay forces vanish, because the basis does not depend on the nuclei positions (subsection 2.4.4).

2.6.2 Atomic orbitals

Atomic orbitals are a set of basis functions centred on the atom sites, usually split into a radial part and a spherical harmonic:

$$\phi_{nlm}(\mathbf{r}) = \chi_{nl}(r) Y_{lm}(\hat{\mathbf{r}}) \tag{2.35}$$

Due to their similarity to the atomic orbitals of hydrogen, Slater Type Orbitals (STOs) can be used as basis functions. They are described by:

$$S^{\zeta}_{nlm}(\mathbf{r}) = A r^{n-1} e^{-\zeta r} Y_{lm}(\hat{\mathbf{r}}), \tag{2.36}$$

where A is a normalisation factor and ζ is called the exponent. STOs can be approximated by Gaussian Type Orbitals (GTOs), which allow all the matrix elements to be calculated much faster. They are expressed as:

$$G_{ijk}^{\zeta}(\mathbf{r}) = Ae^{-\zeta r^2} x^i y^j z^k, \tag{2.37}$$

where the sum $l = i + j + k$ gives the angular momentum of the GTO.

The DFT code CONQUEST [78–80] is based on pseudoatomic orbitals (PAOs) following the format of the DFT code Siesta [99]. These are the solution of the KS equations for the isolated atoms, with the same exchange and correlation functional and pseudopotentials of the system of interest. PAOs are obtained by confining the isolated atoms within spherical potential wells, which ensures that the PAOs are zero beyond a given cutoff radius. A systematic way to define all the different cutoff radii is achieved by introducing the energy shift, i.e., the energy increase experienced by the PAOs because of the confinement.

The minimum basis set is given by the number of electrons in the system. However, to achieve reasonable accuracy, larger basis sets are needed. A first improvement can be obtained by adding a second radial function, with different ζ, to each orbital, i.e. by a double zeta (DZ) basis set. The quality of the basis set can be further improved by polarising the orbitals with the addition of functions of higher angular momentum. A standard basis set is "double-zeta plus polarisation" (DZP), where each strongly occupied valence orbital has two radial functions, and each weakly occupied orbital only one.

The advantage of atomic orbitals over plane waves is a much smaller basis set to obtain solutions of comparable quality. Moreover, atomic orbitals are localised, which avoids the use of the supercell approach for finite systems. For the same reason, the study of systems with the presence of vacuum is very convenient. The downside of atomic orbitals is that it is not straightforward to improve the basis set systematically, but more parameters must be optimised. Finally, unlike plane waves, atomic orbitals move with ions, and Pulay correction to the forces must be computed (subsection 2.4.4).

2.7 The pseudopotential approximation

We know that core electrons on different atoms are almost independent of the environment surrounding the atom and only valence electrons participate in the formation of chemical bonds. Following this intuitive idea, the pseudopotential approximation removes the core electrons and replaces their effect and the effect of nuclei by fictitious interactions, or pseudopotentials, acting on the valence electrons. By eliminating the core electrons, the pseudopotential approximation reduces the size of the basis set. It also avoids the use of a prohibitive number of plane waves to describe the oscillations of the valence electrons in the core region.

In practice, to obtain a pseudopotential it is necessary to solve the radial KS equations

$$\left[-\frac{1}{2}\frac{d^2}{dr^2}+\frac{l(l+1)}{2r^2}+V_{\mathrm{KS}}(r)\right]rR_{nl}(r)=\varepsilon_{nl}rR_{nl}(r) \tag{2.38}$$

for an atom in a particular electronic configuration, taking into account all electrons. Then, the pseudo-wavefunctions $R_l^{\mathrm{PP}}(r)$, determined according to specific requirements [100], are re-inserted into the KS equations which are now solved for the pseudopotentials.

The use of norm-conserving pseudopotentials and plane waves is problematic for materials such as the first-row elements (B, C, N, O, ...) and the transition metals (Ti, Fe, Cu, Zn, ...). Here, the pseudo and the nodeless all-electron wavefunctions almost match. Since the 2p and 3d valence electrons are strongly localised around the ion, a large number of plane waves is necessary to describe their pseudo-wavefunctions. The cutoff energy in the expansion may be reduced by increasing the cutoff radius r_l^{cut} beyond which the pseudo-wavefunction and the all-electron wavefunction match. This however reduces the accuracy, and it is not simple to satisfy these two conflicting requirements. Ultrasoft pseudopotentials tackle this problem by relaxing the norm-conserving requirement [101]. This allows the pseudo-wavefunctions to become much softer, and considerably fewer plane waves are needed.

Chapter 3

Catechol on TiO_2

3.1 Introduction

The nanoparticles employed in DSSCs are usually a mix of the anatase and rutile forms of TiO_2, in a proportion of 4:1. Despite the traditional preference for anatase, rutile is chemically more stable and potentially cheaper to produce. Moreover, rutile performances in DSSCs have been shown to be comparable to those of anatase at one sun light intensity [14].

The (110) plane is the most stable and investigated surface of rutile [15,16]. It covers the 64% of its surface, with the remaining part divided between the (100) and (101) planes [21]. It is therefore important to expand our knowledge of the dye/semiconductor interface also for these minor surfaces.

Using rutile (110) and (100) as a substrate for organic dyes, much larger IPCE values were obtained for the (100) plane than the (110) one, probably due to the larger surface density of anchoring Ti sites [102]. In line with this, in a different study with the N3 dye, the IPCE values on anatase (101) and rutile (100) have been found much higher than on anatase (001) and rutile (001) [103].

Among the many sensitisers, catechol, as one of the smallest, has received considerable attention [30–38]. In addition to being used as a dye, catechol can constitute an efficient anchoring group for the attachment of larger dyes.

For instance, IPCE values up to 50% have been achieved with Ru complexes containing a pendant catechol binding on TiO$_2$ [39].

The catechol/TiO$_2$ complex is an example of a type II mechanism. Despite its lowest excitation energy (4.1 eV) being larger than TiO$_2$ band gap, catechol shifts the absorption threshold of TiO$_2$ into the visible region (from 3.2 to 2.9 eV) [104, 105]. Semiempirical quantum chemical calculations have shown that catechol introduces an occupied π state at the lower end of the anatase gap, and the shift in the absorption has been attributed to a direct charge transfer excitation from this level to the Ti levels at the bottom of the CB [106]. In line with this scheme, a time-dependent density functional theory (TDDFT) investigation of catechol bound to a TiO$_2$ nanocluster has revealed that the new excitation is dominated by a direct catechol → TiO$_2$ transition [107].

In this chapter, we characterise the adsorption of catechol on TiO$_2$. We have employed both the (100) face of rutile, much less investigated than the (110), and the (101) face of the anatase polymorph, the most abundant surface in nanopartiles for DSSCs. We start with the study of the lattice parameters of TiO$_2$ rutile and anatase. Then we move to the surfaces, for which we have calculated their optimised geometries and formation energies. Finally, we investigate the geometries, binding energies, and electronic structures of various binding modes on both surfaces.

3.2 Computational details

The calculations in the present chapter have been performed with the VASP 4.6.34 package [97, 98], which solves the KS equations of the system through a self-consistent procedure in a plane waves basis set. We have used the GGA functional in the formalism of Perdew and Wang (PW91) [89] and ultrasoft pseudopotentials [101]. Specifically, the 4s and 3d of Ti, the 2s and 2p of O and C, and the 1s of H were considered as valence electrons. We have found that the inclusion of the 3s and 3p electrons of Ti results in a difference in the anatase bulk parameters of less than 0.01 Å.

We have performed the optimisations with the conjugate gradient method, stopped when the force acting on each ion was less than 0.03 eV/Å. The convergence of the plane wave cutoff and **k**-point grid for bulk anatase and rutile is discussed in the subsection 3.3.1. The surface calculations were performed by rescaling the converged bulk mesh according to the new surface lattice vectors. For DOS calculations we have increased the number of **k**-points, adopting a finer grid of $(1 \times 8 \times 8)$.

In order to adsorb the dye, the rutile and anatase substrate were modeled by respectively (3×3) and (1×2) supercells, with dimensions of $(13.935 \times 8.973$ Å) for rutile, $(10.477 \times 7.620$ Å) for anatase. Since VASP implements a periodic boundary conditions scheme, we have introduced a vacuum of at least 10 Å between adjacent slabs to avoid any interaction between replica atoms. In the surface calculations, the TiO$_2$ units at the bottom (1 for rutile, 2 for anatase) were constrained to their bulk positions.

We have evaluated the unrelaxed surface formation energy of a slab containing n Ti-layers (defined in sections 3.4 and 3.5) according to the formula:

$$E^{\mathrm{surf}}_{\mathrm{unrel}}(n) = \frac{1}{2A}(E_{\mathrm{unrel}}(n) - \bar{n}E_{\mathrm{bulk}}), \tag{3.1}$$

where A is the surface area of the slab, $E_{\mathrm{unrel}}(n)$ the energy of the unrelaxed slab, $\bar{n}$ the number of TiO$_2$ units in the surface unit cell, and E_{bulk} the energy per TiO$_2$ unit in the infinite bulk system. The energetic gain after the optimisation, $E_{\mathrm{gain}}(n)$, was added to the unrelaxed surface energy to obtain the relaxed surface formation energy $E^{\mathrm{surf}}_{\mathrm{rel}}(n)$:

$$E^{\mathrm{surf}}_{\mathrm{rel}}(n) = E^{\mathrm{surf}}_{\mathrm{unrel}}(n) + E_{\mathrm{gain}}(n) \tag{3.2}$$

The adsorption energies of catechol were evaluated according to the formula:

$$\Delta E = E_{\mathrm{surf+cat}} - E_{\mathrm{surf}} - E_{\mathrm{cat}}. \tag{3.3}$$

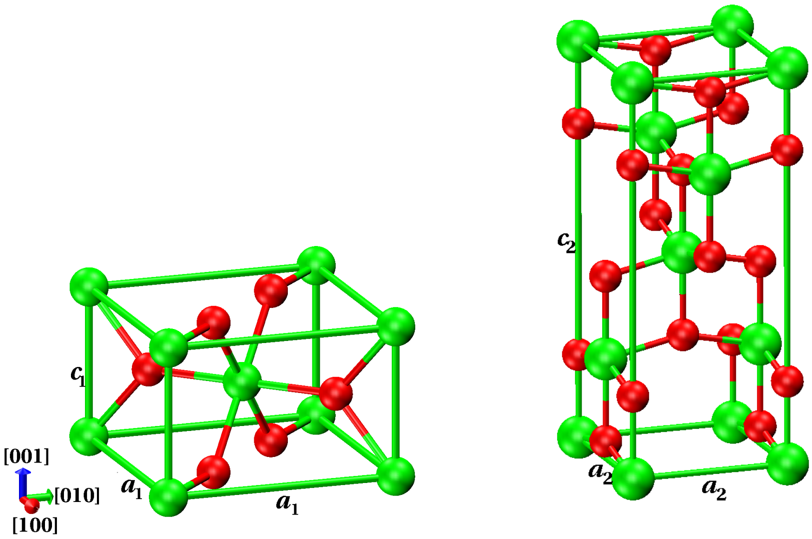

Figure 3.1: Primitive cells of TiO_2 rutile (left, adapted with permission from Ref. [110]. Copyright 2010 American Chemical Society), and anatase (right). Ti are green, O red. The lattice vectors of the two phases are indicated.

Here, $E_{\text{surf+cat}}$ is the energy of the supercell containing the adsorbed catechol, while E_{surf} and E_{cat} are the energy of the same supercell with respectively only the dye or the surface.

All of the figures were made with VMD [108].

3.3 Bulk TiO_2 rutile and anatase

Rutile and anatase have both a tetragonal primitive cell, defined by the vectors a_1 and c_1 for rutile, a_2 and c_2 for anatase (Figure 3.1). In both polymorphs, each Ti is coordinated to six neighbouring O via two long and four short Ti–O bonds (1.976 vs 1.946 Å in rutile, 1.979 vs 1.932 Å in anatase [109]), while each O is coordinated to three Ti via one long and two short bonds lying in the same plane.

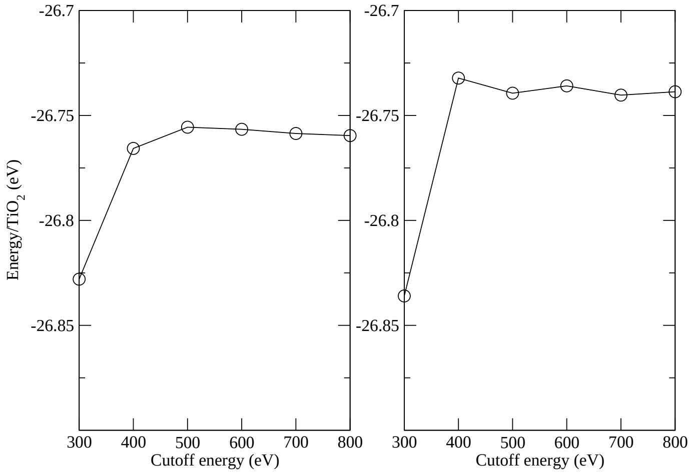

Figure 3.2: Energy/TiO_2 unit of bulk rutile (left) and anatase (right) with respect to the cutoff energy of the plane waves.

3.3.1 Lattice parameters

Figure 3.2 shows the convergencies of the energy/TiO_2 unit of bulk TiO_2 rutile and anatase with respect to the cutoff energy of the plane waves. The default cutoffs in VASP for Ti and O pseudopotentials are 181 and 396 eV respectively. When the value of 400 eV is employed, convergencies to within 10 meV/TiO_2 unit for rutile and anatase are reached with Monkhorst-Pack grids of $(5 \times 5 \times 5)$ and $(4 \times 4 \times 1)$ respectively (Figure 3.3).

To calculate the lattice vectors of the two polymorphs, we have relaxed the cell shape and the atoms for a set of runs at fixed volumes, using the previously converged values of cutoff energies and **k**-point grids (Figure 3.4). The lattice vectors corresponding to the lowest energy configuration are reported in Table 3.1, together with other results from the literature [111, 112]. The calculated lattice parameters differ by around 1-2% from the measured ones, as typical of GGA. The agreement with a previous DFT work employing PBE is good, which gives us confidence in the use of VASP pseudopotentials for TiO_2 throughout this thesis.

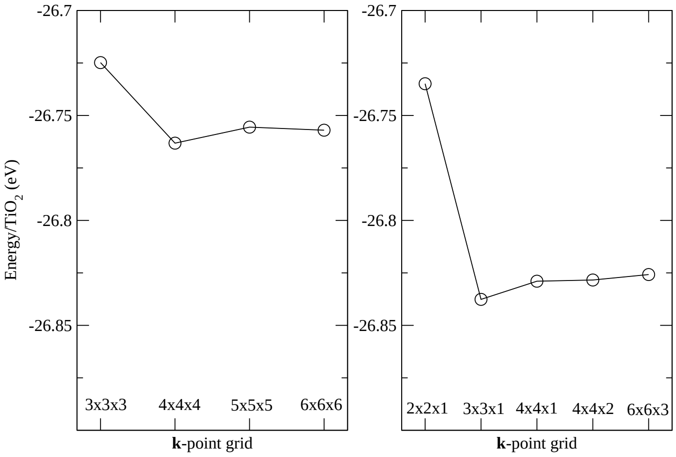

Figure 3.3: Energy/TiO$_2$ unit of bulk rutile (left) and anatase (right) with respect to the **k**-point grid.

	Rutile		Anatase	
	a_1	c_1	a_2	c_2
This work	4.656	2.975	3.811	9.759
PBE [12]	4.634	2.963	3.786	9.737
LDA [12]	4.546	2.925	3.735	9.534
Exp [111, 112]	4.594	2.959	3.784	9.514

Table 3.1: Calculated lattice parameters of TiO$_2$ rutile and anatase compared with other theoretical and experimental results.

From Figure 3.4, it appears that GGA predicts the anatase phase to be more stable than rutile, whereas experimentally rutile is more stable. A similar discrepancy has already been found in a previous DFT study [12], where it has been shown that it does not originate from the choice of pseudopotentials or computational inaccuracies.

3.4 The (100) face of rutile

The rutile (100) surface is formed by alternating Ti-layers, i.e. stoichiometric units similar to O1–Ti2–O3 and O4–Ti5–O6 in Figure 3.5. The topmost Ti-

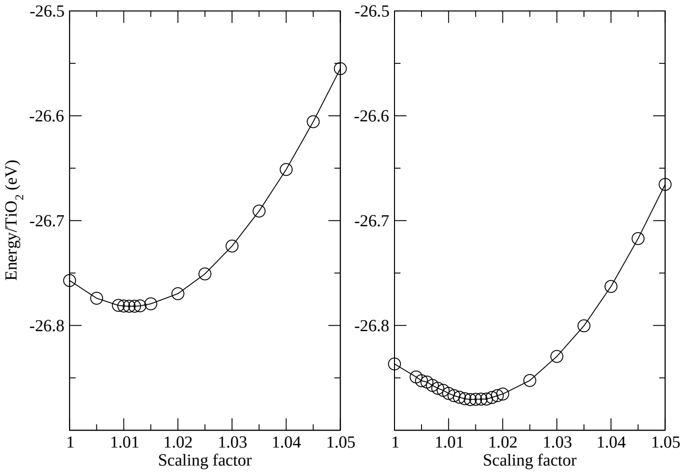

Figure 3.4: Energy/TiO$_2$ unit of bulk rutile (left) and anatase (right) as a function of the volume of the unit cell. The x-axis is the scaling factor with respect to the experimental volumes of Ref. [111, 112].

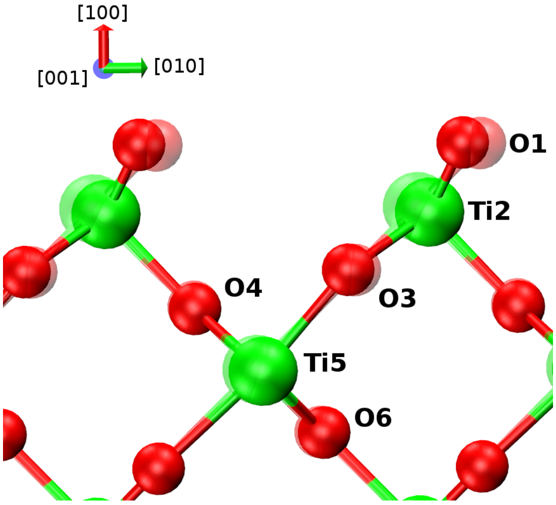

Figure 3.5: Geometry of the rutile (100) surface before (transparent) and after (opaque) the structural relaxation. Ti are green, O red.

	Number of Ti-layers							
	3		4		5		6	
Label	[010]	[100]	[010]	[100]	[010]	[100]	[010]	[100]
O1	−0.25	+0.01	−0.31	+0.07	−0.27	+0.06	−0.26	+0.04
Ti2	+0.17	−0.08	+0.14	−0.03	+0.16	−0.04	+0.18	−0.06
O3	−0.10	+0.00	−0.12	+0.05	−0.13	+0.06	−0.10	+0.03
O4	+0.02	−0.03	−0.02	+0.02	−0.02	−0.02	+0.00	−0.02
Ti5	+0.09	−0.03	+0.08	+0.02	+0.10	+0.01	+0.11	+0.00
O6	+0.05	−0.01	−0.02	+0.01	+0.03	+0.01	−0.01	−0.02

Table 3.2: Calculated displacements (Å) of the rutile (100) surface relative to the optimised bulk terminated structure along [010] and [100] for different numbers of Ti-layers. Labels refer to Figure 3.5. Adapted with permission from Ref. [110]. Copyright 2010 American Chemical Society.

	Unrelaxed	Relaxed
This work	0.096	0.045
PBE [113]	0.098	0.052
PBE [114]	-	0.043
LDA [117]	-	0.074
B3LYP [114]	-	0.044

Table 3.3: Surface formation energies (eV/Å^2) of rutile (100) compared with other results in the literature.

layers expose twofold coordinated bridging O1 bonded to fivefold coordinated Ti2. These are bonded to threefold coordinated O3.

To find a converged thickness, we have studied the geometry and the formation energy of the (1×1) surface for slabs ranging from 3 to 6 Ti-layers. Displacements from the bulk truncated structure along [010] and [100] are reported in Table 3.2. For reasons of symmetry, no displacements could be observed along [001]. The most important changes occur in the topmost Ti-layer. Here, in the thickest slab, O1 and O3 move respectively by −0.26 and −0.10 Å along [010], as Ti2 moves by 0.18 Å. Opposite displacements between T2 (upwards), and O1 and O3 (downwards), occur also along [100]. Though with some minor differences, this pattern has been previously reported [113–116], and is reproduced at a good level also with a slab containing only 3 Ti-layers.

Table 3.3 compares the calculated surface energies with results from the literature. The agreement with previous GGA studies and B3LYP is very good. The unrelaxed and relaxed surface energies as a function of the slab thickness are

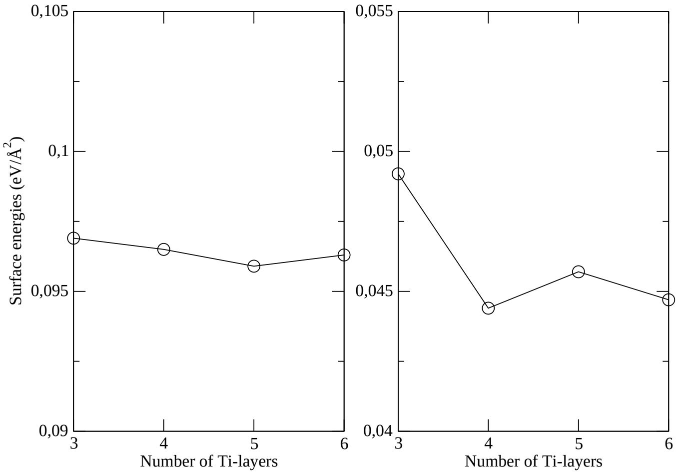

Figure 3.6: Unrelaxed (left) and relaxed (right) surface formation energies of TiO_2 rutile (100) with respect to the number of Ti-layers.

shown in Figure 3.6. Results from a slab with 3 Ti-layers are already converged to better than 0.005 eV/Å^2 with respect to the values of the thickest 6-layer slab.

3.5 The (101) face of anatase

The (101) surface is the one mainly exposed in anatase nanoparticles (Figure 3.7). It has a characteristic sawtooth profile along [$10\bar{1}$]. Analogously to rutile (100), we define a Ti-layer to be made by O–Ti–O stoichiometric units, like O1–Ti2–O3 or O4–Ti5–O6. The topmost Ti-layers expose twofold coordinated bridging O1 bonded to fivefold coordinated Ti2. These are bonded to threefold coordinated O3 along [010]. O4–Ti5–O6 units are instead fully coordinated.

Table 3.4 reports the displacements from the bulk truncated structure along [$10\bar{1}$] and (101) for different numbers of Ti-layers. Due to symmetry, there are no relaxations along [010]. As for rutile (100), the most important changes occur in the topmost Ti-layer. Here, in the 10-layer slab, O1 moves along [$10\bar{1}$] by

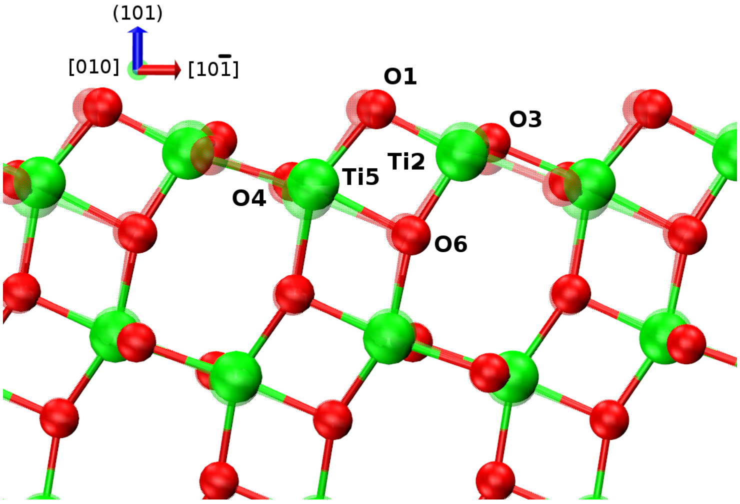

Figure 3.7: Geometry of the anatase (101) surface before (transparent) and after (opaque) the structural relaxation. Ti are green, O red.

	Number of Ti-layers							
	4		6		8		10	
Label	$[10\bar{1}]$	(101)	$[10\bar{1}]$	(101)	$[10\bar{1}]$	(101)	$[10\bar{1}]$	(101)
O1	+0.26	−0.02	+0.20	+0.00	+0.20	+0.00	+0.20	+0.00
Ti2	−0.02	−0.24	−0.04	−0.16	−0.04	−0.15	−0.04	−0.14
O3	+0.10	+0.17	+0.08	+0.21	+0.09	+0.23	+0.09	+0.24
O4	+0.10	+0.09	+0.07	+0.04	+0.07	+0.05	+0.08	+0.06
Ti5	+0.12	+0.22	+0.10	+0.20	+0.10	+0.18	+0.10	+0.19
O6	+0.06	−0.12	+0.08	−0.06	+0.10	−0.05	+0.10	−0.05

Table 3.4: Calculated displacements (Å) of the anatase (101) surface relative to the optimised bulk terminated structure along $[10\bar{1}]$ and (101) for different numbers of Ti-layers. Labels refer to Figure 3.7.

0.20 Å, while Ti2 and O3 move towards (101) by respectively −0.14 and 0.24 Å, bringing O3 to be located above Ti2. A significant relaxation upwards by 0.19 Å occurs also for Ti5. We note that a good description of the changes is given with a slab of at least 6 Ti-layers. The relaxations reported are in line with the calculations in the literature employing GGA [12].

Surface formation energies are presented in Table 3.5. There is a good agreement between ours and previously reported GGA and B3LYP results. As for rutile (100) the surface energies converge very fast with the thickness of the slab (Figure 3.8). Both the unrelaxed and relaxed values of a 6 Ti-layer slab

	Unrelaxed	Relaxed
This work	0.078	0.034
PBE [12]	0.080	0.031
PBE [114]	-	0.031
B3LYP [114]	-	0.035
LDA [12]	0.097	0.052

Table 3.5: Surface formation energies (eV/Å^2) of anatase (101) compared with other results in the literature.

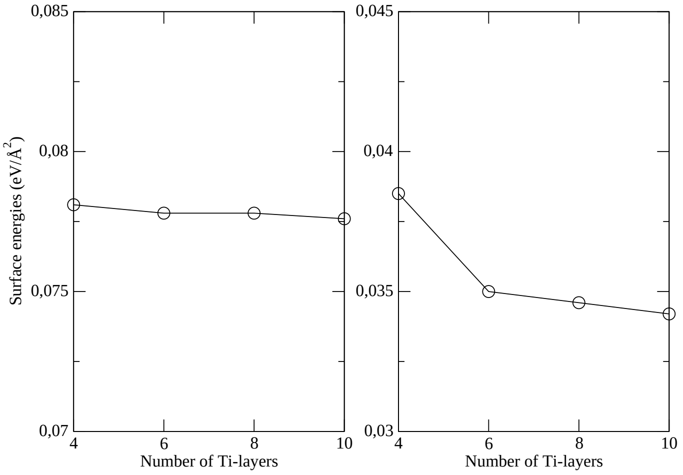

Figure 3.8: Unrelaxed (left) and relaxed (right) surface formation energies of TiO$_2$ anatase (101) with respect to the number of Ti-layers.

are already converged to better than 0.005 eV/Å^2 with respect to the values of 0.078 and 0.034 eV/Å^2 of a 10 Ti-layer slab.

3.6 Adsorption of catechol

Before adsorbing catechol on TiO$_2$ we have tested the pseudopotentials supplied with VASP on the structure of catechol (Figure 3.9). The main geometrical parameters are displayed in Table 3.6, together with others from a published GGA-DFT work [118]. At the cutoff energy of 400 eV, previously employed for TiO$_2$, the agreement between the two is found to be good. Thus, throughout this thesis, when using VASP, the adsorption of organic molecules on TiO$_2$ will

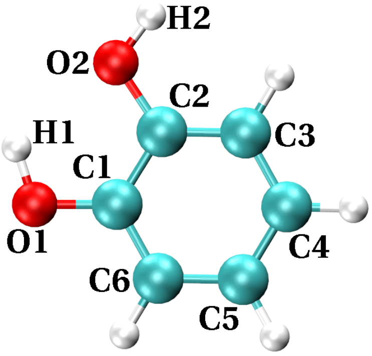

Figure 3.9: Catechol molecule with the atomic labels used in the text. O are red, C cyan, H white.

be performed with that cutoff.

3.6.1 Adsorption structures

Catechol can be present in solution as a neutral, partially dissociated, or fully dissociated species. For each of the species, we have investigated a possible type of adsorption on both the TiO_2 substrates. In particular, we have studied a molecular (rMOL, aMOL), a partially dissociative monodentate (rMON, aMON), and a fully dissociative bridging adsorption (rBRI, aBRI), where the prefixes r and a indicate respectively an adsorption on rutile or anatase. To preserve the neutrality of the cell, when removed from catechol, we have bonded H ions to the nearest bridging O at the surface.

The six optimised structures are shown in Figure 3.10. In every mode, the Ti bonded to catechol are displaced outwards, so as to favour the interaction. In rMOL and aMOL, both the OH groups of neutral catechol form hydrogen bonds with two twofold coordinated O of the substrate. In rMON and aMON, one O of catechol bonds to a fivefold coordinated Ti, while the OH group interacts by a hydrogen bond with a twofold coordinated O. Both the O of the dye bond to two adjacent fivefold coordinated Ti in the relaxed rBRI and aBRI structures.

Bonds	Ref. [118]	This work
C1C2	1.42	1.40
C2C3	1.40	1.39
C3C4	1.41	1.40
C4C5	1.40	1.39
C5C6	1.40	1.39
C6C1	1.40	1.39
C1O1	1.37	1.37
C2O2	1.37	1.38
Angles		
C1C2C3	120.0	120.6
C2C3C4	120.1	120.0
C3C4C5	119.9	120.0
C4C5C6	120.0	120.4
C5C6C1	120.3	120.1
C6C1C2	119.6	119.3
O1C1C2	121.6	120.7
O2C2C3	124.3	124.1
Dihedrals		
H1O1C1C2	0.1	0.0
H2O2C2C3	0.0	0.0

Table 3.6: Main geometrical parameters of catechol compared to the results in the literature. Labels refer to Figure 3.9.

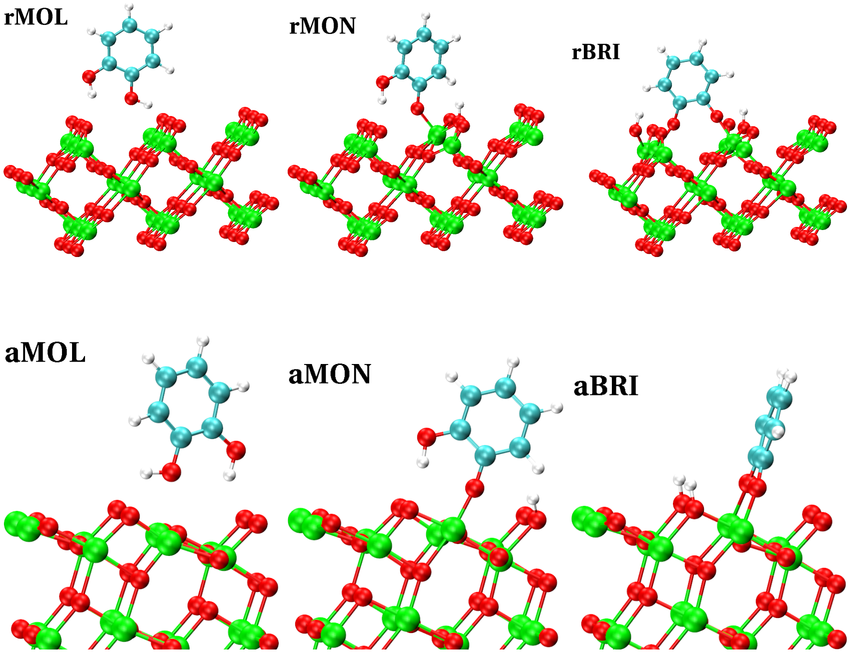

Figure 3.10: Geometries of the optimised adsorptions of catechol on rutile (100) (top, adapted with permission from Ref. [110]. Copyright 2010 American Chemical Society), and anatase (101) (bottom). Ti are green, O red, C cyan, H white.

3.6.2 Adsorption energies

Table 3.7 reports the adsorption energies relative to the different modes. On rutile (100), rMON is the most favoured, similarly to what has been found for the (110) face [119].

We have repeated the calculations for rMON on a thicker slab with 5 Ti-layers. However, the adsorption energy we have found in this case (−0.83 eV) was close to that of the 3 Ti-layer slab (−0.88 eV), suggesting that increasing

Mode	E_{ads} (eV)
rMOL	−0.33
rMON	−0.88
rBRI	+0.11
aMOL	−0.31
aMON	−0.81
aBRI	−1.00

Table 3.7: Adsorption energies of the investigated modes of catechol on rutile (100) and anatase (101). See text for the abbreviations of modes.

the slab thickness has little effect.

We have found rBRI to have a positive adsorption energy, regardless of the starting configurations and positions of hydrogens on the surface, and have not investigated it further. This result seems to be a peculiarity of the rutile (100) surface, since a similar adsorption is energetically favoured on the fivefold coordinated Ti of rutile (110) [119], and the corresponding aBRI is the most stable mode on anatase (101). Here, the adsorption energies of aMOL and aMON are very close to those of rMOL and rMON on rutile (100).

3.6.3 Electronic structures

Figure 3.11 shows the electronic structures for the different modes of adsorption of catechol on rutile (100) and anatase (101). In both substrates, catechol introduces occupied molecular states into the band gap, while it does not contribute to the lowest unoccupied levels in any of the binding modes, as confirmed by the HOMO and LUMO charge-density isosurfaces (Figure 3.12). This picture fits in the type II mechanism of the catechol/TiO$_2$ system, in which the experimental new low-energy band is thought to be given by a catechol → TiO$_2$ transition [36, 107].

Due to the well known band gap problem of DFT [120], we are not able to determine the position of the gap states (HOMO and HOMOs-1) with respect to the bottom of the CB of TiO$_2$. We note that the position of HOMO and HOMOs-1 inside the gap seems to be related to the strength of the adsorption: they are at the edge of the CB in rMOL and aMOL, ($E_{\text{ads}} =\sim -0.3$ eV), pushed towards the gap in rMON and aMOL, ($E_{\text{ads}} =\sim -0.9$ eV), and located inside the gap in aBRI ($E_{\text{ads}} = -1.00$ eV).

A recent combined theoretical and experimental study of catechol on rutile (110) has revealed that both bridging and monodentate adsorptions coexist, but the latter is more stable [119]. However, only the bridging binding was found to be able to introduce states in the gap of rutile. This is not a desirable situtation, as these states have been shown to be involved in the type II mechanism [107].

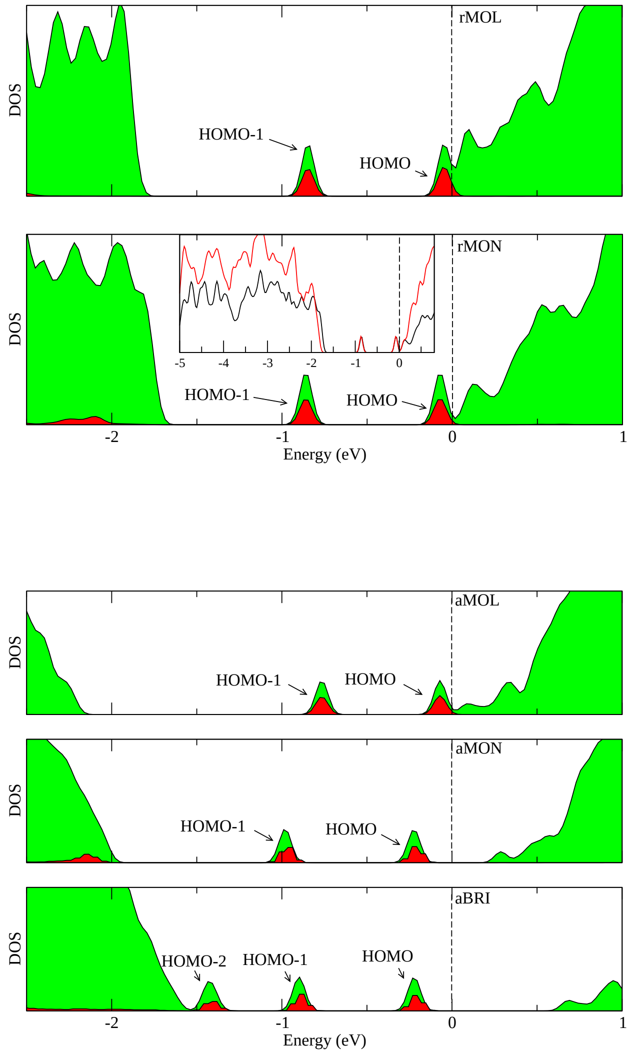

Figure 3.11: Electronic structures of the three modes of adsorption of catechol on rutile (100) (top, adapted with permission from Ref. [110]. Copyright 2010 American Chemical Society), and anatase (101) (bottom). In green are plotted the total DOS (arbitrary units), in red their projections on catechol. The Fermi energies are marked by dashed lines. Inset: total DOS of rMON on a 3-layer (black) compared with a 5-layer (red) slab.

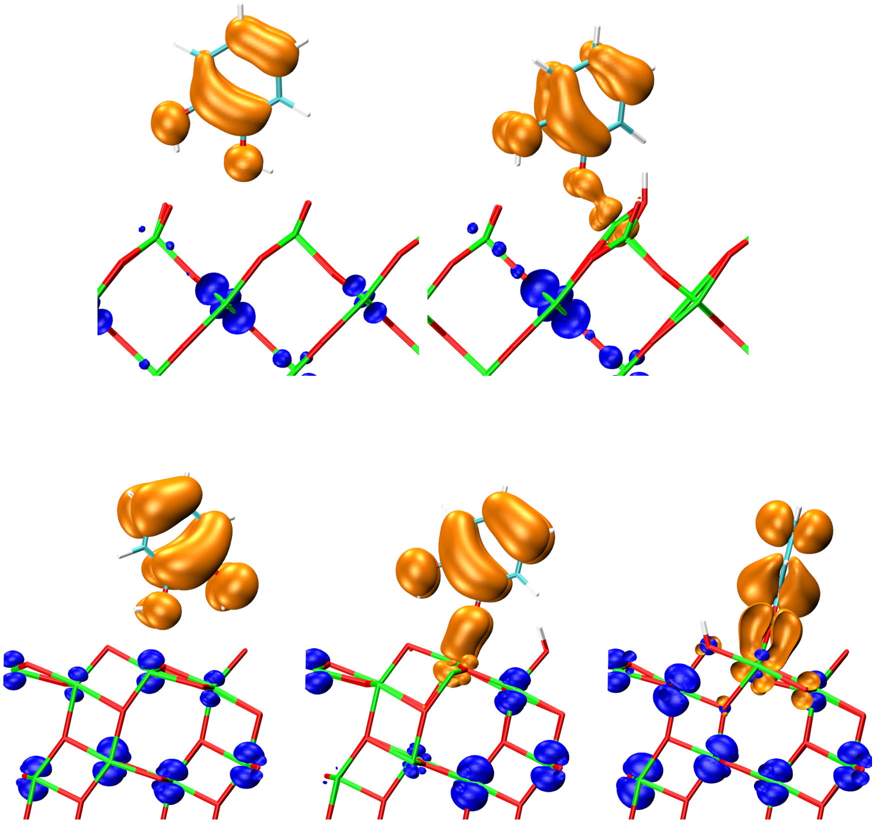

Figure 3.12: Charge-density isosurfaces of 0.03 e/Å^3 of HOMO (orange) and LUMO (blue) for the adsorption modes investigated on rutile (100) (top) and anatase (101) (bottom). Both views are from [010].

On rutile (100), we find instead gap states to appear for the most stable monodentate binding. This is a favourable characteristic for the electron injection, which suggests that the photocurrent in rutile DSSCs may increase with the (100) orientation of the nanoparticles.

Finally, in order to prove that our results do not depend on the finite slab thickness, we have calculated the DOS of rMON using a thicker 5-layer slab (Figure 3.11, inset). This causes an increase of the band gap of the oxide by about 0.1 eV, but the qualitative shape of the DOS, and the relative position of HOMO, HOMO−1, and CB remains unaltered.

3.7 Summary of the chapter

In this chapter, we have introduced rutile and anatase, the two polymorphs of TiO_2 commonly present in nanoparticles for DSSCs. For both, we have determined converged cutoff energies and **k**-point grids, together with lattice parameters, which we will use throughout the thesis. We have characterised the (100) face of rutile and the (101) face of anatase, describing their geometries and surface energies.

On both substrates, we have investigated the adsorption of catechol. Monodentate and bridging are the most stable bindings on rutile (100) and anatase (101) respectively. Regardless of the type of substrate and interaction, the LUMOs are localised only on the surface, while at least two states localised on catechol, HOMO and HOMO–1, are introduced into the band gap after the adsorption. The electronic structure for the binding modes of catechol on TiO_2 fit into the general understanding of the type II mechanism, which is thought to be direct from catechol to the semiconductor, and not to involve any excited states of the dye.

Chapter 4

Coating the TiO_2 electrode with Al_2O_3

4.1 Introduction

A route to the increase of efficiency of DSSCs is the coating of the TiO_2 film with an overlayer of a second oxide [5]. The mechanism through which the overlayer increases the efficiency is still under debate, and at least four possible explanations have been proposed [121].

In the first mechanism, the insulating layer works as a physical barrier which retards all of the electron transfers at the interface [55]. However, while the injection into the semiconductor is insensitive to the small lengthening of the injection time caused by the coating, a retardation of the recombinations at the TiO_2/dye and TiO_2/electrolyte interfaces reduces the losses. This results into a larger electron concentration in the TiO_2 film, and consequently into a higher quasi-Fermi level and open-circuit photovoltage V_{oc}. A retardation of interfacial charge recombinations has been reported for various oxides, such as Al_2O_3 [54, 56], Nb_2O_5 [58, 59], MgO [60], $CaCO_3$ [61], and ZrO_2 [62].

In the second mechanism, the overlayer creates a dipole moment at the oxide/oxide interface, which could be due to its higher isoelectric point (the pH value for zero surface charge), or its electron affinity lower than TiO_2. It is the so-called surface dipole effect, which induces a positive shift of the TiO_2 CB, and results into a higher V_{oc}. A good correlation has been found between the isoelectric points of Al_2O_3, ZrO_2, ZnO and the induced change in V_{oc}, suggesting that the acidity of the material is a key factor [63].

In the third mechanism, the second oxide is thought to passivate the surface states of TiO_2, which are responsible for the recombination of the injected electron with the dye or the redox couple. Charge transfer from surface states has been shown to be strongly suppressed by the Al_2O_3 coating [64].

In the fourth mechanism, the improved performance of DSSCs arises from an enhanced adsorption of the dye on the overlayer, which, if with a high isoelectric point (more basic) than TiO_2, favours the attachment of carboxyl dyes. For instance, surface modification of nanocrystalline SnO_2 electrodes with a thin layer of MgO, Al_2O_3, and ZrO_2 was found to improve the adsorption of a Ru complex, and thus the photocurrent in the cell [65].

Since its isoelectric point is much higher than that of TiO_2 (9.2 vs 5.5), Al_2O_3 is one of the most popular oxides to be used to coat TiO_2 nanoparticles. On Al_2O_3, the amount of dye adsorption increases with the thickness of the overlayer [66]. However, a coating which is too thick blocks the photocurrent, with a corresponding loss of efficiency. In order to optimise the efficiency then, it is necessary to employ an overlayer with an optimum thickness, and values ranging from 1 to 120 Å have been reported in the literature [66].

The carboxyl group –COOH constitutes the binding anchor of the most widely used Ru-based dyes. In the attempt to shed light on their adsorption, the interaction of formic acid (HCOOH) with anatase has been the subject of many works in the last years [22–27]. However, the results in the literature are not always in agreement with each other, indicating that further investigations are necessary on this system. For example, some DFT studies have suggested that the most stable structure is a molecular monodentate [22, 25]. Others have predicted that the latter is in equilibrium with a dissociative bridging [23], whereas an experimental work has shown that, in addition to hydrogen bonded HCOOH, chelating and monodentate formate ($HCOO^-$) are also present [26].

Contrary to the information on the adsorption of HCOOH on TiO_2 anatase, the information regarding the adsorption on Al_2O_3 is scarce. There is experimental evidence that formic acid bonds to the surface by the two oxygens [122], supported by the finding that the spectrum of the bridging adsorption given by DFT best matches the experimental counterpart [123]. It is of vital importance, in order to understand the effect of the Al_2O_3 coating, to gain more insights into this system.

In this chapter, we address the effect of the Al_2O_3 overlayer on the binding of formic acid and catechol on TiO_2 anatase (101). First, we describe the generation of the amorphous Al_2O_3 (a-Al_2O_3) through the "melt and quench" technique [124], and test our sample against others in the literature. Then, we proceed to the adsorption of the two binding groups. Finally, by adsorbing the benchmark N3 dye [40], anchoring through –COOH groups, we show that the results obtained for formic acid can be generalised and extended to larger dyes commonly employed in DSSCs.

4.2 Computational details

The calculations in the present chapter have been performed with the VASP 4.6.34 package [97, 98]. We have used the GGA functional in the formalism of Perdew and Wang (PW91) [89] and ultrasoft pseudopotentials [101]. Specifically, the 4s and 3d of Ti, the 5s and 4d of Ru, the 3s and 3p of Al, the 2s and 2p of O and C, and the 1s of H were considered as valence electrons.

Since VASP implements a periodic boundary conditions scheme, we have introduced a vacuum of at least 10 Å between adjacent slabs to avoid any interaction between replica atoms. Optimisations were performed with the conjugate gradient method, and stopped when the force acting on each nucleus was less than 0.03 eV/Å. The convergence of the plane wave cutoff and **k**-point grid for bulk Al_2O_3 corundum is discussed in Section 4.3. We have performed the calculations on the Al_2O_3/TiO_2 interface with a grid of $(1 \times 2 \times 1)$, obtained by rescaling to the surface unit cell described in section 4.4 the converged grid of bulk anatase (subsection 3.3.1). For DOS calculations we have increased the number of **k**-points, adopting a finer grid of $(8 \times 8 \times 1)$.

The adsorption energies were evaluated according to the formula:

$$\Delta E = E_{\mathrm{surf+mol}} - E_{\mathrm{surf}} - E_{\mathrm{mol}}, \tag{4.1}$$

where $E_{\mathrm{surf+mol}}$ is the energy of the supercell with adsorbed a molecule (HCOOH, catechol, or N3), while E_{surf} and E_{mol} are the energy of the same supercell with respectively only the substrate or a single isolated molecule.

All of the figures were made with VMD [108].

4.3 Bulk Al_2O_3 corundum

The corundum phase of Al_2O_3 (α-Al_2O_3) crystallises into a simple hexagonal Bravais lattice (Figure 4.1), defined by the lattice constants a_3 and c_3. The O form a hexagonal close-packed (hcp) structure, where the Al occupy two thirds of the octahedrally coordinated interstices.

4.3.1 Lattice parameters

The convergence of the energy/Al_2O_3 unit of bulk α-Al_2O_3 with respect to the cutoff energy of the plane waves is shown in Figure 4.2. With a cutoff of 400 eV (employed in chapter 3 for the adsorption of catechol on TiO_2), a convergence to within 10 meV/Al_2O_3 unit is reached with a Monkhorst-Pack grid of $(2 \times 2 \times 1)$ (Figure 4.3).

To calculate the lattice parameters of the crystal, we have relaxed the cell shape and the atoms for a set of runs at fixed volumes (Figure 4.4). The

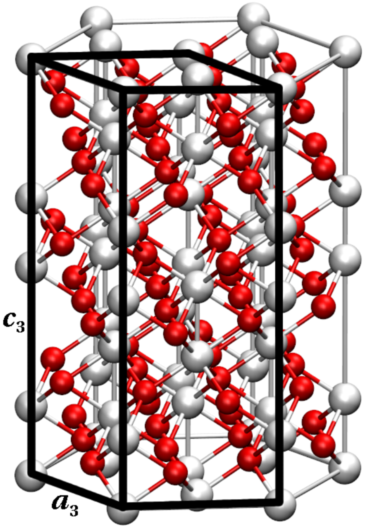

Figure 4.1: Hexagonal Bravais lattice of α-Al_2O_3. Al are white, O red. The unit cell and the lattice vectors a_3 and c_3 are indicated.

	a_3	c_3
This work	4.827	13.172
GGA [125]	4.82	13.16
LDA [127]	4.590	12.560
Exp [126]	4.756	12.982

Table 4.1: Calculated lattice parameters of α-Al_2O_3 compared with other theoretical and experimental results.

lattice vectors corresponding to the lowest energy configuration of α-Al_2O_3 are reported in Table 4.1, where they are compared with other results from the literature. Our lattice parameters match those of a previous GGA work [125]. The overestimation of the experimental values is around 1.5%, which validates the use of VASP pseudopotentials for Al and O at the cutoff of 400 eV.

4.4 The a-Al_2O_3/TiO_2 anatase (101) interface

We have generated the a-Al_2O_3 sample by the melt and quench technique on α-Al_2O_3 [124]. Our final goal was the reproduction of the a-Al_2O_3/TiO_2 anatase (101) interface. Therefore, we have chosen the size of the bulk α-Al_2O_3 unit cell to be melted in a way to minimise the lattice strain once placed on a surface

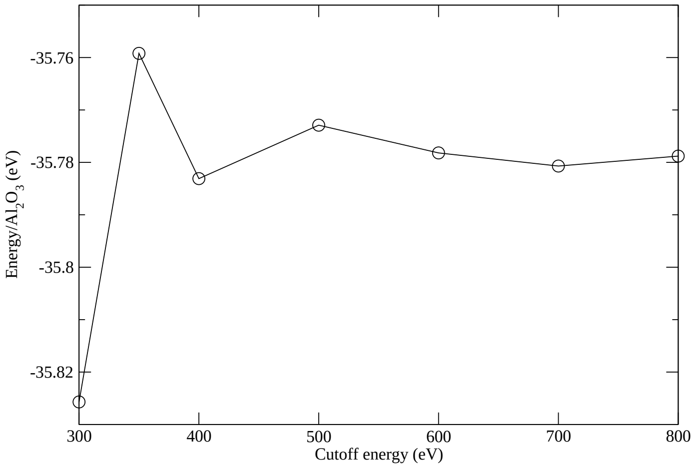

Figure 4.2: Energy/Al_2O_3 unit of bulk α-Al_2O_3 with respect to the cutoff energy of the plane waves.

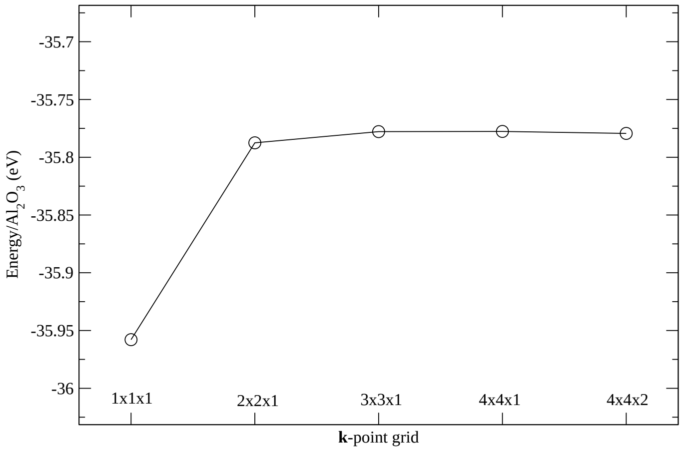

Figure 4.3: Energy/Al_2O_3 unit of bulk α-Al_2O_3 with respect to the **k**-point grid.

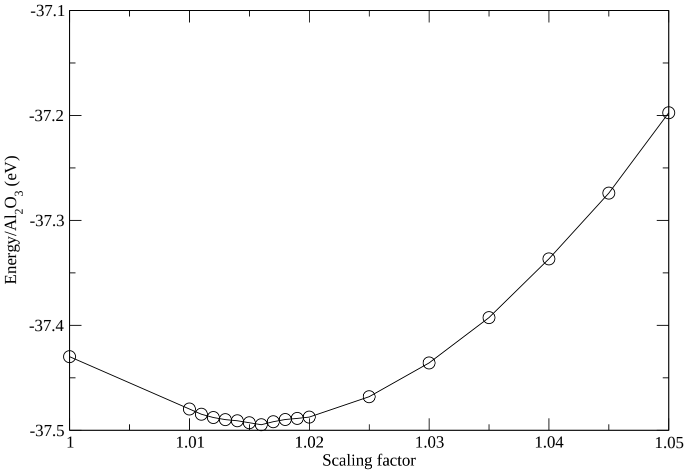

Figure 4.4: Energy/Al_2O_3 unit of bulk α-Al_2O_3 as a function of the volume of the unit cell. The x-axis is the scaling factor with respect to the experimental volume of Ref. [126].

unit cell of anatase (101), in the limit of our computational capabilites.

Using the calculated lattice parameters, we have constructed a 8 Ti-layer (1×2) anatase (101) unit cell with dimensions of $A_1 = 7.622$ and $B_1 = 10.477$ Å, and an orthorhombic bulk α-Al_2O_3 unit cell. The density of a-Al_2O_3 ranges from 2.95 g/cm^3 to 3.3 g/cm^3. Thus, we have multiplied the lattice vectors of α-Al_2O_3 by a factor of 1.06, bringing them to $A_2 = 8.864$, $B_2 = 10.233$, and $C_2 = 13.962$ Å. The corresponding density of 3.2 g/cm^3 coincides with that of previous theoretical study [128]. With this choice of the unit cells, the alignment A_1/A_2, B_1/B_2 gives lattice mismatches of respectively 14 and 2%, which will be compensated as reported below.

The melt and quench procedure of the α-Al_2O_3 has started with 2 ps of *ab initio* molecular dynamics (MD) at $T = 5000$ K (Figure 4.5, a), well above the experimental melting point of 2327 K, during which the bulk oxide was brought to a completely disordered liquid phase. Then, the system was rapidly quenched at a rate of 500 K/ps to the final temperature of 500 K (Figure 4.5, b). At this point, the lattice vectors A_2 and B_2 were adjusted to match respectively

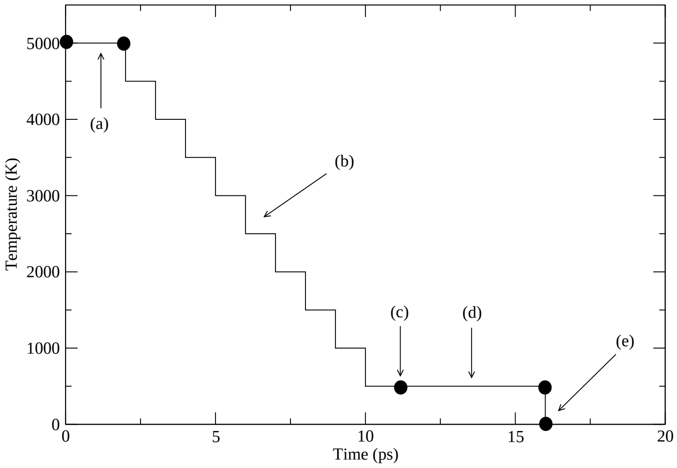

Figure 4.5: Scheme for the generation of the amorphous phase of Al_2O_3. (a) high temperature melting; (b) linear quenching; (c) rescaling of the lattice vectors; (d) equilibration; (e) relaxation at 0 K. Adapted with permission from Ref. [129]. Copyright 2012 American Chemical Society.

A_1 and B_1 of anatase, while preserving the density by varying C_2 (Figure 4.5, c). The system was then equilibrated for 5 ps (Figure 4.5, d), and data were extracted during the last 3 ps of this run. Finally, the sample was relaxed at the temperature of 0 K (Figure 4.5, e).

Figure 4.6 displays the radial distribution functions (RDFs) $g_{12}(r)$ of the binary system, defined as the probability of finding one atom of type 2 in a spherical shell between r and $r + \Delta r$ from one atom of type 1:

$$\big\langle n_{12}(r, r + \Delta r)\big\rangle = 4\pi r^2 \rho_2 g_{12}(r)\Delta r, \tag{4.2}$$

where ρ_2 is the density of atoms of type 2. From the RDFs of Figure 4.6 we can extract the pair nearest-neighbour distances R_M, corresponding to the maximum positions. They are reported in Table 4.2, where they are compared with previous results obtained with classical MD and experiment.

Compared to classical MD, our *ab initio* MD uses a higher cooling rate (1 or 2

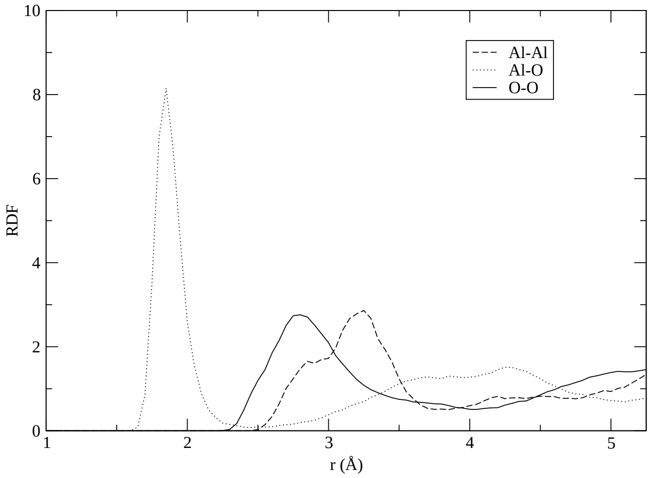

Figure 4.6: RDFs of the a-Al_2O_3 sample generated by the "melt and quench" technique. Adapted with permission from Ref. [129]. Copyright 2012 American Chemical Society.

	Al–O	O–O	Al–Al
This work	1.85	2.80	3.25
Classical MD [130]	1.9	2.8	3.1
Classical MD [131]	1.77	2.82	3.07
Classical MD [128]	1.76	2.75	3.12
Experiment [132]	1.80	2.80	3.12

Table 4.2: Maximum positions R_M of the RDFs compared with other results in the literature.

orders of magnitude) [128,130,131], which deviates more from real experiments. A cooling which is too fast can in theory freeze the liquid state and avoid the system to reach the amorphous phase. Despite this, our DFT maximum positions agree well with theory and experiment.

As a final test, we have calculated the electronic structure of our sample, and compared it to that of the α-Al_2O_3 phase (Figure 4.7). The two are very similar, and differ qualitatively only in the width of the band gap. Its reduction (from 5.7 to 3.1 eV) following the transformation of phase is known in the literature, and is an indicator of the amorphisation process [130, 131].

After being tested, the a-Al_2O_3 sample was placed on the optimised anatase

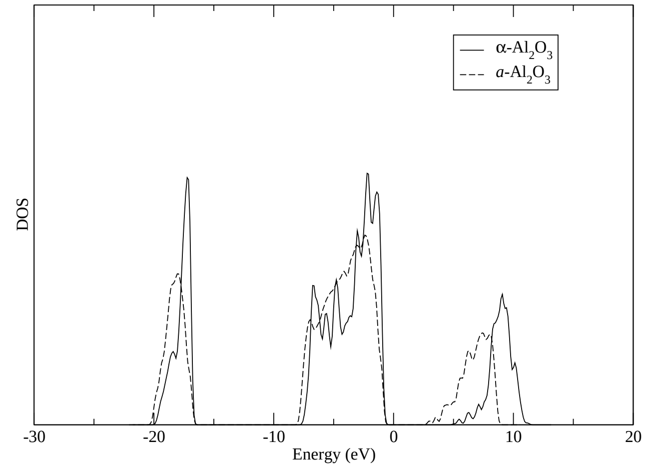

Figure 4.7: Comparison between the electronic structures (arbitrary units) of α-Al_2O_3 and a-Al_2O_3. The first has been multiplied by a factor of 4, to take into account the different number of atoms in the unit cells.

(101) substrate. Then, by two cleavages at distances of 3 and 9 Å from the interface, we have obtained two stoichiometric structures, which we have subsequently relaxed (Figure 4.8).

Our way to generate the interface by stacking a sample prepared with *ab initio* MD does not allow to simulate the atom-by-atom growth, typical of ALD. Kinetic Monte Carlo simulations do not have this disadvantage [133]. However, due to the large number of possible atomic configurations, a statistical kinetics method would have to consider too many elementary events, at the cost of computational time. Our approach constitutes a tradeoff between accuracy and realism, and has been successfully applied to model other interfaces such as a-Al_2O_3/Ge [131], $SrTiO_3$/Si [134], and ZrO_2/Si [135].

The type of bonds across the interface are reported in Table 4.3. While the total number of bonds is equal to 6 in both cases, the coordination pattern is rather different. For example, in the thicker coating, a Ti ion of the top layer is dragged out by about 1 Å, and can thus accommodate three bonds with the O of the coating.

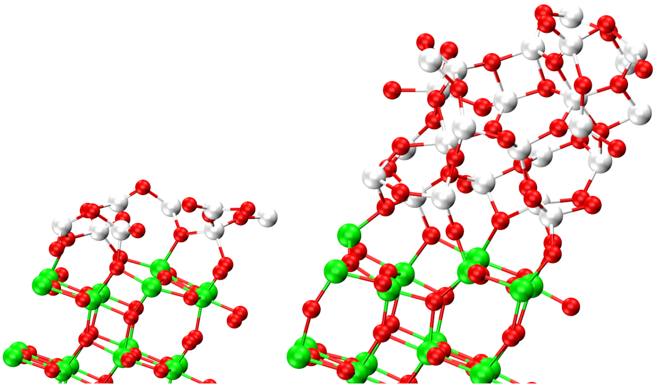

Figure 4.8: Front views of the relaxed 3 (left) and 9 Å (right) coated structures of a-Al_2O_3 on anatase (101). Ti are green, Al white, O red. Reprinted with permission from Ref. [129]. Copyright 2012 American Chemical Society.

	Occurrences		Average lengths	
Bonds	3 Å	9 Å	3 Å	9 Å
$Ti^{\{1\}}$–O	3	1	2.04	1.94
$O^{\{1\}}$–Al	3	3	1.88	1.86
$Ti^{\{3\}}$–O	0	1	-	1.99
$O^{\{2\}}$–Al	0	1	-	2.04

Table 4.3: Pattern of bonds across the interface. The atoms of the substrate are classified according to the numbers of atoms of the overlayer which they bond, as indicated by the superscript. Adapted with permission from Ref. [129]. Copyright 2012 American Chemical Society.

Mode	0 Å	3 Å	9 Å
MON(H)	−0.94	−1.23	unstable
MON	−0.36	−1.37	−1.91
BRI	−0.94	−2.04	−2.78

Table 4.4: Adsorption energies (eV) of HCOOH adsorbed on TiO_2 anatase (101) for different thicknesses of the coating. See Figure 4.9 for the abbreviations. Adapted with permission from Ref. [129]. Copyright 2012 American Chemical Society.

We have estimated the induced corrugation of the TiO_2 substrate by the root mean square deviation (RMSD) of the atoms in its top Ti-layer with respect to the bare surface. The values for the 3 and 9 Å structures are, respectively, 0.18 and 0.35 Å. In the structure with the 9 Å coating, a large contribution to the RMSD is given by the upwards relaxation of the Ti which is dragged out.

4.5 Adsorption of formic acid

In this section, we make use of the two a-Al_2O_3/TiO_2 samples to study the adsorption of formic acid. This small molecule constitutes the binding group of Ru-based dyes, the paradigm of sensitisers for DSSCs, and can thus provide relevant information to understand their adsorption.

4.5.1 Binding energies

On anatase (101), many different bindings are possible [22,23,25,27]. We have exploited the results present in the literature to focus only on the three most stable, i.e. two monodentate (one molecular and one dissociative) and a bridging adsorption. On the amorphous overlayer, the number of different configurations for the same type of adsorption is even larger than on the bare anatase. Our approach was to test the same adsorptions of the bare surface on different binding sites, reporting only the most stable for each.

Figure 4.9 and Table 4.4 present structures and energies of formic acid on anatase (101), with and without the a-Al_2O_3 coating. Without the coating, a molecular monodentate binding (MON(H)-0) is more stable than a dissociative

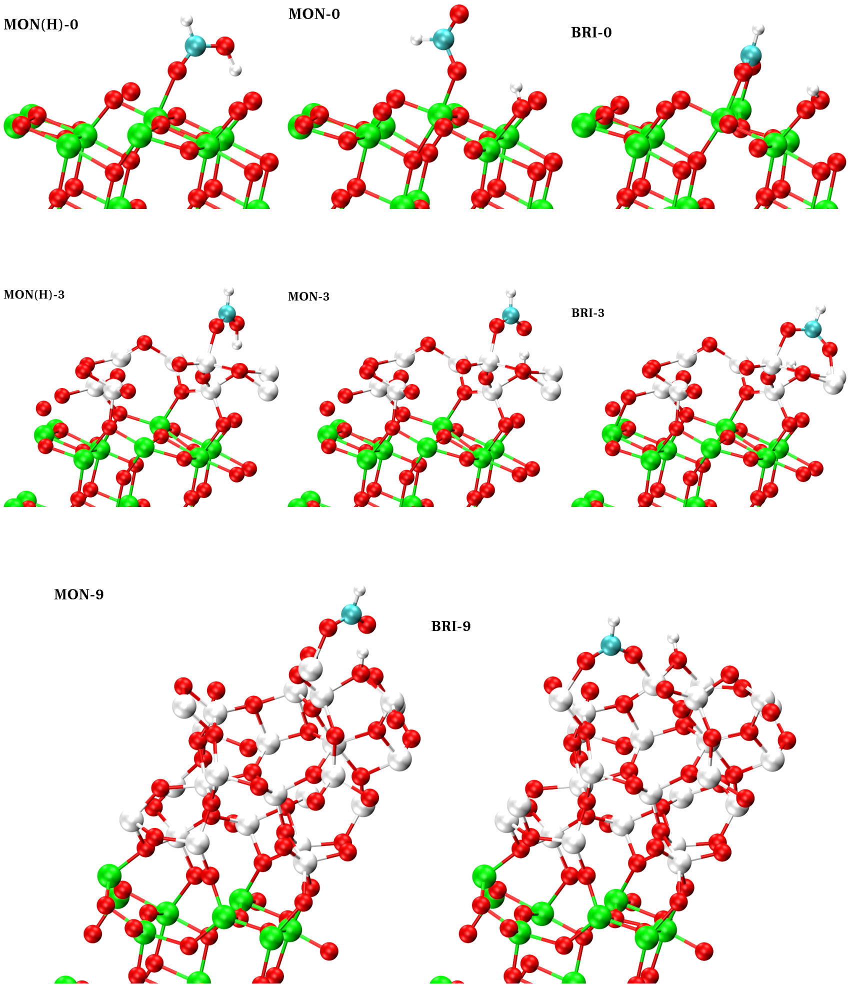

Figure 4.9: Most stable adsorptions of formic acid on TiO_2 anatase (101) for different thicknesses of the a-Al_2O_3 overlayer. MON(H) and MON stand respectively for molecular and dissociative monodentate, BRI for bridging. The number associated with each figure corresponds to the thickness of the overlayer in Å. Ti are green, Al large white, O red, C cyan, H small white. Reprinted with permission from Ref. [129]. Copyright 2012 American Chemical Society.

binding (MON-0), and has adsorption energies close to the bridging (BRI-0), in agreement with a recent work by Nunzi *et al* [23].

The adsorption of HCOOH on the coated system presents a remarkably different scenario. The emerging picture does not seem to depend on the a-Al_2O_3 thickness, with the only exception that all of the molecular adsorptions relax towards dissociative ones (MON-9) on the 9 Å overlayer. A common feature to the two substrates is that the coating reverses the results of bare anatase, where the molecular monodentate binding was favoured over the dissociative.

Despite in some cases we have found adsorption energies for the same type of interaction to spread over a few tenths of eV, bridging adsorptions in the two systems (BRI-3 and BRI-9), are always more stable than corresponding monodentate (MON(H)-3, MON-3, MON-9), consistently with experiments predicting that the molecule is bonded to the surface by the two O [122].

Interestingly, when the coating is present, every adsorption becomes more stable, a fundamental characteristic for the stability of DSSCs based on carboxylate dyes. This finding agrees with a recent work employing the N3 dye on Al_2O_3 overcoated TiO_2, in which the improved adsorption of the dyes was identified as one reason for the increase of the photocurrent [66]. The resulting enhanced adsorption is in line also with another study on a carboxylate-containing dye (Rhodamine B) on the same substrate, where the interaction between –COO and Al was found to be stronger than that between –COO and Ti [136]. In the same work, the authors have proved that the binding mode of Rhodamine B is dominantly the monodentate linkage. We find instead that bridging configurations, with energies larger than 2 eV, stabilise most the interaction of HCOOH.

4.5.2 Vibrational frequencies

The difference Δ between the antisymmetric $\nu_{as}^{(\mathrm{OCO})}$ and symmetric stretching of vibration $\nu_{s}^{(\mathrm{OCO})}$ depends on the nature of the bond between the carboxylate and the oxide [137]. In particular, separations larger or significantly smaller than that in the free carboxylate ion (250–270 cm^{-1} for sodium formate [138]), are indicative of monodentate or bidentate (chelating or bridging) adsorptions respectively.

We have calculated the vibrational frequencies of adsorbed formate with and without the thick overlayer, by diagonalising the dynamical matrix. We have taken into account only the degrees of freedom of the adsorbed species, as we have found that the addition of underlying surface atoms gives negligible differences in the resulting frequencies (∼3 cm^{-1}).

The six intrinsic normal modes for the adsorptions on anatase with and without the 9 Å overlayer are reported in Table 4.5, where they are compared to data from experiments. When no overlayer is present, Δ for the bridging binding (184 cm^{-1}) agrees with the experiment (180 cm^{-1}). We note that different values of $\nu_{as}^{(OCO)}$ in MON(H) and BRI characterise the two adsorptions. This feature is present in the experimental spectrum of HCOOH on TiO_2 anatase [26], and confirms that monodentate and bridging structures are likely to coexist.

On the coated substrate, a very good match is obtained when comparing the BRI frequencies to the experimental peak positions [122]. Our Δ values for MON and BRI are respectively 256 and 250 cm^{-1}, the latter being very close to the experimental value of 249 cm^{-1} for formic acid on a-Al_2O_3. Thus, the vibrational frequencies for HCOOH on the bare and coated anatase lend further support to the structures predicted from the binding energies.

4.6 Adsorption of catechol

We have shown in subsection 3.6.1 that monodentate (aMON) and bridging (aBRI) are the most stable interactions of catechol on anatase (101). Here, we would like to investigate these two bindings on the a-Al_2O_3/TiO_2 substrate with the coating of 3 Å, in order to reveal whether moieties different from –COOH could also benefit from the a-Al_2O_3 overlayer.

To accomplish this, we have studied two monodentate, differing for the bind-

	0 Å			9 Å		
Type	MON(H)	BRI	exp^a	MON	BRI	exp^d
$\nu^{(CH)}$	3017	2978	2883	2956	3020	2894
$\nu_{as}^{(OCO)}$	1631	1515	1665/1550^b	1604	1632	1629
$\delta^{(CH)}$	1379	1369	1380	1381	1400	1392
$\nu_{s}^{(OCO)}$	1325	1331	1370^c	1348	1382	1380
$\pi^{(CH)}$	1017	1007	-	1020	1010	1061
$\delta^{(OCO)}$	785	705	-	718	705	788
Δ	306	184	180^c	256	250	249

Table 4.5: Vibrational frequencies (cm^{-1}) of HCOOH adsorbed on TiO_2 anatase (101) with and without the 9 Å a-Al_2O_3 overlayer. (a) data from Ref. [26]; (b) assigned to MON/BRI; (c) only the BRI value was detected; (d) the assignment of frequencies and experimental peaks for the coated system have been taken from Ref. [122], where the HCOOH was adsorbed on amorphous Al_2O_3. Adapted with permission from Ref. [129]. Copyright 2012 American Chemical Society.

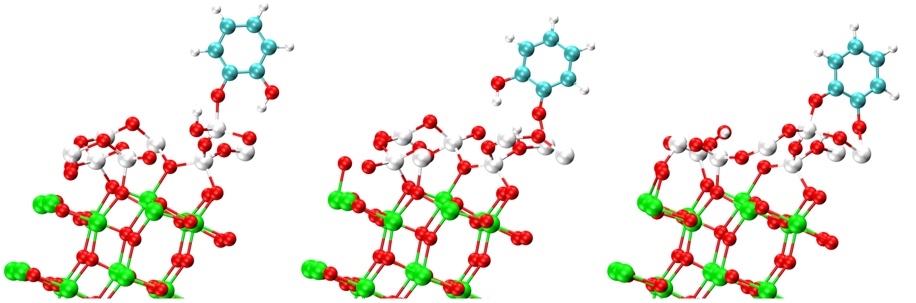

Figure 4.10: Relaxed structures of catechol adsorbed on the a-Al_2O_3/TiO_2 anatase (101) substrate: aMON1 (left); aMON2 (middle); aBRI (right). Ti are green, Al large white, O red, C cyan, H small white.

ing site (aMON1, aMON2), and one bridging adsorption (aBRI), whose optimised geometries are illustrated in Figure 4.10.

The effect of the overlayer on catechol is shown in Table 4.6. Both aMON1 and aMON2 are more stable than aMON on the bare substrate (-1.17 and -1.35 vs -0.81 eV), while their monodentate bonds are shorter by 0.1 Å. The stabilisation with the coating is even larger for the bridging aBRI, the most stable on anatase (101) (-1.00 eV). Its corresponding aBRI, whose bond lengths are asymmetric (1.76 and 2.00 Å), binds with an energy significantly lower (-3.04 eV).

	Bond distances (Å)			
Mode	B1	B2	M1	ΔE (eV)
aMON	-	-	1.84	-0.81
*a*MON1	-	-	1.74	-1.17
*a*MON2	-	-	1.73	-1.35
aBRI	1.85	1.85	-	-1.00
*a*BRI	1.76	2.00	-	-3.04

Table 4.6: Bond distances and adsorption energies for catechol in the monodentate and bridging modes with and without the 3 Å coating of *a*-Al_2O_3 on anatase (101). B1 and B2 are the bridging, M1 the monodentate bonds. The prefix "*a*" is used for the adsorptions on the amorphous coating, while those on bare anatase are shown with the same prefix "a" adopted in chapter 3.

We plot in Figure 4.11 the electronic structures of the three adsorptions, together with their projections on catechol and on the overlayer. The latter introduces some states into the band gap of anatase (101), but does not contribute to the bottom of its CB. It is interesting to notice that the *a*-Al_2O_3 coating does not have any influence on the main feature of catechol on TiO_2, i.e. the introduction of occupied molecular states in the gap. This suggests that after coating the TiO_2 film, the adsorption of catechol is improved, while a type II mechanism between catechol and TiO_2 may still be in action.

4.7 Adsorption of the N3 dye

In this section, we tackle the question of whether the results obtained for HCOOH can be generalised and extended to the larger common dyes binding through –COOH. To this end, we have investigated the effect of the overlayer on the binding energies of the N3 dye.

As the N3 dye is formed by 51 atoms, many more than catechol or formic acid, we had to employ a slab with a larger surface area (20.954 × 15.240 Å). Therefore, in order to keep the calculations affordable, we have reduced the thickness of the slab from 8 to 4 Ti-layers, including a total of 251 atoms. We have limited our study to two types of adsorptions, a double monodentate/bridging (BRIMON) and a monodentate (2MON) interaction, which have been shown to be between the most stable on anatase (101) [139]. The place-

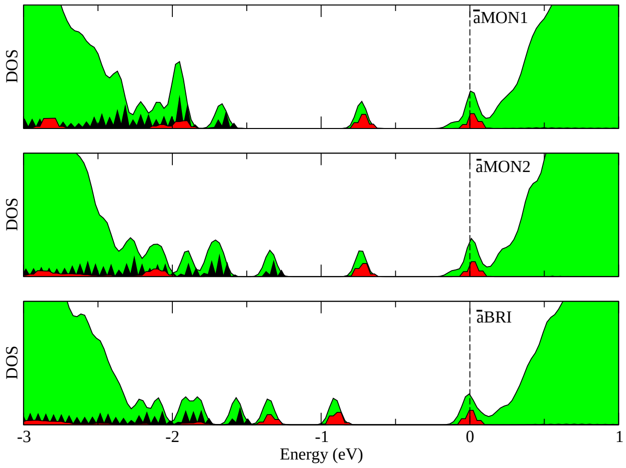

Figure 4.11: Electronic structures of the three modes of adsorption of catechol on the overcoated anatase (101). In green are plotted the total DOS (arbitrary units), in black and red, respectively, their projections on a-Al_2O_3 and catechol. The Fermi energies are marked by dashed lines.

ment of the proton in the monodentate linkage has been derived from the formic acid behaviour discussed in section 4.5 (i.e. on the dye for the bare anatase, on the surface for the overlayer).

The relaxed structures, with and without the overlayer are illustrated in Figure 4.12. From the adsorption energies and bond distances in Table 4.7, it is evident that, not only for HCOOH, but also for the entire N3 dye, the interaction is much stronger when the TiO_2 is coated by a layer of a-Al_2O_3.

In order to accommodate both the carboxyl groups to the crystalline substrate, the monodentate bonds are forced to maintain larger distances than with formic acid (2.24, 2.25 and 2.19 Å vs 2.13 Å). On the contrary, the amorphous substrate allows the N3 dye to accommodate both the carboxyl groups even at shorter monodentate distances than formic acid (1.78, 1.76 and 1.73 Å vs 1.83 Å). We have found negligible differences between the bridging bond lengths of N3 and HCOOH, in both substrates. This argument explains why for the bare TiO_2 the energies are higher than one would expect on the basis of the previous

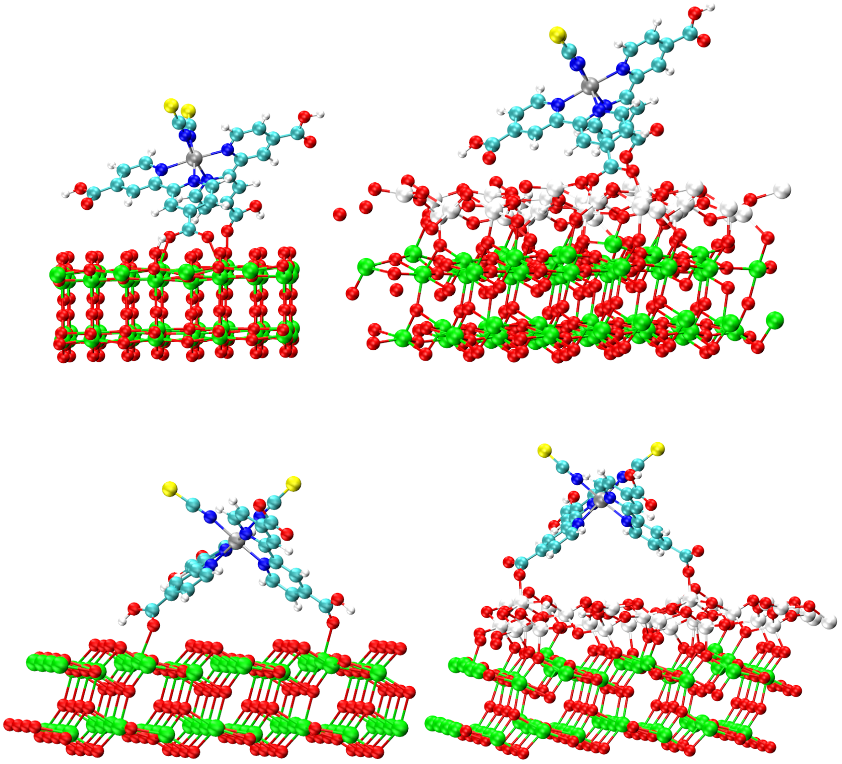

Figure 4.12: Relaxed structures of the N3 dye in the BRIMON (top) and in the 2MON (bottom) mode with and without the 3 Å a-Al_2O_3 coating on anatase (101). Ru are silver, Ti green, S yellow, Al large white, O red, N blue, C cyan, H small white. Reprinted with permission from Ref. [129]. Copyright 2012 American Chemical Society.

	Bond distances (Å)				
Mode	B1	B2	M1	M2	ΔE (eV)
BRIMON(TiO_2)	2.11	2.11	2.24	-	-1.08
BRIMON(Al_2O_3/TiO_2)	1.94	1.86	1.73	-	-5.35
2MON(TiO_2)	-	-	2.25	2.19	-0.98
2MON(Al_2O_3/TiO_2)	-	-	1.78	1.76	-4.58

Table 4.7: Bond distances and adsorption energies for the N3 dye in the BRIMON and 2MON modes with and without the 3 Å coating of a-Al_2O_3 on anatase (101). B1 and B2 are the bridging, M1 and M2 the monodentate bonds. Adapted with permission from Ref. [129]. Copyright 2012 American Chemical Society.

results on formic acid, while for the a-Al_2O_3/TiO_2 they are lower. Despite this quantitative deviation, we stress however that the adsorption of N3 reproduces qualitatively the trend already seen for formic acid, both the adsorptions being enormously stabilised in presence of the a-Al_2O_3 overlayer.

4.8 Summary of the chapter

In this chapter, we have presented a study of the a-Al_2O_3/TiO_2 anatase (101) substrate, which has been employed to adsorb formic acid, catechol, and the N3 dye.

We have generated the a-Al_2O_3 sample through the melt and quench *ab initio* technique, characterised it by its RDFs and electronic structures, and used to construct two models of the a-Al_2O_3/TiO_2 interface which differ in the overlayer thickness.

When no coating is present on anatase, both monodentate and bridging adsorptions of formic acid are in equilibrium. The effect of the overlayer, regardless of its thickness, is to considerably stabilise all of the adsorptions, while shifting the equilibrium towards the bridging, as confirmed by the vibrational analysis. The trend seen for formic acid can be extended also to catechol, for which we have predicted lower adsorption energies on the coated anatase.

The stronger interaction of carboxyl groups, confirmed by calculations on the entire N3 dye, supports the experimental attribution of a higher photocurrent to an enhanced adsorption of Ru-based dyes [66].

Chapter 5

Modelling ALD growth of Al_2O_3

5.1 Introduction

A possible way to grow an overlayer of Al_2O_3 on a nanocrystalline TiO_2 film is to make use of the surface sol-gel process [67]. With this technique, Palomares *et al* have reported an increase of 30% in the efficiency of DSSCs [55]. The sol-gel process, however, has a minimum achievable thickness of 10 Å, which gives poor control in the determination of the optimal thickness.

Compared to the sol-gel technique, ALD has a higher thickness resolution (around 1 Å). It is then the ideal solution to deposit uniform and monolayer Al_2O_3 films [68–73]. Alumina ALD, whose precursors are usually trimethylaluminium ($Al(CH_3)_3$, TMA) and H_2O, is based on the repetition of the two self-terminating half-reactions on the growing substrate:

1. $Al–OH^* + Al(CH_3)_3 \rightarrow Al–O–Al(CH_3)_2^* + CH_4$
2. $Al–O–Al(CH_3)_2^* + 2H_2O \rightarrow Al–O–Al(OH)_2^* + 2CH_4$,

where the asterisks represent the surface species.

In the attempt to go beyond the efficiency increase of the sol-gel process, Lin *et al* have employed Al_2O_3 ALD to overcoat anatase nanoparticles for DSSCs [74]. However, despite the potential advantages of ALD, the final 14% increase of efficiency was lower than the 30% already reported with the sol-gel technique [55]. In ref. [140, 141], Tien *et al* have ascribed the unsatisfactory results to a low Al_2O_3 coverage of the TiO_2 film, due in turn to the prevalence of the island growth mode during ALD [75]. A complete understanding of the growth mechanism of the Al_2O_3 overlayers is then an essential step towards further efficiency increases in DSSCs.

The knowledge of the mechanism is particularly crucial at subsurface defects of anatase. In their proximity, water binds more strongly than on the clean surface [142], and its desorption temperature is higher [143]. It has been estimated that 15% of the surface atoms could be located at step edges [24]. In particular, the existence of triangular islands, whose orientation is determined by two types of low energy monoatomic steps (abbreviated in Ref. [24] as D and B), has been shown by scanning tunnelling microscopy studies [144].

In this chapter, we first investigate the hydration of anatase (101) prior to ALD, both at the clean surface and step D, with the purpose of providing realistic models of the substrates. Then we move to the first half-reaction of ALD, described in the ideal process by:

$$\text{Ti–OH}^* + \text{Al(CH}_3)_3 \rightarrow \text{Ti–O–Al(CH}_3)_2{}^* + \text{CH}_4,$$

or

$$\text{Ti–(OH}_2)^* + \text{Al(CH}_3)_3 \rightarrow \text{Ti–O–Al(CH}_3)^* + 2\text{CH}_4,$$

where the asterisks represent the surface species. We compare the reaction pathways obtained for the (101) surface with those at steps. Despite some simplifications in the theoretical approach, we capture important insights into the adsorption of TMA, and provide a possible explanation to the incomplete and undesired coverage of the TiO_2 electrode.

5.2 *Ab initio* thermodynamics

Calculations within DFT do not include any effect of temperature or pressure. Thus, results should be used with care in applications where the temperature may be crucial, such as ALD. In describing experiments that are conducted at constant T and p, the appropriate thermodynamic potential to consider is the Gibbs free energy $G(T,p)$. The natural extension to DFT when its zero temperature energies enter in a suitable way into the calculation of $G(T,p)$ is *ab initio* thermodynamics [145]. In its illustration below, we will follow a derivation from Ref. [146].

The Gibbs free adsorption energy (which can also be interpreted as the surface free energy with respect to a clean surface) of N_{gas} molecules on a surface area A is defined as:

$$\Delta G = \frac{1}{A}\Big[G_{\mathrm{surf+gas}} - G_{\mathrm{surf}} - N_{\mathrm{gas}}\mu\Big], \tag{5.1}$$

where $G_{\mathrm{surf+gas}}$ and G_{surf} are respectively the Gibbs free energy of the surface with and without the gas, while μ is the chemical potential of the gas. We discuss separately the contributions to Eq. 5.1 in the solid and in the gas phase.

We decompose the solid phase Gibbs free energies according to

$$G = E + F^{\mathrm{vib}} + pV. \tag{5.2}$$

In Eq. 5.2, E is the total energy, while F^{vib} the vibrational free energy, which, for M nuclei in the harmonic approximation, can be expressed as:

$$F^{\mathrm{vib}}(T) = \sum_{i=1}^{3M}\Big[\frac{1}{2}\hbar\omega_i + kT\ln\Big(1-\exp\Big(-\frac{\hbar\omega_i}{kT}\Big)\Big)\Big], \tag{5.3}$$

where ω_i is a vibrational mode of the system.

The chemical potential of a gas of N molecules at temperature T and pressure p can be expressed as a function of its total partition function Z:

$$\mu(T,p) = (-kT \ln Z + pV)/N \tag{5.4}$$

For an ideal gas of indistinguishable molecules, Z can be written exactly by means of statistical thermodynamics. Thus, Eq. 5.4 becomes:

$$\mu(T,p) = E + \mu^{\mathrm{vib}}(T) + \Delta\mu(T,p) \tag{5.5}$$

where E is the total energy of a gas molecule, while the vibrational free energy $\mu^{\mathrm{vib}}(T)$ can be written in a way similar to Eq. 5.3.

We emphasise that the analytical expression for $\Delta\mu(T,p)$, which includes all the remaining temperature and pressure dependent terms, is known [146]. Alternatively, $\Delta\mu(T,p)$ can be derived from the experimental enthalphies $\Delta H(T,p^0)$ and entropies $\Delta S(T,p^0)$, at a reference pressure p^0, with respect to the $T = 0$ K limit [147]:

$$\Delta\mu(T,p) = \Delta H(T,p^0) - T\Delta S(T,p^0) + kT \ln \frac{p}{p^0}. \tag{5.6}$$

We are finally able to insert Eq. 5.2 and Eq. 5.5 into Eq. 5.1, and obtain a convenient formula for the Gibbs free adsorption energies:

$$\Delta G(T,p) = \frac{N_{\mathrm{gas}}}{A}\Big[\Delta e + \Delta f^{\mathrm{vib}}(T) - \Delta\mu(T,p)\Big], \tag{5.7}$$

where Δe is the binding energy per molecule at $T = 0$ K:

$$\Delta e = \Big[E_{\mathrm{surf+gas}} - E_{\mathrm{surf}} - N_{\mathrm{gas}}E_{\mathrm{gas}}\Big]/N_{\mathrm{gas}}, \tag{5.8}$$

while $\Delta f^{\mathrm{vib}}(T)$ is the vibrational contribution per molecule to the Gibbs free energy of adsorption:

$$\Delta f^{\mathrm{vib}}(T) = \Big[F^{\mathrm{vib}}_{\mathrm{surf+gas}} - F^{\mathrm{vib}}_{\mathrm{surf}} - N_{\mathrm{gas}}\mu^{\mathrm{vib}}\Big]/N_{\mathrm{gas}}. \tag{5.9}$$

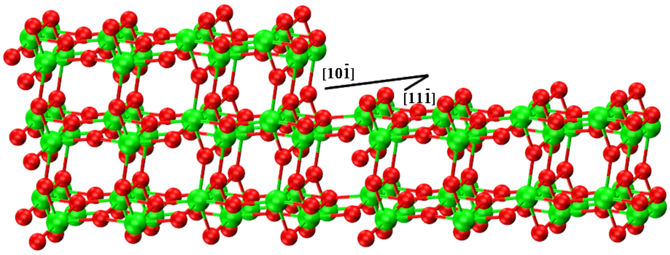

Figure 5.1: Unit cell of the step D of anatase (101) employed in the calculations. Ti are green, O red.

In passing, we mention that we have neglected the pV-term of Eq. 5.2, as insignificant compared to the binding energies [145].

Eq. 5.7 states that, when interested in the structure of a surface in contact with a gas at a given (T, p), we must evaluate, for a number of different configurations, the DFT binding energy Δe, and the smaller vibrational term $\Delta f^{\text{vib}}(T)$. We can then plot the Gibbs free energy of adsorption for each model as a function of the chemical potential (or temperature at a fixed pressure), yielding a straight line for each adsorption model considered. At any $\Delta\mu(T, p)$ (or T), the model with the lowest lying line can be identified as the most stable.

5.3 Computational details

The calculations in this chapter have been performed with the VASP 4.6.34 package [97,98]. We have used a computational setup similar to that in chapter 3, to which we refer for the details.

For the anatase (101) surface, we have chosen a (1×3) slab with a thickness of 8 Ti-layers, and dimensions of (10.477 × 11.430 Å). To model the step D of anatase (101), we have taken an orthorhombic (2×2) slab, with dimensions of (11.160 × 28.660 Å). This supercell has one vector orientated along [11$\bar{1}$], and a thickness of 6 Ti-layers. The monoatomic step edge was created by removing 16 of the 32 TiO_2 units from the top Ti-layer (Figure 5.1).

To take into account the effects of temperature and pressure in describing

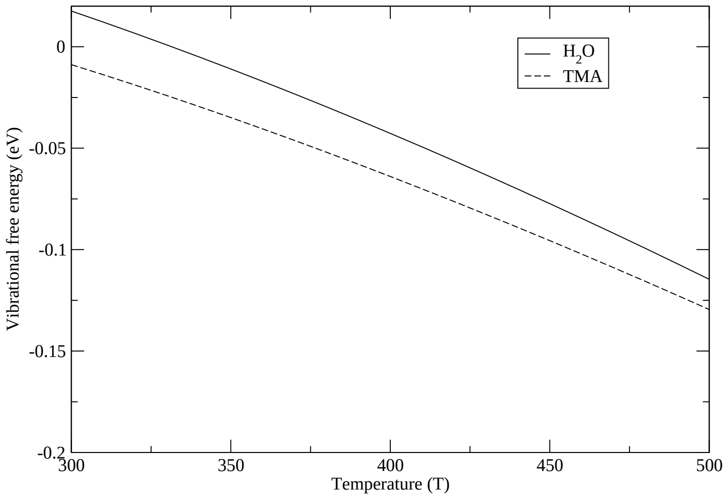

Figure 5.2: Estimated vibrational free energies of adsorption per molecule of water and TMA on anatase (101).

the adsorption of the precursors, we have followed the *ab initio* thermodynamics approach, illustrated in Section 5.2. In this framework, the Gibbs free adsorption energies are given by Eq. 5.7.

Evaluating exactly the free vibrational contribution (Eq. 5.9) would require a full calculation of the vibrational modes of the surface with and without the gas molecules. While this is in principle possible, phonon calculations are computationally expensive, as vibrational frequencies are very sensitive to the forces being accurate. This translates into numerous self-consistent iterations, each with a tight criterion for the stopping condition.

Figure 5.2 gives the idea of the order of magnitude of the free vibrational term for water and TMA adsorbed molecularly on anatase (101). We have neglected the changes in the vibrational modes of the surface atoms, and considered only those of the adsorbed molecules. This is in part justified by the fact that we expect the change in the modes of the atoms involved in the bond to be the most relevant. In our temperature range of interest, $\Delta f^{\mathrm{vib}}(T)$ favours the binding of the ALD precursors. We have verified that taking into account these estimates would shift negatively the final Gibbs free adsorption energies without affecting the physical conclusions. For this reason, similarly to Ref. [148], we have neglected phonons.

We have used Eq. 5.6 to calculate $\Delta\mu(T,p)$ of water. As tabulated enthalpy and entropy values were not available for TMA, we have calculated $\Delta\mu(T,p)$ following the analytical derivation of statistical thermodynamics [146].

5.4 Hydration of TiO_2 anatase prior to ALD

Before the first cycle of ALD starts, the anatase substrate is wetted with a pulse of H_2O vapour. In this section, in order to provide realistic models of substrates for the first half-reaction, we address the hydration of clean surface and step D of anatase (101).

5.4.1 Adsorption energies of water

There is experimental [149] and theoretical [148, 150] evidence that water is adsorbed molecularly on anatase (101), at any surface coverage. Based on this finding, we have decided not to investigate any dissociative adsorption on the clean surface, focussing on three different molecular coverages: 1/6 ML (low coverage), 1 ML (full coverage), and 2 ML (bilayer).

Table 5.1 compares the adsorption energies of water on anatase (101) at different sites and coverages with some previous results. At low coverage, water is adsorbed with an energy of −0.78 eV on a fivefold coordinated Ti (Figure 5.3, left), and forms two hydrogen bonds with a bridging O. In the full coverage, all of the rows of fivefold coordinated Ti are saturated (Figure 5.3, middle), but the bridging O can not accommodate two hydrogen bonds together, causing a rotation of the water molecules along $[10\bar{1}]$, and a decrease of the adsorption energy to −0.73 eV. The bilayer coverage is obtained by adsorbing rows of water along [010], between the rows of saturated fivefold coordinated Ti (Figure 5.3,

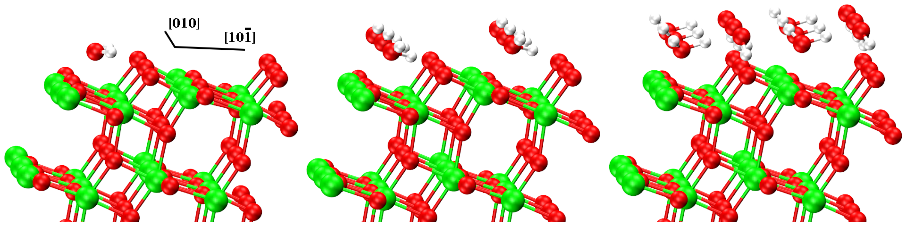

Figure 5.3: Optimised structures of water adsorption on the clean (101) anatase surface at 1/6 ML (left), 1 ML (middle), and 2 ML (right) coverage. Ti are green, O red, H white. Reproduced from Ref. [151].

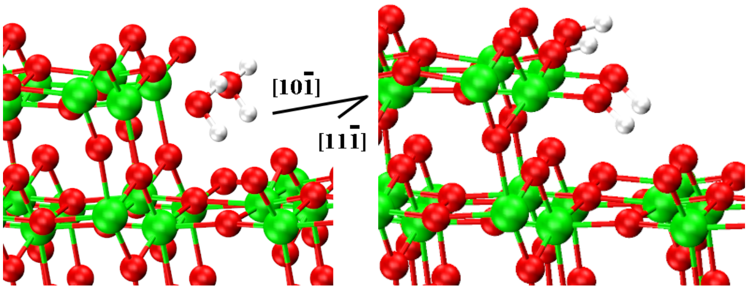

Figure 5.4: Optimised structures of molecular (left) and dissociative (right) adsorption of water on step D of anatase (101) at 1 ML coverage. Ti are green, O red, H white. Reproduced from Ref. [151].

right). The added molecules form two hydrogen bonds with two bridging O and a third with a water of the adjacent [010] row. The new pattern of hydrogen bonds extending along $[10\bar{1}]$ slightly strengthens the adsorption to -0.76 eV. Considering all the different structures, the adsorption energy dependence on the water coverage follows a trend which is in agreement with the literature [148, 150].

On step D, we have investigated both molecular and dissociative adsorption of water. In the first case, water molecules were adsorbed at fivefold coordinated step Ti. In the second, a H atom was transferred to the nearest twofold coordinated step O. At full coverage, a molecular adsorption (Figure 5.4, left) is slightly favoured (-1.02 eV) over a dissociative one (-1.00 eV) (Figure 5.4, right), in agreement with a previous study [24]. The molecular and dissociative energies are less close when moving from a full to a half hydroxylated step, being respectively -1.04 and -0.95 eV.

		Δe (eV)	
Site	Coverage	Mol	Diss
Terrace	low	-0.78	
		-0.74 [150]	
		-0.77 [148]	
	full	-0.73	
		-0.72 [150]	
		-0.73 [148]	
	bilayer	-0.76	
		-0.81 [148]	
StepD	half	-1.04	-0.95
	full	-1.02	-1.00
		-1.12 [24]	-1.04 [24]

Table 5.1: Adsorption energies of water at different coverages and sites of anatase (101). Adapted from Ref. [151].

5.4.2 Gibbs free adsorption energies of water

The adsorption energies in Table 5.1 are valid only at zero temperature and pressure. However, since the hydration degree of any surface depends on the temperature and partial pressure of the water, we plot in Figure 5.5 the Gibbs free adsorption energies of water on anatase (101) as a function of T, at the typical ALD pressure of 1 torr (Eq. 5.7). Each line corresponds to a different water coverage, and the horizontal line marks the zero desorption value of the bare surface. It can be seen that for temperatures above 350 K the surface is already dehydrated. This finding is fundamental, because implies that, at the typical ALD temperature of 423 K [74], water molecules are already desorbed. Accordingly, we expect the first half-reaction, i.e. the adsorption of TMA, to take place on a dehydrated anatase (101) surface. In passing, we mention here that a desorption temperature of 445 K, agreeing with that reported by Arrouvel *et al* [148], is recovered when the standard vapour pressure (760 torr) is used.

Lin *et al* have established a graphical model for the first-half reaction of alumina ALD on anatase (101) [74]. In this model, Ti–OH groups react with TMA, form TiO–Al–$(CH_3)_2$ groups and release one CH_4 molecule. Our finding, predicting water desorption at temperatures much lower than the experimental ones, is at odds with this model.

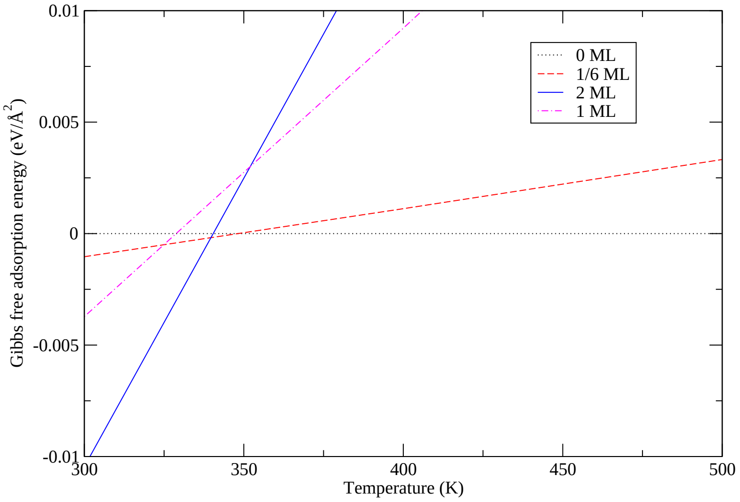

Figure 5.5: Gibbs free adsorption energies with respect to the temperature (p = 1 torr) for different coverages of molecularly adsorbed water on anatase (101).

A different picture emerges from the adsorption of water on step D, one of the most characteristic defects of anatase (101). We have shown that at these sites water is preferentially adsorbed molecularly. Figure 5.6 shows the Gibbs free adsorption energy for different coverages of molecular water at step D. It can be seen that water is desorbed at temperatures around 450 K, 100 K higher than at the clean surface, and, more importantly, above typical ALD working temperatures. In the next section, we will show that the presence of water deeply affects the subsequent half-reaction of the first ALD cycle, and can explain the island growth mode observed during experiments [140, 141, 152].

5.5 The first half-reaction of ALD

We have shown in subsection 5.4.2 that *ab initio* thermodynamics predicts a dehydrated anatase (101) surface as a substrate for the first metal precursor pulse. On the contrary, at step D, although some dissociated water is likely to be

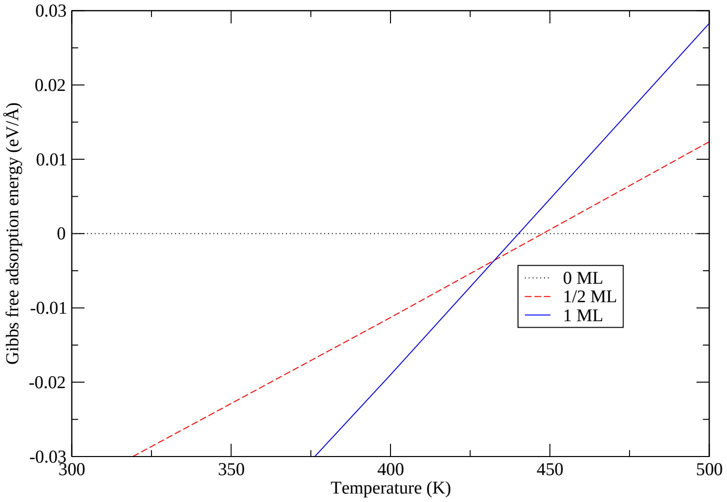

Figure 5.6: Gibbs free adsorption energies with respect to the temperature ($p = 1$ torr) for different coverages of molecularly adsorbed water on step D of anatase (101).

Label of Figure 5.7	Δe (eV)
T1	-1.04
T2	-0.54

Table 5.2: Energetics with respect to the desorbed state (at $T = 0$ K) for the adsorption of TMA on bare anatase (101) Adapted from Ref. [151].

present, the most thermodynamically stable configuration is 1 ML of molecularly adsorbed water. Accordingly, we have employed the two expected models for the adsorption of TMA. In this section, we first calculate the adsorption energies at zero temperature, and then use Eq. 5.7 (without normalising to the surface area A) to take into account the effects of pressure and temperature.

5.5.1 Adsorption energies of TMA

Figure 5.7 and Table 5.2 report the $T = 0$ K structures and binding energies for the adsorption of TMA on the bare surface. When a TMA molecule is adsorbed here (Figure 5.7, T1), the reaction is exothermic (-1.04 eV) and does

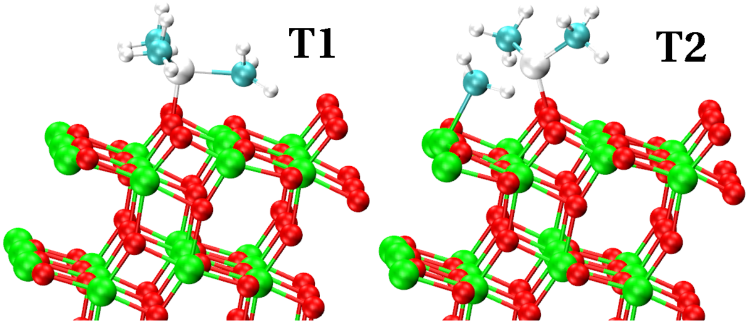

Figure 5.7: Potential energy minima structures for the adsorption of TMA on the bare anatase (101) surface: molecular (T1) and dissociative adsorption (T2). Ti are green, Al large white, O red, C cyan, H small white. Reproduced from Ref. [151].

not present any barrier. The final Al–O distance is 1.84 Å, and one CH_3 group interacts with a fivefold coordinated Ti, which relaxes upwards by 0.19 Å. As a result, the CH_3–Al bond is more stretched compared to the gas phase (2.13 vs 1.96 Å). We have also considered the possibility of a dissociative adsorption of TMA (Figure 5.7, T2). In this mode, still exothermic (-0.54 eV), but less favoured than molecular adsorption, the dissociated CH_3 group is bonded to a fivefold coordinated Ti below (2.22 Å). The latter moves by 0.45 Å upwards, implying that an interaction between the two fragments, separated by a distance of 2.54 Å, is still present.

Elliott *et al* have investigated the adsorption of TMA on bare Al_2O_3, and reported a binding energy of -1.2 eV [70]. They have found TMA to dissociate in one $AlCH_3$ and two CH_3 fragments. This final state, at an energy 2.4 eV lower than molecular adsorption, was the only to be stable against desorption. Here, we find instead that TMA is adsorbed molecularly, and no further stabilisation is achieved when the molecule is decomposed. This will have important consequences when the competition with desorption is taken into account.

Figure 5.8 and Table 5.3 show the $T = 0$ K structures and energies for the adsorption of TMA on step D. When TMA is adsorbed on the bridging O close to the edge, the relaxed structure is identical to the one at the flat surface (Figure 5.8, S1), with an Al–O distance of 1.83 Å. The interaction between a

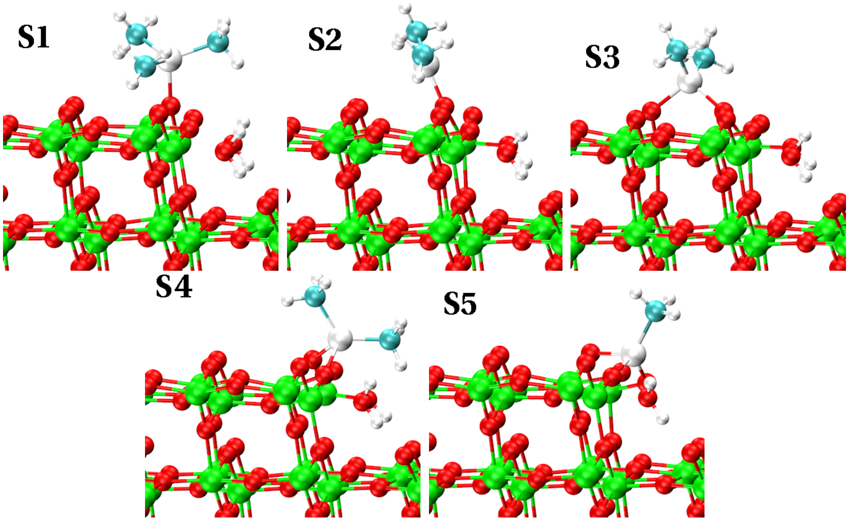

Figure 5.8: Potential energy minima structures for the adsorption of TMA on the hydrated step D: $Al(CH_3)_3$ at the bridging O (S1), $Al(CH_3)_2$ following elimination of one CH_4 (S2), $Al(CH_3)_2$ following relaxation towards the surface (S3), $Al(CH_3)_2$ following relaxation towards step D (S4), $AlCH_3$ following elimination of two CH_4 (S5). Ti are green, Al large white, O red, C cyan, H small white. Reproduced from Ref. [151].

Label of Figure 5.8	Δe (eV)
S1	−1.05
S2	−1.47
S3	−2.13
S4	−2.04
S5	−3.00

Table 5.3: Energetics with respect to the desorbed state of the adsorption of TMA on the step D of anatase (101). Adapted from Ref. [151].

CH_3 group and a fivefold coordinated Ti is still present, and causes a stretching of the CH_3 bond with the Al, like in the flat surface. Coherently, we find a similar adsorption energy of -1.05 eV (only 0.01 eV lower than at the clean surface). From this structure, a methyl group can accept a hydrogen from a near water molecule and desorb as CH_4. In the relaxed structure (Figure 5.8, S2), the Al presents a planar coordination, and binds the bridging O with a distance of 1.75 Å. The resulting reaction energy is of -0.42 eV. Despite this configuration being stable, we have identified at least two other configurations with a lower energy. In the first (Figure 5.8, S3), $Al(CH_3)_2$ moves towards the surface, and bonds to a second bridging O in a tetrahedral structure. The corresponding gain of energy is of -0.66 eV. In the second (Figure 5.8, S4), with an energy gain of -0.57 eV, the $Al(CH_3)_2$ group moves towards the edge, making an additional bond to a twofold coordinated step O, and creating again a tetrahedral structure. Unlike in S3, here, another CH_3 group is in proximity of the remaining OH group at the step, from which a second H can be transferred. To test this possibility, we have optimised the structure of a double CH_4 desorption (Figure 5.8, S5). In S5, the remaining $AlCH_3$ group replaces the previous bond to the methyl group with a third bond to the O of the original water. This second desorption gives an additional stabilisation of -0.96 eV, and brings to -3.00 eV the total gain of energy compared to the desorbed TMA.

5.5.2 Gibbs free adsorption energies of TMA

Figure 5.9 shows the Gibbs free adsorption energies for the adsorption of TMA on the clean anatase (101). It can be noticed that a molecular adsorption (T1) is endothermic (+0.3 eV), and, contrary to what happens on the bare Al_2O_3 substrate [70], a stabilisation through decomposition (T2) is precluded (+0.8 eV). As a consequence, at typical ALD conditions, the desorbed configuration (T0) will be the most stable, with TMA being unreactive towards anatase (101).

Figure 5.10 illustrates the Gibbs free adsorption energies on step D. As anticipated, despite the molecular adsorption being still endothermic (S1), here,

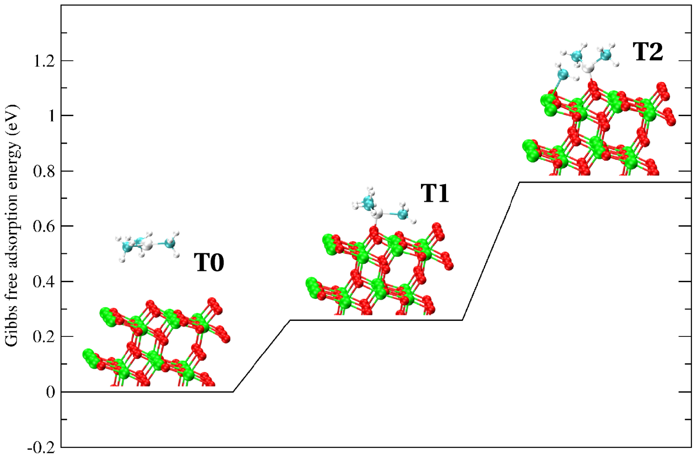

Figure 5.9: Gibbs free adsorption energy profile for TMA on bare anatase (101). T0 represents the desorbed state, the other labels are identical to Figure 5.7. Reproduced from Ref. [151].

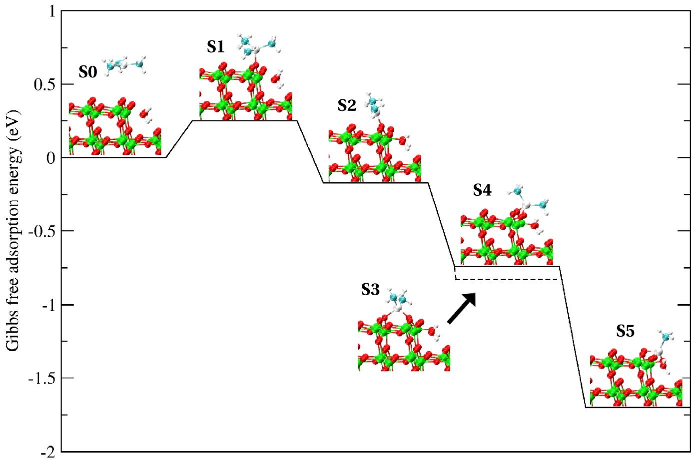

Figure 5.10: Gibbs free adsorption energy profile for TMA on the fully hydrated step D of anatase (101). S0 represents the desorbed state, the other labels are identical to Figure 5.8. From S2 the system can be stabilised to S3 (dashed line) or proceed towards S4 and S5. Reproduced from Ref. [151].

the presence of neighbouring H_2O molecules leads to striking differences. Provided the reaction barrier is not too high, water molecules can indeed react with TMA, making possible the elimination of a CH_4 group (S2). It is the desorption of this CH_4 which allows negative Gibbs free adsorption energies to be reached. S3 (dashed line at -0.8 eV) and S4 levels have been further stabilised by the rearrangements of the remaining $Al(CH_3)_2$. From S4, a second methyl group can desorb (S5), bringing to a final stabilisation of -1.7 eV compared to the desorbed state S0. Accordingly, at the end of the TMA pulse, we predict the step D to be in configurations S3 and S5, i.e. covered by a mixture of $Al(CH_3)_2$ and $AlCH_3$ groups ready to react with the subsequent water pulse of the second ALD half-reaction.

Together, Figures 5.9 and 5.10 help to understand the growth mechanism of the Al_2O_3 ALD on anatase (101). After the first half-reaction, some Al are retained only in proximity of steps D, which act as nucleation centres. These findings agree with the experimental observation of an island growth mode [140, 141, 152], which imposes a lower bound of 5-10 layers to the number of ALD cycles, if a uniform coating is to be obtained. Our mechanism suggests that lower temperatures or higher water partial pressures may help to retain more water on the surface, promoting thus ALD.

It is worth noting that at a given temperature and pressure, the only factor influencing the coverage of water is its adsorption energy (from -0.7 to -0.8 eV on the surface, below -1 eV on step D). We have carried out test calculations on the adsorption of water near subsurface Ti interstitials and O vacancies, obtaining adsorption energies lower than -1 eV, in line with the literature [143]. This suggests that, after the first hydration, some water is retained also at these sites. Therefore, it is likely that subsurface point defects have a role similar to step D, acting as nucleation sites where TMA is adsorbed and stabilised with an analogous mechanism.

5.6 Summary of the chapter

We have investigated the water pulse and the subsequent first half-reaction of alumina ALD on anatase (101). Our results predict that, at typical ALD working conditions, one should expect some water to be retained only at defects.

Depending on the availability of water, and hence on the adsorption site, different pathways are possible after the TMA pulse. On the flat surface, desorption is favoured over adsorption. At defects, acting as nucleation centres for the island growth mode, TMA interacts with the adjacent molecules of water and the endothermic chemisorption can be stabilised by the elimination of one or two CH_4.

Our calculations help to understand the growth mechanism of the Al_2O_3 ALD on TiO_2 anatase (101) and explain the experimental difficulties faced in depositing continuous single layers.

Chapter 6

Excitations of natural dyes by ΔSCF

6.1 Introduction

One of the key parameters in the development of a new dye is the absorption spectrum, which one would like to tune to the solar spectrum. The calculation of absorption spectra is one of the main problems of computational chemistry. TDDFT provides localised valence excitations which are usually accurate to within 0.3 eV [153, 154]. The drawback of TDDFT are charge transfer excitations [155], and approaches like constrained DFT [156], where an external potential is added to fulfil a desired constraint on the density, have been proposed to overcome the difficulty [157–159].

Δ self-consistent field (ΔSCF) is one of the earliest methods for the calculation of excitation energies in Hartree-Fock [76, 77]. These are calculated by promoting one electron into a virtual orbital, and solving the equations for the constrained configuration. The applicability to DFT, where the excited states can be calculated by populating different KS levels, is then straightforward [160], at a cost not very different from the ordinary ground state theory.

ΔSCF has been shown to give satisfactory results for the potential energy surfaces (PESs) of H_2 and NaCl [160], the vertical excitations of N_2 and CO [161], and CO adsorbed on Pd(111) [160]. A surprising similar accuracy to TDDFT has been observed for a test set of vertical excitation energies of 16 chromophores [162], and the use ΔSCF to investigate the isomerisation dynamics of azobenzene has yielded PESs that agree very well with those derived from TDDFT [163].

In this chapter, we describe the intuitive idea behind ΔSCF, which we have implemented in CONQUEST [78–80]. We report some tests on the lowest PESs of CO and the vertical excitation energies of catechol. Then we move to anthocyanidins. We have studied the effect of hydroxy substitutions and pH on their lowest excitations. To reproduce a typical DSSC interface, we have adsorbed one anthocyanidin on TiO_2 anatase (101), focussing on the resulting shift of the excitation energy. Finally, we show that it is possible to relax a molecule in its excited state by simply taking the ΔSCF gradient.

6.2 The ΔSCF method in DFT

We recall that the ground state density $n(\mathbf{r})$ of a system of N electrons can be found by solving the KS equations:

$$H_{\mathrm{KS}}\psi_i(\mathbf{r}) = \varepsilon_i\psi_i(\mathbf{r}), \tag{6.1}$$

and taking the square sum of the resulting KS orbitals:

$$n(\mathbf{r}) = \sum_{i=1}^{\infty} f_i|\psi_i(\mathbf{r})|^2, \tag{6.2}$$

where only the lowest N orbitals contribute (f_i equals 1 if $i \leq N$, 0 otherwise). As H_{KS} is itself a functional of the density, Eq. (6.1) and (6.2) must be solved in a self-consistent way.

Once the set of the KS orbitals has been calculated, a very intuitive way to simulate an excitation in a molecule is to promote one electron from an occupied ψ_k ($k \leq N$) to a virtual orbital ψ_l ($l > N$). The new density $n^{\mathrm{exc}}(\mathbf{r})$, calculated from Eq. (6.2) with $f_k = 0$ and $f_l = 1$, can be used to construct an excited Hamiltonian $H^{\mathrm{exc}}_{\mathrm{KS}}(\mathbf{r})$ and set up new KS equations:

$$H^{\mathrm{exc}}_{\mathrm{KS}}\psi_i(\mathbf{r}) = \varepsilon_i\psi_i(\mathbf{r}), \tag{6.3}$$

These are solved again self-consistently, with the restriction of maintaining the $\psi_k \rightarrow \psi_l$ excitation at every iteration.

Within ΔSCF, the calculation of triplet energies, E_{T}, is immediate. In a system where all the orbitals are doubly occupied, except for the two highest orbitals ψ_a and ψ_b which are singly occupied by electrons of spin α, the $S_z = 1$ triplet configuration from a Slater determinant is:

$$^3_1\Psi = \frac{1}{\sqrt{2}}[\psi_a(\mathbf{r}_1)\psi_b(\mathbf{r}_2) - \psi_a(\mathbf{r}_2)\psi_b(\mathbf{r}_1)]\alpha(s_1)\alpha(s_2). \tag{6.4}$$

Here, we have indicated with s_1 and s_2 the spin coordinates of the unpaired electrons having spatial coordinates $\mathbf{r}_1$ and $\mathbf{r}_2$, while neglected the irrelevant closed shell orbitals. ΔSCF calculates triplet energies by a self-consistent run in this spin-constrained configuration.

Singlet energies, E_{S}, are not directly accessible by single determinants and are thus obtained by means of the sum method [164]. In particular, in a configuration where ψ_a and ψ_b are both singly occupied by electrons of spin α and β respectively, the corresponding spin mixed configuration from a Slater determinant is:

$$^{\mathrm{MIX}}\Psi = \frac{1}{\sqrt{2}}[\psi_a(\mathbf{r}_1)\beta(s_1)\psi_b(\mathbf{r}_2)\alpha(s_2) - \psi_a(\mathbf{r}_2)\beta(s_2)\psi_b(\mathbf{r}_1)\alpha(s_1)], \tag{6.5}$$

whose energy E_{MIX} can be calculated by a second spin-constrained ΔSCF run. Since $^{\mathrm{MIX}}\Psi$ is given by an equal combination of the $S_z = 0$ triplet and singlet, respectively ${}^3_0\Psi$ and ${}^1_0\Psi$:

$$ {}^{\mathrm{MIX}}\Psi = \frac{1}{2}({}^3_0\Psi +{}^1_0 \Psi), \tag{6.6}$$

the following expression for E_{MIX} holds when the triplets are degenerate:

$$E_{\mathrm{MIX}} = \frac{1}{2}(E_{\mathrm{S}} + E_{\mathrm{T}}), \tag{6.7}$$

which provides a spin purification formula for E_{S}.

6.3 Computational details

We have performed the calculations in this chapter with the CONQUEST code [78–80], which solves the KS equations by diagonalising the Hamiltonian matrix in a pseudo-atomic orbital basis. The code has been developed by our group, which has made more simple the addition of ΔSCF. We have used the local spin density approximation (LSDA) [89] of the exchange-correlation functional, Troullier-Martins pseudopotentials [165], and a DZP basis set (15 PAOs for Ti, 13 for C and O, and 5 for H). Relaxations of structures were performed with a quasi-Newton method, and stopped when the force acting on each nucleus was less than 0.05 eV/Å.

To model TiO_2 anatase (101), we have used a (1×2) surface unit cell, with a thickness of 4 Ti-layers, and dimensions of $(10.073\times7.450$ Å). As these are very close to the surface dimensions of anatase (101) in chapter 3, we have adopted the same $(1 \times 2 \times 1)$ **k**-point grid.

By means of ΔSCF, we reproduce an excitation from the highest occupied to the lowest unoccupied level of the dye, i.e. a HOMOdye → LUMOdye excitation, typical of sensitisers in DSSCs. Since during the self-consistent procedure the position of HOMOdye and LUMOdye with respect to the TiO_2 levels can change, it is important to "follow" the excitation and determine at every iteration HOMOdye and LUMOdye. To this end, we spatially locate the KS orbitals

ψ_j and assign them either to the dye or to the surface by expanding ψ_j with respect to the PAOs:

$$\psi_j = \Sigma_\alpha c_{j\alpha}\phi_\alpha + \Sigma_\beta c_{j\beta}\phi_\beta, \tag{6.8}$$

where ϕ_α and ϕ_β are the PAOs centred respectively on the atoms of the dye or the oxide. By summing over the squared coefficients $|c_{j\alpha}|^2$ and $|c_{j\beta}|^2$ we obtain two coefficients which reflect the localisation of ψ_j:

$$D_j = \Sigma_\alpha |c_{j\alpha}|^2, \tag{6.9}$$

and

$$O_j = \Sigma_\beta |c_{j\beta}|^2. \tag{6.10}$$

Their comparison allows the assignment of the orbitals.

6.4 Tests on pseudopotentials and basis set

In this section, we present the tests on the pseudopotentials and the DZP basis set used in this chapter. We start with catechol, as its ring is part of many anthocyanidins. In addition, basis sets and pseudopotentials for Ti and O were tested on anatase lattice parameters.

6.4.1 Catechol geometry

We have derived the main geometrical parameters of catechol in gas phase, and compared them with some previous GGA-DFT results [118] (Table 6.1). It is evident that a DZP basis set together with LDA pseudopotentials reproduce well the structure already reported in the literature, which makes it suitable to the investigation of anthocyanidins.

Bonds	GGA-DFT [118]	LDA-DFT
C1C2	1.42	1.41
C2C3	1.40	1.39
C3C4	1.41	1.41
C4C5	1.40	1.40
C5C6	1.40	1.40
C6C1	1.40	1.40
C1O1	1.37	1.35
C2O2	1.37	1.37
Angles		
C1C2C3	120.0	120.9
C2C3C4	120.1	119.3
C3C4C5	119.9	120.0
C4C5C6	120.0	120.6
C5C6C1	120.3	119.7
C6C1C2	119.6	119.5
O1C1C2	121.6	118.3
O2C2C3	124.3	126.1
Dihedrals		
H1O1C1C2	+0.1	−1.3
H2O2C2C3	+0.0	+0.7

Table 6.1: Geometrical parameters of gas phase catechol compared to the results in the literature. Labels refer to Figure 3.9.

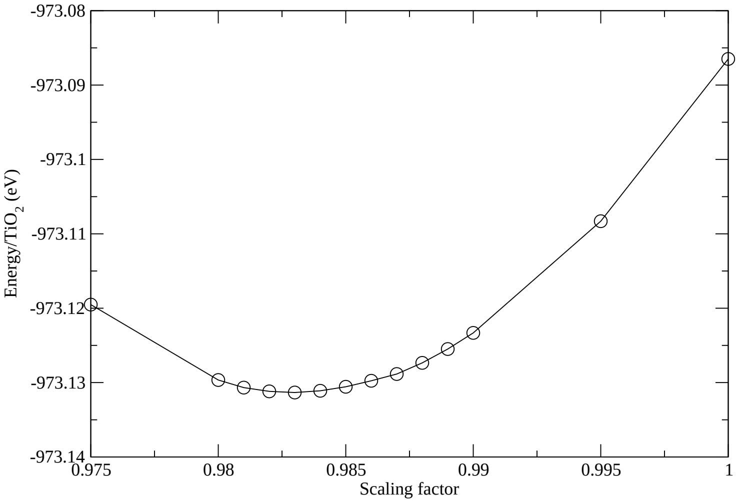

Figure 6.1: Energy/TiO_2 unit of bulk anatase as a function of the volume of the unit cell. The x-axis is the scaling factor with respect to the experimental volume of Ref. [109].

6.4.2 TiO_2 anatase lattice parameters

In order to test the LDA pseudopotentials and the DZP basis set on the lattice parameters of anatase, we have performed a series of optimisations where the experimental lattice parameters and the coordinates of the atoms have been multiplied by a scaling factor (Figure 6.1). The lattice vectors corresponding to the lowest energy configuration of TiO_2 anatase, a_2 and c_2, are respectively 3.718 and 9.340 Å. As expected for LDA, they underestimate the experimental values (-1.7%), which validates the pseudopotentials and basis set of Ti and O to study TiO_2 anatase.

6.5 Testing ΔSCF

Before using ΔSCF for large systems, we have tested its implementation on the CO molecule and the catechol dye. A LDA-ΔSCF study on CO is already

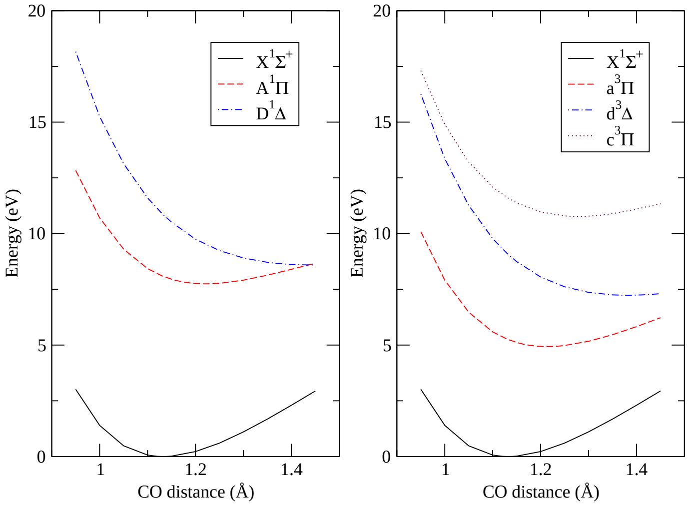

Figure 6.2: Potential energy surfaces for the ground and the lowest singlet (left) and triplet (right) excited states of CO obtained by ΔSCF.

present in the literature [161]. For this reason, the CO dimer is particularly convenient for our purposes.

6.5.1 CO molecule

We have studied the ground and a few excited singlet and triplet PESs of CO, from which we have extracted the vertical excitation energies and the position of the minima.

We have taken the transition configurations of the excited states from a previous TDDFT work [166] with the LDA functional. As both the 1π and 2π orbitals are doubly degenerate, when involved in the excitations, we have removed or added half electron in each of them. Due to the small number of PAOs, we have found a DZP basis set not enough to achieve convergence, and the results presented have been obtained with a triple-ζ double polarised basis set (22 PAOs for both C and O).

From the PESs of Figure 6.2, we have obtained the equilibrium bond lengths

State	Transition	ΔSCF	TDDFT [167]	exp [168]
$X^1\Sigma^+$	-	1.13	-	1.128
$A^1\Pi$	$5\sigma \to 2\pi$	1.22	1.24	1.235
$a^3\Pi$	$5\sigma \to 2\pi$	1.21	1.20	1.206
$D^1\Delta$	$1\pi \to 2\pi$	1.44	1.38	1.399
$d^3\Delta$	$1\pi \to 2\pi$	1.38	1.38	1.370
$c^3\Pi$	$4\sigma \to 2\pi$	1.28	1.25	1.348

Table 6.2: Equilibrium bond lengths (Å) of the ground and lowest excited states of CO.

State	Transition	ΔSCF	ΔSCF [161]	TDDFT [166]	exp [168]
$A^1\Pi$	$5\sigma \to 2\pi$	8.10	7.84	8.25	8.51
$a^3\Pi$	$5\sigma \to 2\pi$	5.26	6.09	6.02	6.32
$D^1\Delta$	$1\pi \to 2\pi$	10.90	10.82	10.02	10.23
$d^3\Delta$	$1\pi \to 2\pi$	9.11	9.72	9.24	9.36
$c^3\Pi$	$4\sigma \to 2\pi$	11.62	12.26	11.43	11.55

Table 6.3: Vertical excitation energies (eV) of the lowest excited states of CO.

(Table 6.2), in qualitative agreement with TDDFT [167] and experiment [168], and the vertical excitation energies (Table 6.3). For some excitations, our results deviate from the previous ΔSCF work [161], which could be due to the use of PAOs instead of plane waves. The agreement with the literature is however very good, and we are confident in the implementation of the method.

6.5.2 Free and Ti-bound catechol

As a second test, we have calculated the excitation energies of free and Ti-bound catechol.

The lowest energy band $S_0 \to S_1$ of free catechol is dominated by a HOMO → LUMO transition [31, 107]. Experimentally, binding catechol to Ti does not cause any shift of the spectrum, as a new low energy $S_0 \to$ Ti band appears instead [36]. In the Ti-bound catechol, the excitation corresponding to $S_0 \to S_1$ is between orbitals which are nearly identical to those of free catechol [31]. The vertical excitations of free and Ti-bound catechol are presented in Table 6.4. In both systems, ΔSCF improves the KS difference between HOMOdye and LUMOdye, and reproduces the position of the peak with good accuracy.

	Free	Ti-bound
KS	4.10	4.17
ΔSCF	4.50	4.41
TDDFT [31]	4.77	4.86
Exp [36]	4.59	4.59

Table 6.4: Excitation energies of free and Ti-bound catechol compared to the results in the literature.

As well as the calculation of excitation energies, an interesting application of ΔSCF is the relaxation of a molecule in its excited state. To this end, we can make use of the Hellmann-Feynman theorem to find forces, and relax the structure in the excited BO surface without any important modification of the main DFT code.

After updating the nuclei, one could solve again for the ground state density and then re-excite the electron, or looking directly for self-consistency of the excited state density. We have chosen the second approach, as tests have shown that it halves the computational time, while the differences in all of the bond lengths between the two procedures are always less than 0.01 Å.

We have mentioned that the lowest optical band of free catechol is dominated by a single electronic excitation, primarily of the HOMO → LUMO origin [31, 107]. Accordingly, we have employed HOMO and LUMO of the same spin channel to promote the electron and relax the dye by ΔSCF.

The deviations of the main geometrical parameters of catechol from the ground state are reported in Table 6.5, where they are compared with some previous results from the literature [118]. As for the ground state, we find the benzene ring to be planar. The most important changes are given by the increase of all of the CC bond distances. On the contrary, the CO lengths become smaller. Also the bond angles modify their values, with differences up to almost 6 degrees for C2C3C4 and C5C6C1. With the exception of the two dihedrals H1O1C1C2 and H2O2C2C3, the described trend agrees very well with the one in the literature [118], and suggests that ΔSCF can be used as a simple tool for the calculation of excited state geometries.

At this point, we would like to report an unsuccessful attempt to study the catechol/TiO_2 system in the excited state of the dye. In our calculations, LUMOdye corresponds to LUMO+43, and has an energy of 4.82 eV with respect to the bottom of the CB of the oxide. LUMOdye mixes with the continuum of levels of TiO_2, as indicated by its expansion coefficients D_L and O_L (Eqs. 6.9 and 6.10), respectively 1.0 and 0.5 for catechol and TiO_2. In this case, an assignment of LUMOdye based on the physical localisation of the orbitals is necessarily weak. Moreover, during the excited state self-consistent run, the position of LUMOdye varies discontinuously, because the values of D_j and O_j are very close to each other, and oscillate in many orbitals. We believe that the hybridisation of the LUMOdye with the continuum of states of the oxide is the source of lack of self-consistency.

One possible way to tackle the problem is to extend ΔSCF to allow excited electrons to occupy linear combinations of KS states. This approach has been shown to perform better than standard ΔSCF when the molecular orbitals hybridise with the surface [161]. Despite intriguing, we have not explored this possibility, both because of lack of time and because we have not experienced any issues in the adsorption of the cyanidin dye (subsection 6.6.3). For the latter, LUMOdye is always situated below the CB, and two orders of magnitude separate D_L from O_L.

6.6 Anthocyanidins

Among the natural dyes, anthocyanins and anthocyanidins are phenolic compounds responsible for the colour of many fruits and vegetables. Both anthocyanins and anthocyanidins have been traditionally employed in DSSCs, with low but promising efficiencies up to 1% [45–49].

Anthocyanidins consist of two aromatic rings (A and C) bonded to a third aromatic ring (B) (Fig. 6.3). If a sugar group is present at position R_1, anthocyanidins are known as anthocyanins, whose optical properties are very simi-

Bonds	TDDFT [118]	ΔSCF
C1C2	+0.02	+0.01
C2C3	+0.04	+0.04
C3C4	+0.00	+0.02
C4C5	+0.02	+0.02
C5C6	+0.00	+0.01
C6C1	+0.04	+0.05
C1O1	−0.02	−0.02
C2O2	−0.01	−0.02
Angles		
C1C2C3	+0.6	+2.2
C2C3C4	−3.0	−5.8
C3C4C5	+1.9	+3.6
C4C5C6	+1.6	+2.6
C5C6C1	−3.1	−5.7
C6C1C2	+1.4	+3.1
O1C1C2	+0.3	−0.3
O2C2C3	−2.7	−2.4
Dihedrals		
H1O1C1C2	+11.6	+1.2
H2O2C2C3	+5.9	+25.0

Table 6.5: Deviation from the ground state of the most important parameters of catechol in the first excited state compared to the results in the literature. Labels refer to Figure 3.9.

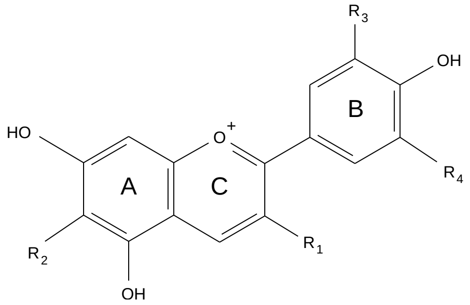

Figure 6.3: Chemical structure of the anthocyanidins studied in this thesis.

Name	R_1	R_2	R_3	R_4
Pelargonidin	OH	H	H	H
Cyanidin	OH	H	OH	H
Delphinidin	OH	H	OH	OH
Aurantinidin	OH	OH	H	H

Table 6.6: Anthocyanidins used in this thesis according to their substitutions.

lar [169]. Here, to reduce the computational cost, all of the calculations have been carried out with the sugar free compounds.

6.6.1 Effect of hydroxylations

In agreement with experiments [170, 171], *ab initio* configuration interaction (CI) calculations have shown that hydroxy substitutions at position R_2 increase the lowest excitation energy in anthocyanidins, while successive hydroxylations at positions R_3 and R_4 decrease it [172].

To assess the performance of ΔSCF, we have studied the lowest excitation energies of the anthocyanidins in Ref. [172] (Table 6.6). The excitations have been modelled by promoting one electron from HOMO to LUMO, as TDDFT calculations have shown that the lowest energy transition in anthocyanidins is essentially HOMO → LUMO [173].

Since we have modelled the anthocyanidins in their protonated form, a uniform background charge is introduced, and the convergence of the energy with respect to the size of the supercell is slow, reflecting the decreasing interaction between the dyes and the jellium background. However, excitation energies

Name	KS	ΔSCF	TDDFT [173]	CI [172]	Exp [170]
Pelargonidin	1.70	1.74	2.55	2.58	2.38
Cyanidin	1.61	1.67	2.46	2.56	2.32
Delphinidin	1.64	1.57	2.50	2.46	2.27
Aurantinidin	1.72	1.86	-	2.63	2.48

Table 6.7: Lowest excitation energies of anthocyanidins compared to the results in the literature.

are given by differences of energies, and in our calculations, they are already converged to within 0.01 eV with respect to the size of the supercell.

Results are presented in Table 6.7, where they are compared with other works in the literature. ΔSCF severely underestimates the experimental values by around 0.5 eV, which could be ascribed to the LDA problem with optical gaps (in TDDFT, hybrid functionals shift the peaks of anthocyanidins by 0.3–0.4 eV with respect to the PBE functional [169,174]). A direct comparison with the experimental data is however not possible, as they were taken with dyes in a methanol solvent. We note that while TDDFT gives energies which are close to the experiments, it fails in reproducing the correct relative order. On the contrary, despite the severe underestimation, ΔSCF follows the before mentioned trend, i.e., a hydroxylation in the A-ring causes a blue-shift in the spectrum, while a red-shift is the consequence of successive hydroxy substitutions in the B-ring.

6.6.2 Effect of pH

The chemical form of anthocyanins is dependent on the pH of the solution (Figure 6.4). At acidic conditions ($\mathrm{pH} < 3$), anthocyanins exist mostly in the protonated flavylium form (AH^+), and present an absorption band at 2.34 eV [175]. In the pH range 3–4, the flavylium coexists with a neutral quinonoidal form (A), whose absorption band is red-shifted to 2.24 eV. Then, up to pH 5 the quinonoidal form is prevalent. At higher pH, an ionised quinonoidal form (A^-) also appears.

We have calculated the ΔSCF excitation energies of cyanidin for AH^+, A,

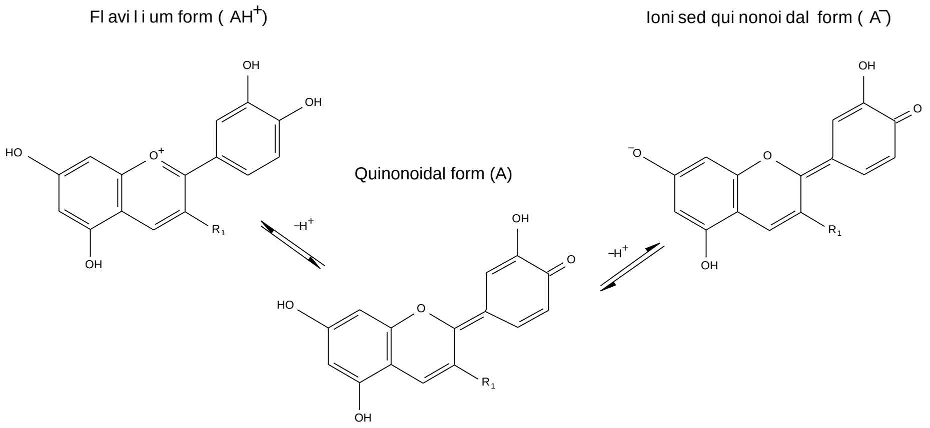

Figure 6.4: Equilibrium between the various forms of anthocyanins depending on the pH of the solution.

	AH^+	A	A^-
KS	1.61	1.49	1.30
ΔSCF	1.67	1.75	1.30
TDDFT [169]	2.14	2.33	2.20
Exp [175]	2.34	2.14	2.10

Table 6.8: Excitation energies of flavylium (AH^+), quinonoidal (A), and ionised quinonoidal (A^-) form of cyanidin. Experimental data refer to the anthocyanin pigment of red cabbage.

and A^- (Table 6.8). Our calculations indicate that, from the neutral form A, a protonation shifts the excitation energies towards the red, in agreement with TDDFT, but at odds with the experiment. Viceversa, an increase of pH red-shifts the spectrum, in agreement with both TDDFT and experiment.

So far, the emerging picture is that LDA-ΔSCF underestimates the excitation energies of anthocyanidins. A study on the singlet states of a set of 16 chromophores has revealed that when hybrid functionals are used, TDDFT and ΔSCF give similar accuracies, whereas with PBE, instead, TDDFT is on average more accurate by around 0.2 eV [162]. As stressed by the authors, however, this is a statistical argument, and one should not expect the same accuracy between TDDFT and ΔSCF for a single class of dyes. Even with hybrid functionals, the two methods can differ also by as much as 0.6 eV [162].

Despite the failure, even with LDA, the underestimation seems to be sys-

Mode	E_{ads} (eV)
MON1	-1.99
MON2	-2.87
BRI	-2.36

Table 6.9: Adsorption energies of the investigated modes of cyanidin on anatase (101). See text for the abbreviations of modes.

tematic. This allows predictions of differences in the excitation energies with an accuracy comparable to TDDFT.

6.6.3 Cyanidin on anatase (101)

Upon adsorption on TiO_2, the equilibrium between the forms is thought to be shifted towards the quinonoidal, since the cyanidin-sensitised TiO_2 appears purple and the spectrum is red-shifted by 0.20 eV compared to cyanidin in solution [48].

To investigate the effect of binding to TiO_2 on the excitation energy, we have adsorbed cyanidin on anatase (101), the most exposed face of nanoparticles in DSSCs.

Ground state structures

In section 3.6, we have employed the anatase (101) surface for the adsorption of catechol, which constitutes the anchoring group of cyanidin. We recall that for catechol both bridging and monodentate bindings are possible, with the equilibrium shifted towards the first. Based on these findings, we have studied two partially dissociative monodentate (MON1 and MON2) and a fully dissociative bridging mode (BRI) (Figure 6.5). MON1 and BRI have a similar spatial arrangement of the dyes, while MON2 differs in their orientation. In MON1 and MON2, rather than positioning the dissociated proton on the surface, we have preferred to remove it and work with a neutral supercell. Consistently, the second dissociated proton of BRI was attached to the surface.

Table 6.9 reports the corresponding adsorption energies. Differently from the adsorption of catechol, MON2 is predicted to be the most stable binding,

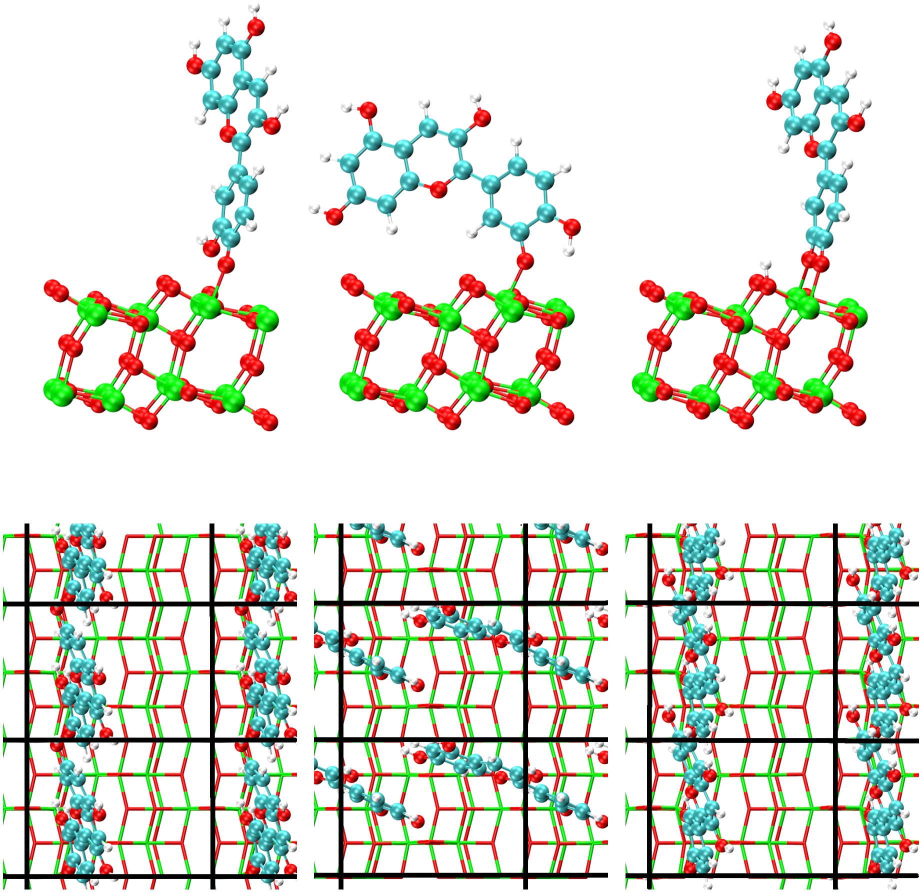

Figure 6.5: Front views (top) of the relaxed geometries of cyanidin on TiO_2 anatase (101) in MON1 (left), MON2 (middle), and BRI (right), with their corresponding views from the top (below). Ti are green, O red, C cyan, H white. The black lines mark the periodic unit cells.

	Free	aMON1	aMON2	aBRI
KS	1.61	1.41 (0.20)	1.10 (0.51)	1.11 (0.50)
ΔSCF	1.67	1.56 (0.11)	1.42 (0.25)	1.34 (0.33)
TDDFT [176]	2.39	-		1.91 (0.48)
Exp [48]	2.30	-		2.10 (0.20)

Table 6.10: Lowest excitation energies (eV) of cyanidin in gas phase and when bound to TiO_2 anatase (101). In parenthesis, the shift between the two values is reported.

followed by BRI. However, when comparing the two structures with the similar spatial arrangement of the dyes, MON1 and BRI, the latter is more favoured by 0.37 eV, following the trend already seen for catechol.

Excitation energies

In Table 6.10, we compare the HOMOdye → LUMOdye excitation energies of cyanidin on anatase with the HOMO → LUMO of the dye in gas phase, and report the shifts caused by the binding. We show also the data from a simple KS analysis and TDDFT [176]. ΔSCF improves the KS results in all of the adsorptions, but the excitations remain far from the experimental values, which are better reproduced by TDDFT. Despite the accuracy on the excitation energies, however, TDDFT overestimates the experimental shift (0.48 vs 0.20 eV), whereas ΔSCF gives more accurate values for all of the adsorptions (0.1–0.3 eV).

Excited state structure of MON2

Finally, we have relaxed the most stable MON2 structure in the excited spin-mixed state by promoting one electron from HOMOdye to LUMOdye within the same spin channel and taking the ΔSCF gradient.

We show in Figure 6.6 the relaxed structure. None of the atoms of the surface displaces by more than 0.01 Å, in line with the fact that the excitation is localised within the dye. The only exception is the Ti1 atom. Its covalent bond length with the dye is increased significantly by 0.06 Å, which suggests that the interaction becomes weaker after the excitation. Another change is due

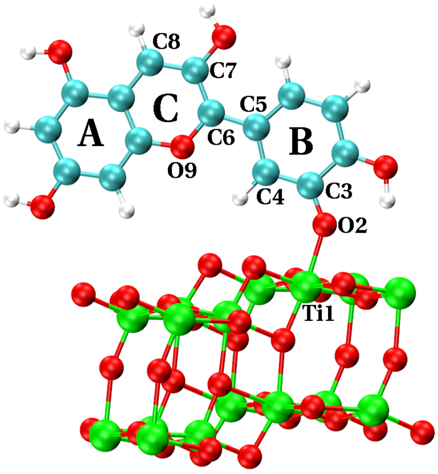

Figure 6.6: Excited state structure of MON2 with the atomic labels used in the text. Ti are green, O red, C cyan, H white. The corresponding ground state structure is shown in Figure 6.5, middle.

Bonds	Deviation (Å)
Ti1O2	+0.06
C3C4	+0.02
C4C5	−0.02
C5C6	+0.02
C6C7	−0.03
C7C8	+0.02
C6O9	+0.02

Table 6.11: Most important changes in the bond lengths of the first excited state of MON2 from the ground state structure. Labels refer to Figure 6.6.

to the larger distance C5C6 between the rings B and C, which increases by 0.02 Å. We have not observed any change larger than 0.01 Å also in the atoms of ring A. The most important deviations in the bond distances of cyanidin from its ground state are summarised in Table 6.11.

6.7 Summary of the chapter

In this chapter, we have illustrated the ΔSCF method, which we have successfully tested on CO and catechol. We have focussed on anthocyanidins. ΔSCF systematically underestimates their excitation energies. Yet, it is interesting that relative excitations between different anthocyanidins follow the experimental trend.

We have found the most stable adsorption of cyanidin on TiO_2 to be monodentate. While HOMOdye → LUMOdye excitations of cyanidin on TiO_2 are not accurate, the red-shifts from the gas phase are in line with experiments.

We have proposed ΔSCF as a simple tool to calculate excited state geometries of dyes. At the affordable computational cost of DFT, we have relaxed the structure corresponding to the most favoured adsorption of cyanidin on TiO_2 in its HOMOdye → LUMOdye excited state.

Chapter 7

Conclusions

We have presented a DFT investigation on some of the current challenges in the mechanism of DSSCs. The entire work was motivated by the search for a new generation of solar cells, more affordable than the traditional silicon devices. DSSCs fulfil this requirement, but they still suffer from low efficiencies.

In a DSSC, many factors can influence the overall conversion efficiency. In this thesis, we have focussed on the interaction dye/semiconductor, the coating of TiO_2 with a second oxide, and the issues behind the ALD of Al_2O_3 on anatase. In addition, we have assessed the validity of ΔSCF to study the excitations of natural anthocyanidins.

7.1 Binding of catechol

Catechol is among the most popular and relevant dyes. We have shown that its adsorption on anatase (101), the most prevalent face in TiO_2 nanoparticles for DSSCs, causes the introduction of molecular states into the band gap of the semiconductor. The lowest unoccupied orbitals are localised only on TiO_2. Thus, the electronic structures for the catechol/TiO_2 system fit into the general understanding of the type II mechanism, which is thought to be direct from the dye to the semiconductor, and not to involve any excited states of the first.

On rutile (110), monodentate and bridging adsorptions coexist, but only the less stable bridging introduces gap states [177]. We have predicted that catechol binds in a monodentate way on rutile (100), as bridging is unstable. This adsorption introduces two dye states into the band gap of rutile. Gap states are beneficial for the photocurrent, as they are involved in the electron transfer of the type II mechanism. Since the photovoltages of rutile and anatase DSSCs are almost the same, whereas rutile films give a lower short-circuit photocurrent [14], increasing the amount of the (100) orientation may improve the charge injection, and hence the efficiency of catechol-based rutile DSSCs.

On the other hand, we have shown that when the more common anatase nanoparticles are employed, all of the investigated adsorptions of catechol and formic acid are stabilised after coating the surface with a thin layer of a-Al_2O_3. In an actual device, this would bring to an increase of the dye coverage, which, again, would positively impact on the photocurrent.

7.2 Key aspects of the Al_2O_3 coating

The findings on catechol parallel a similar stabilisation effect of the a-Al_2O_3 coating on formic acid and the whole N3 dye. The stronger interaction with the substrate supports the experimental finding that the adsorption of N3, and hence the photocurrents, are improved on the Al_2O_3 overcoated TiO_2 [66].

Thus, our results point towards an a-Al_2O_3 overlayer which acts as an enhancer of the dye adsorption. The implication is that a full a-Al_2O_3 coverage of the TiO_2 film is a key ingredient to enhance the efficiency of DSSCs. Unfortunately, if a uniform coating is to be obtained, the island growth mode imposes a lower bound of 5-10 layers to the number of ALD cycles, with a corresponding decrease of efficiency in DSSCs [74].

We have attributed the experimental difficulties of ALD to the poor hydration of the anatase (101) substrate. Lower temperatures could prevent the desorption of water and promote a uniform growth, although at the expenses of slower ALD reaction rates. Alternatively, the reactive sites could be increased by higher water partial pressures. This would lead to a higher waste of water, always supplied in excess during ALD, and would worsen the environmental performance of the ALD technology [178].

Another mechanism postulated in the literature for the coating is the surface dipole effect: the overlayer can induce a shift of the CB edge of TiO_2 towards positive energies (resulting into higher V_{oc}), as a consequence of a dipole moment formed at the oxide/TiO_2 interface. We would like to mention that our calculations have not detected any significant shift of the TiO_2 CB due to the a-Al_2O_3 coating, even though a dipole moment arises in the supercell. A future collaboration will elucidate the origin of this dipole, which could be both due to a charge transfer across the interface or to a charge distribution within the a-Al_2O_3 coating.

7.3 ΔSCF for natural anthocyanidins

We have dedicated part of the research on DSSCs to implement ΔSCF, one of the earliest methods for the calculation of excitation energies, in our DFT code CONQUEST. Motivated by the growing search for cheaper and fully biodegradable dyes, we have employed ΔSCF to reproduce the lowest excitations of natural anthocyanidins. At odds with catechol, ΔSCF is not accurate for vertical excitations of anthocyanidins. Given the large systematic underestimation, it is questionable whether hybrid functionals would give an accuracy comparable to TDDFT, as resulted, on average, from a previous study on singlet energies of organic chromophores [162].

ΔSCF allows a straightforward calculation of the excited state geometries. The relaxation of molecules, both in gas phase or on a surface, is performed at the affordable computational cost of DFT. Yet, the study of the catechol/TiO_2 system in the excited state of catechol was not possible due to a non-convergence of the self-consistent run. We have pointed to the hybridisation of the LU-

MOdye with the continuum of states of the oxide as the cause of the lack of self-consistency. This is confirmed by the fact that the determination of the excited state in the cyanidin/TiO_2 system, where LUMOdye does not mix with TiO_2, has not presented any technical difficulties. One possible way to overcome the problem could be to extend ΔSCF to allow the excited electron to be spread over a linear combinations of KS states [161]. As results on free and Ti-bound catechol suggest the suitability of ΔSCF for this dye, this is an intriguing and worthwhile direction.

Finally, we would like to emphasise that *ab initio* MD simulations in the excited BO state of the dye/TiO_2 system, although never performed in this thesis, are also possible by ΔSCF. Similarly to geometry optimisations, ΔSCF *ab initio* MD does not require any significant modification of the main code.

Bibliography

[1] M. Grätzel. Photoelectrochemical solar cells. *Nature*, 414:338–344, 2001.

[2] A. Hagfeldt, G. Boschloo, L. Sun, L. Kloo, and H. Pettersson. Dye-sensitized solar cells. *Chemical Reviews*, 110(11):6595–6663, 2010.

[3] S.R. Wenham and M.A. Green. Silicon solar cells. *Progress in Photovoltaics: Research and Applications*, 4(1):3–33, 1998.

[4] A.V. Shah, H. Schade, M. Vanecek, J. Meier, E. Vallat-Sauvain, N. Wyrsch, U. Kroll, C. Droz, and J. Bailat. Thin-film silicon solar cell technology. *Progress in Photovoltaics: Research and Applications*, 12(2-3):113–142, 2004.

[5] Q. Zhang and G. Cao. Nanostructured photoelectrodes for dye-sensitized solar cells. *Nano Today*, 6(1):91–109, 2011.

[6] B. O'Regan and M. Grätzel. A low-cost, high-efficiency solar cell based on dye-sensitized colloidal TiO_2 films. *Nature*, 353:737–740, 1991.

[7] H. Gerischer, M.E. Michel-Beyerle, F. Rebentrost, and H. Tributsch. Sensitization of charge injection into semiconductors with large band gap. *Electrochimica Acta*, 13(6):1509–1515, 1968.

[8] R. Eichberger and F. Willig. Ultrafast electron injection from excited dye molecules into semiconductor electrodes. *Chemical Physics*, 141(1):159–173, 1990.

[9] R. Memming. Electron transfer processs with excited molecules at semiconductor electrodes. *Progress in surface science*, 17(1):7–73, 1984.

[10] F. Hao, X. Jiao, J. Li, and H. Lin. Solvent dipole modulation of conduction band edge shift and charge recombination in robust dye-sensitized solar cells. *Nanoscale*, 5(2):726–733, 2013.

[11] P.M. Oliver, G.W. Watson, E.T. Kelsey, and S.C. Parker. Atomistic simulation of the surface structure of the TiO_2 polymorphs rutile and anatase. *Journal of Materials Chemistry*, 7(3):563–568, 1997.

[12] M. Lazzeri, A. Vittadini, and A. Selloni. Structure and energetics of stoichiometric TiO_2 anatase surfaces. *Physical Review B*, 63(15):155409, 2001.

[13] Y. He, O. Dulub, H. Cheng, A. Selloni, and U. Diebold. Evidence for the predominance of subsurface defects on reduced anatase TiO_2 (101). *Physical Review Letters*, 102(10):106105, 2009.

[14] N.G. Park, J. Van de Lagemaat, and A.J. Frank. Comparison of dye-sensitized rutile- and anatase-based TiO_2 solar cells. *Journal of Physical Chemistry B*, 104(38):8989–8994, 2000.

[15] C.L. Pang, R. Lindsay, and G. Thornton. Chemical reactions on rutile TiO_2 (110). *Chemical Society Reviews*, 39(51):00, 2008.

[16] U. Diebold. The surface science of titanium dioxide. *Surface Science Reports*, 48(5-8):53–229, 2003.

[17] G. Teobaldi, W.A. Hofer, O. Bikondoa, C.L. Pang, G. Cabailh, and G. Thornton. Modelling STM images of TiO_2 (110) from first-principles: defects, water adsorption and dissociation products. *Chemical Physics Letters*, 437(1):73–78, 2007.

[18] R. Schaub, P. Thostrup, N. Lopez, E. Lægsgaard, I. Stensgaard, J.K. Nørskov, and F. Besenbacher. Oxygen vacancies as active sites for water dissociation on rutile TiO_2 (110). *Physical Review Letters*, 87(26), 2001.

[19] L.M. Liu, C. Zhang, G. Thornton, and A. Michaelides. Structure and dynamics of liquid water on rutile TiO_2 (110). *Physical Review B*, 82(16):161415, 2010.

[20] S. Wendt, R. Schaub, J. Matthiesen, E.K. Vestergaard, E. Wahlström, M.D. Rasmussen, P. Thostrup, L.M. Molina, E. Lægsgaard, I. Stensgaard, B. Hammer, and F. Besenbacher. Oxygen vacancies on TiO_2 (110) and their interaction with H_2O and O_2: A combined high-resolution STM and DFT study. *Surface Science*, 598(1):226–245, 2005.

[21] P. Jones and J.A. Hockey. Infra-red studies of rutile surfaces. Part 2. Hydroxylation, hydration and structure of rutile surfaces. *Transactions of the Faraday Society*, 67:2679–2685, 1971.

[22] A. Vittadini, A. Selloni, F.P. Rotzinger, and M. Grätzel. Formic acid adsorption on dry and hydrated TiO_2 anatase (101) surfaces by DFT calculations. *The Journal of Physical Chemistry B*, 104(6):1300–1306, 2000.

[23] F. Nunzi and F. De Angelis. DFT investigations of formic acid adsorption on single-wall TiO_2 nanotubes: effect of the surface curvature. *Journal of Physical Chemistry C*, 115(5):2179–2186, 2011.

[24] X.Q. Gong, A. Selloni, M. Batzill, and U. Diebold. Steps on anatase TiO_2 (101). *Nature Materials*, 5(8):665–670, 2006.

[25] K.L. Miller, J.L. Falconer, and J.W. Medlin. Effect of water on the adsorbed structure of formic acid on TiO_2 anatase (101). *Journal of Catalysis*, 278(2):321–328, 2011.

[26] G.Y. Popova, T.V. Andrushkevich, Y.A. Chesalov, and E.S. Stoyanov. In situ FTIR study of the adsorption of formaldehyde, formic acid, and methyl formiate at the surface of TiO_2 (Anatase). *Kinetics and Catalysis*, 41(6):805–811, 2000.

[27] P. Raghunath and M.C. Lin. Adsorption configurations and reactions of boric acid on a TiO_2 anatase (101) surface. *The Journal of Physical Chemistry C*, 112(22):8276–8287, 2008.

[28] E. Mosconi, A. Selloni, and F. De Angelis. Solvent effects on the adsorption geometry and electronic structure of dye-sensitized TiO_2: a first-principles investigation. *The Journal of Physical Chemistry C*, 116(9):5932–5940, 2012.

[29] F. De Angelis, S. Fantacci, and R. Gebauer. Simulating dye-sensitized TiO_2 heterointerfaces in explicit solvent: absorption spectra, energy levels, and dye desorption. *The Journal of Physical Chemistry Letters*, 2(7):813–817, 2011.

[30] S.G. Abuabara, Luis G.C. Rego, and V.S. Batista. Influence of thermal fluctuations on interfacial electron transfer in functionalized TiO_2 semiconductors. *Journal of the American Chemical Society*, 127(51):18234–18242, 2005.

[31] W.R. Duncan and O.V. Prezhdo. Electronic structure and spectra of catechol and alizarin in the gas phase and attached to titanium. *The Journal of Physical Chemistry B*, 109(1):365–73, 2005.

[32] I. Kondov, H. Wang, and M. Thoss. Computational study of titanium (IV) complexes with organic chromophores. *International Journal of Quantum Chemistry*, 106(6):0, 2006.

[33] P.C. Redfern, P. Zapol, L.A. Curtiss, T. Rajh, and M.C. Thurnauer. Computational studies of catechol and water interactions with titanium

oxide nanoparticles. *The Journal of Physical Chemistry B*, 107(41):11419–11427, 2003.

[34] L.G.C. Rego and V.S. Batista. Quantum dynamics simulations of interfacial electron transfer in sensitized TiO_2 semiconductors. *Journal of the American Chemical Society*, 125(26):7989–7997, 2003.

[35] T. Lana-Villarreal, A. Rodes, J.M. Perez, and R. Gomez. A spectroscopic and electrochemical approach to the study of the interactions and photoinduced electron transfer between catechol and anatase nanoparticles in aqueous solution. *Journal of the American Chemical Society*, 127(36):12601–12611, 2005.

[36] Y. Wang, K. Hang, N.A. Anderson, and T. Lian. Comparison of electron transfer dynamics in molecule-to-nanoparticle and intramolecular charge transfer complexes. *The Journal of Physical Chemistry B*, 107(35):9434–9440, 2003.

[37] S. Koppen and W. Langel. Adsorption of small organic molecules on anatase and rutile surfaces: a theoretical study. *Physical Chemistry Chemical Physics*, 10(14):1907–1915, 2008.

[38] W. Stier and O.V. Prezhdo. Non-adiabatic molecular dynamics simulation of ultrafast solar cell electron transfer. *Journal of Molecular Structure: THEOCHEM*, 630(1-3):33–43, 2003.

[39] C.R. Rice, M.D. Ward, M.K. Nazeeruddin, and M. Grätzel. Catechol as an efficient anchoring group for attachment of ruthenium–polypyridine photosensitisers to solar cells based on nanocrystalline TiO_2 films. *New Journal of Chemistry*, 24(9):651–652, 2000.

[40] M.K. Nazeeruddin, A. Kay, I. Rodicio, R. Humphry-Baker, E. Müller, P. Liska, N. Vlachopoulos, and M. Grätzel. Conversion of light to electricity by *cis*-X_2Bis(2, 2'-bipyridyl-4, 4'-dicarboxylate)ruthenium(II) charge-

transfer sensitizers (X= Cl^-, Br^-, I^-, CN^-, and SCN^-) on nanocrystalline titanium dioxide Electrodes. *Journal of the American Chemical Society*, 115(14):6382–6390, 1993.

[41] M.K. Nazeeruddin, P. Pechy, T. Renouard, S.M. Zakeeruddin, R. Humphry-Baker, P. Comte, P. Liska, L. Cevey, E. Costa, V. Shklover, L. Spiccia, G.B. Deacon, C.A. Bignozzi, and M. Grätzel. Engineering of efficient panchromatic sensitizers for nanocrystalline TiO_2-based solar cells. *Journal of the American Chemical Society*, 123(8):1613–1624, 2001.

[42] L. Han, A. Islam, H. Chen, C. Malapaka, B. Chiranjeevi, S. Zhang, X. Yang, and M. Yanagida. High-efficiency dye-sensitized solar cell with a novel co-adsorbent. *Energy & Environmental Science*, 5(3):6057–6060, 2012.

[43] T. Bessho, S.M. Zakeeruddin, C.Y. Yeh, E.W.G. Diau, and M. Grätzel. Highly efficient mesoscopic dye-sensitized solar cells based on donor–acceptor-substituted porphyrins. *Angewandte Chemie International Edition*, 49(37):6646–6649, 2010.

[44] G. Calogero, J.H. Yum, A. Sinopoli, G. Di Marco, M. Grätzel, and M.K. Nazeeruddin. Anthocyanins and betalains as light-harvesting pigments for dye-sensitized solar cells. *Solar Energy*, 86(5):1563–1575, 2012.

[45] S. Hao, J. Wu, Y. Huang, and J. Lin. Natural dyes as photosensitizers for dye-sensitized solar cell. *Solar Energy*, 80(2):209–214, 2006.

[46] G. Calogero and G.D. Marco. Red Sicilian orange and purple eggplant fruits as natural sensitizers for dye-sensitized solar cells. *Solar Energy Materials and Solar Cells*, 92(11):1341–1346, 2008.

[47] Q. Dai and J. Rabani. Photosensitization of nanocrystalline TiO_2 films by anthocyanin dyes. *Journal of Photochemistry and Photobiology A: Chemistry*, 148(1):17–24, 2002.

[48] K. Tennakone, A.R. Kumarasinghe, G. Kumara, K.G.U. Wijayantha, and P.M. Sirimanne. Nanoporous TiO_2 photoanode sensitized with the flower pigment cyanidin. *Journal of Photochemistry and Photobiology A: Chemistry*, 108(2):193–195, 1997.

[49] N.J. Cherepy, G.P. Smestad, M. Grätzel, and J.Z. Zhang. Ultrafast electron injection: implications for a photoelectrochemical cell utilizing an anthocyanin dye-sensitized TiO_2 nanocrystalline electrode. *The Journal of Physical Chemistry B*, 101(45):9342–9351, 1997.

[50] M. Grätzel. Recent advances in sensitized mesoscopic solar cells. *Accounts of Chemical Research*, 42(11):1788–1798, 2009.

[51] H. Nusbaumer, J.E. Moser, S.M. Zakeeruddin, M.K. Nazeeruddin, and M. Grätzel. Co-II(dbbiP)(2)(2^+) complex rivals tri-iodide/iodide redox mediator in dye-sensitized photovoltaic cells. *The Journal of Physical Chemistry B*, 105(43):10461–10464, 2001.

[52] M. Brugnati, S. Caramori, S. Cazzanti, L. Marchini, and C.A. Bignozzi. Electron transfer mediators for photoelectrochemical cells based on Cu(I) metal complexes. *International Journal of Photoenergy*, 2007, 2007.

[53] Z. Zhang, P. Chen, T.N. Murakami, S.M. Zakeeruddin, and M. Grätzel. The 2,2,6,6-tetramethyl-1-piperidinyloxy radical: an efficient, iodine-free redox mediator for dye-sensitized solar cells. *Advanced Functional Materials*, 18(2):341–346, 2008.

[54] E. Palomares, J.N. Clifford, S.A. Haque, T. Lutz, and J.R. Durrant. Slow charge recombination in dye-sensitised solar cells (DSSC) using Al_2O_3 coated nanoporous TiO_2 films. *Chemical Communications*, (14):1464–1465, 2002.

[55] E. Palomares, J.N. Clifford, T. Haque, S.A.and Lutz, and J.R. Durrant. Control of charge recombination dynamics in dye sensitized solar cells by

the use of conformally deposited metal oxide blocking layers. *Journal of the American Chemical Society*, 125(2):475–482, 2003.

[56] X.T. Zhang, H.W. Liu, T. Taguchi, Q.B. Meng, O. Sato, and A. Fujishima. Slow interfacial charge recombination in solid-state dye-sensitized solar cell using Al_2O_3-coated nanoporous TiO_2 films. *Solar Energy Materials and Solar Cells*, 81(2):197–203, 2004.

[57] M. Shanmugam, M.F. Baroughi, and D. Galipeau. Effect of atomic layer deposited ultra thin HfO_2 and Al_2O_3 interfacial layers on the performance of dye sensitized solar cells. *Thin Solid Films*, 518(10):2678–2682, 2010.

[58] A. Zaban, S.G. Chen, S. Chappel, and B.A. Gregg. Bilayer nanoporous electrodes for dye sensitized solar cells. *Chemical Communications*, 2000(22):2231–2232, 2000.

[59] J. Xia, N. Masaki, K. Jiang, and S. Yanagida. Sputtered Nb_2O_5 as a novel blocking layer at conducting glass/TiO_2 interfaces in dye-sensitized ionic liquid solar cells. *The Journal of Physical Chemistry C*, 111(22):8092–8097, 2007.

[60] S. Wu, H. Han, Q. Tai, J. Zhang, B.L. Chen, S. Xu, C. Zhou, Y. Yang, H. Hu, and X.Z. Zhao. Improvement in dye-sensitized solar cells with a ZnO-coated TiO_2 electrode by rf magnetron sputtering. *Applied Physics Letters*, 92(12):122106, 2008.

[61] Z.S. Wang, M. Yanagida, K. Sayama, and H. Sugihara. Electronic-insulating coating of $CaCO_3$ on TiO_2 electrode in dye-sensitized solar cells: improvement of electron lifetime and efficiency. *Chemistry of Materials*, 18(12):2912–2916, 2006.

[62] D.B. Menzies, R. Cervini, Y.B. Cheng, G.P. Simon, and L. Spiccia. Nanostructured ZrO_2-coated TiO_2 electrodes for dye-sensitised solar cells. *Journal of Sol-Gel Science and Technology*, 32(1):363–366, 2004.

[63] Y. Diamant, S. Chappel, SG Chen, O. Melamed, and A. Zaban. Core-shell nanoporous electrode for dye sensitized solar cells: the effect of shell characteristics on the electronic properties of the electrode. *Coordination Chemistry Reviews*, 248(13-14):1271–1276, 2004.

[64] F. Fabregat-Santiago, J. García-Cañadas, E. Palomares, J.N. Clifford, S.A. Haque, J.R. Durrant, G. Garcia-Belmonte, and J. Bisquert. The origin of slow electron recombination processes in dye-sensitized solar cells with alumina barrier coatings. *Journal of Applied Physics*, 96(11):6903–6907, 2004.

[65] A. Kay and M. Grätzel. Dye-sensitized core-shell nanocrystals: improved efficiency of mesoporous tin oxide electrodes coated with a thin layer of an insulating oxide. *Chemistry of Materials*, 14(7):2930–2935, 2002.

[66] V. Ganapathy, B. Karunagaran, and S.W. Rhee. Improved performance of dye-sensitized solar cells with TiO_2/alumina core-shell formation using atomic layer deposition. *Journal of Power Sources*, 195(15):5138–5143, 2010.

[67] I. Ichinose, H. Senzu, and T. Kunitake. A surface sol-gel process of TiO_2 and other metal oxide films with molecular precision. *Chemistry of Materials*, 9(6):1296–1298, 1997.

[68] S.M. George. Atomic layer deposition: an overview. *Chemical Reviews*, 110(1):111–131, 2010.

[69] A.C. Dillon, A.W. Ott, J.D. Way, and S.M. George. Surface chemistry of Al_2O_3 deposition using $Al(CH_3)_3$ and H_2O in a binary reaction sequence. *Surface Science*, 322(1-3):230–242, 1995.

[70] S.D. Elliott and J.C. Greer. Simulating the atomic layer deposition of alumina from first principles. *Journal of Materials Chemistry*, 14(21):3246–3250, 2004.

[71] S.D. Elliott and H.P. Pinto. Modelling the deposition of high-k dielectric films by first principles. *Journal of Electroceramics*, 13(1):117–120, 2004.

[72] A. Rahtu, T. Alaranta, and M. Ritala. In situ quartz crystal microbalance and quadrupole mass spectrometry studies of atomic layer deposition of aluminum oxide from trimethylaluminum and water. *Langmuir*, 17(21):6506–6509, 2001.

[73] Z. Hu, J. Shi, and H. Turner. Molecular dynamics simulation of the Al_2O_3 film structure during atomic layer deposition. *Molecular Simulation*, 35(4):270–279, 2009.

[74] C. Lin, F.Y. Tsai, M.H. Lee, C.H. Lee, T.C. Tien, L.P. Wang, and S.Y. Tsai. Enhanced performance of dye-sensitized solar cells by an Al_2O_3 charge-recombination barrier formed by low-temperature atomic layer deposition. *Journal of Materials Chemistry*, 14:2999–3003, 2009.

[75] R.L. Puurunen and W. Vandervorst. Island growth as a growth mode in atomic layer deposition: a phenomenological model. *Journal of Applied Physics*, 96:7686, 2004.

[76] O. Gunnarsson and B.I. Lundqvist. Exchange and correlation in atoms, molecules, and solids by the spin-density-functional formalism. *Physical Review B*, 13(10):4274, 1976.

[77] R.O. Jones and O. Gunnarsson. The density functional formalism, its applications and prospects. *Reviews of Modern Physics*, 61(3):689, 1989.

[78] D.R. Bowler, T. Miyazaki, and M.J. Gillan. Recent progress in linear scaling ab initio electronic structure techniques. *Journal of Physics: Condensed Matter*, 14(11):2781, 2002.

[79] D.R. Bowler, R. Choudhury, M.J. Gillan, and T. Miyazaki. Recent progress with large-scale ab initio calculations: the CONQUEST code. *Physica Status Solidi (b)*, 243(5):989–1000, 2006.

[80] T. Miyazaki, D.R. Bowler, R. Choudhury, and M.J. Gillan. Atomic force algorithms in density functional theory electronic-structure techniques based on local orbitals. *The Journal of Chemical Physics*, 121:6186, 2004.

[81] D.R. Hartree. The wave mechanics of an atom with a non-Coulomb central field. Part I. Theory and methods. In *Mathematical Proceedings of the Cambridge Philosophical Society*, volume 24, pages 89–110. Cambridge Univ Press, 1928.

[82] V. Fock. Näherungsmethode zur Lösung des quantenmechanischen Mehrkörperproblems. *Zeitschrift für Physik A Hadrons and Nuclei*, 61(1):126–148, 1930.

[83] R.M. Martin. *Electronic Structure: Basic Theory and Practical Methods.* Cambridge University Press, 2004.

[84] P. Hohenberg and W. Kohn. Inhomogeneous electron gas. *Physical Review*, 136(3B):B864–B871, 1964.

[85] W. Kohn and L.J. Sham. Self-consistent equations including exchange and correlation effects. *Physical Review*, 140(4A):A1133–A1138, 1965.

[86] P. Pulay. Convergence acceleration of iterative sequences. The case of SCF iteration. *Chemical Physics Letters*, 73(2):393–398, 1980.

[87] D.M. Ceperley and B.J. Alder. Ground state of the electron gas by a stochastic method. *Physical Review Letters*, 45(7):566–569, 1980.

[88] J.P. Perdew, K. Burke, and M. Ernzerhof. Generalized gradient approximation made simple. *Physical Review Letters*, 77(18):3865–3868, 1996.

[89] J.P. Perdew and Y. Wang. Accurate and simple analytic representation of the electron-gas correlation energy. *Physical Review B*, 45(23):13244–13249, 1992.

[90] A.D. Becke. Density-functional exchange-energy approximation with correct asymptotic behavior. *Physical Review A*, 38(6):3098–3100, 1988.

[91] K. Kim and K.D. Jordan. Comparison of density functional and MP2 calculations on the water monomer and dimer. *The Journal of Physical Chemistry*, 98(40):10089–10094, 1994.

[92] P.J. Stephens, F.J. Devlin, C.F. Chabalowski, and M.J. Frisch. Ab initio calculation of vibrational absorption and circular dichroism spectra using density functional force fields. *The Journal of Physical Chemistry*, 98(45):11623–11627, 1994.

[93] C. Lee, W. Yang, and R.G. Parr. Development of the Colle-Salvetti correlation-energy formula into a functional of the electron density. *Physical Review B*, 37(2):785, 1988.

[94] A.D. Becke. A new mixing of Hartree–Fock and local density-functional theories. *The Journal of Chemical Physics*, 98:1372, 1993.

[95] P. Pulay. Ab initio calculation of force constants and equilibrium geometries in polyatomic molecules. *Molecular Physics*, 17(2):197–204, 1969.

[96] H.J. Monkhorst and J.D. Pack. Special points for Brillouin-zone integrations. *Physical Review B*, 13(12):5188–5192, 1976.

[97] G. Kresse and J. Hafner. Ab initio molecular dynamics for liquid metals. *Physical Review B*, 47(1):558–561, 1993.

[98] G. Kresse and J. Furthmuller. Efficiency of ab-initio total energy calculations for metals and semiconductors using a plane-wave basis set. *Computational Materials Science*, 6(1):15–50, 1996.

[99] J. Junquera, Ó. Paz, D. Sánchez-Portal, and E. Artacho. Numerical atomic orbitals for linear-scaling calculations. *Physical Review B*, 64(23):235111, 2001.

[100] D.R. Hamann, M. Schlüter, and C. Chiang. Norm-conserving pseudopotentials. *Physical Review Letters*, 43(20):1494–1497, 1979.

[101] D. Vanderbilt. Soft self-consistent pseudopotentials in a generalized eigenvalue formalism. *Physical Review B*, 41(11):7892–7895, 1990.

[102] A. Imanishi, H. Suzuki, N. Ohashi, T. Ohta, and Y. Nakato. Dye-sensitized photocurrents and adsorption properties of merocyanine dye at atomically flat rutile (110) and (100) TiO_2 surfaces. *Inorganica Chimica Acta*, 361(3):778–782, 2008.

[103] Y. Lu, D. Choi, J. Nelson, O.B. Yang, and BA Parkinson. Adsorption, desorption, and sensitization of low-index anatase and rutile surfaces by the ruthenium complex dye N3. *Journal of The Electrochemical Society*, 153(8):E131–E137, 2006.

[104] J. Moser, S. Punchihewa, P.P. Infelta, and M. Grätzel. Surface complexation of colloidal semiconductors strongly enhances interfacial electron-transfer rates. *Langmuir*, 7(12):3012–3018, 1991.

[105] O.V. Prezhdo, W.R. Duncan, and V.V. Prezhdo. Photoinduced electron dynamics at the chromophore–semiconductor interface: a time-domain ab initio perspective. *Progress in Surface Science*, 84(1-2):30–68, 2009.

[106] P. Persson, R. Bergstrom, and S. Lunell. Quantum chemical study of photoinjection processes in dye-sensitized TiO_2 nanoparticles. *Journal of Physical Chemistry B*, 104(44):10348–10351, 2000.

[107] R. Sánchez-de Armas, M.A. San-Miguel, J. Oviedo, A. Márquez, and J.F. Sanz. Electronic structure and optical spectra of catechol on TiO_2 nanoparticles from real time TD-DFT simulations. *Physical Chemistry Chemical Physics*, 13(4):1506–1514, 2011.

[108] W. Humphrey, A. Dalke, and K. Schulten. VMD: visual molecular dynamics. *Journal of Molecular Graphics*, 14(1):33–38, 1996.

[109] J.K. Burdett, T. Hughbanks, G.J. Miller, J.W. Richardson Jr, and J.V. Smith. Structural-electronic relationships in inorganic solids: powder neu-

tron diffraction studies of the rutile and anatase polymorphs of titanium dioxide at 15 and 295 K. *Journal of the American Chemical Society*, 109(12):3639–3646, 1987.

[110] U. Terranova and D.R. Bowler. Adsorption of catechol on TiO_2 rutile (100): a density functional theory investigation. *The Journal of Physical Chemistry C*, 114(14):6491–6495, 2010.

[111] S.C. Abrahams and J.L. Bernstein. Rutile: normal probability plot analysis and accurate measurement of crystal structure. *The Journal of Chemical Physics*, 55(7):3206–3211, 1971.

[112] K.V.K. Rao, S.V.N. Naidu, and L. Iyengar. Thermal expansion of rutile and anatase. *Journal of the American Ceramic Society*, 53(3):124–126, 1970.

[113] J. Muscat, N.M. Harrison, and G. Thornton. Effects of exchange, correlation, and numerical approximations on the computed properties of the rutile TiO_2 (100) surface. *Physical Review B*, 59(3):2320–2326, 1999.

[114] F. Labat, P. Baranek, and C. Adamo. Structural and electronic properties of selected rutile and anatase TiO_2 surfaces: an ab initio investigation. *Journal of Chemical Theory and Computation*, 4(2):341–352, 2008.

[115] M. Ramamoorthy, R.D. King-Smith, and D. Vanderbilt. Defects on TiO_2 (110) surfaces. *Physical Review B*, 49(11):7709–7715, 1994.

[116] P.J.D. Lindan, N.M. Harrison, J.M. Holender, M.J. Gillan, and M.C. Payne. The $TiO_2(100)(1 \times 3)$ reconstruction: insights from ab initio calculations. *Surface Science*, 364(3):431–438, 1996.

[117] H. Perron, C. Domain, J. Roques, R. Drot, E. Simoni, and H. Catalette. Optimisation of accurate rutile TiO_2 (110),(100),(101) and (001) surface models from periodic DFT calculations. *Theoretical Chemistry Accounts*, 117(4):565–574, 2007.

[118] J.P. Cornard, C. Lapouge, and C. Allet-Bodelot. Study of S_0 and S_1 states of catechol and catechol-Al(III) systems in aqueous solution by TD-DFT methods and electronic spectroscopies. *Chemical Physics Letters*, 489(4-6):164–168, 2010.

[119] S.C. Li, J. Wang, P. Jacobson, X.Q. Gong, A. Selloni, and U. Diebold. Correlation between bonding geometry and band gap states at organic-inorganic interfaces: catechol on rutile TiO_2 (110). *Journal of the American Chemical Society*, 131(3):980–984, 2009.

[120] A. Seidl, A. Görling, P. Vogl, J.A. Majewski, and M. Levy. Generalized Kohn-Sham schemes and the band-gap problem. *Physical Review B*, 53(7):3764, 1996.

[121] B.C. O'Regan, S. Scully, A.C. Mayer, E. Palomares, and J. Durrant. The effect of Al_2O_3 barrier layers in TiO_2/Dye/CuSCN photovoltaic cells explored by recombination and DOS characterization using transient photovoltage measurements. *The Journal of Physical Chemistry B*, 109(10):4616–4623, 2005.

[122] M. Liehr, P.A. Thiry, J.J. Pireaux, and R. Caudano. Formic acid on aluminum oxide: A comparison between inelastic-electron-tunneling spectroscopy and high-resolution electron-energy-loss spectroscopy. *Physical Review B*, 31(1):42, 1985.

[123] S.R. Tong, L.Y. Wu, M.F. Ge, W.G. Wang, and Z.F. Pu. Heterogeneous chemistry of monocarboxylic acids on α-Al_2O_3 at ambient condition. *Atmospheric Chemistry and Physics Discussions*, 10:3937–3974, 2010.

[124] X. Zhao, D. Ceresoli, and D. Vanderbilt. Structural, electronic, and dielectric properties of amorphous ZrO_2 from ab initio molecular dynamics. *Physical Review B*, 71(8):085107, 2005.

[125] L.G. Hector Jr, S.M. Opalka, G.A. Nitowski, L. Wieserman, D.J. Siegel, H. Yu, and J.B. Adams. Investigation of vinyl phosphonic

acid/hydroxylated α-Al_2O_3 (0001) reaction enthalpies. *Surface Science*, 494(1):1–20, 2001.

[126] M. Lucht, M. Lerche, H.C. Wille, Y.V. Shvyd'ko, H.D. Ruter, E. Gerdau, and P. Becker. Precise measurement of the lattice parameters of α-Al_2O_3 in the temperature range 4.5-250 K using the Mossbauer wavelength standard. *Journal of applied crystallography*, 36(4):1075–1081, 2003.

[127] A. Marmier, A. Lozovoi, and M.W. Finnis. The α-alumina (0001) surface: relaxations and dynamics from shell model and density functional theory. *Journal of the European Ceramic Society*, 23(15):2729–2735, 2003.

[128] G. Gutiérrez and B. Johansson. Molecular dynamics study of structural properties of amorphous Al_2O_3. *Physical Review B*, 65(10):104202, 2002.

[129] U. Terranova and D.R. Bowler. Coating TiO_2 anatase by amorphous Al_2O_3: effects on dyes anchoring through carboxyl groups. *The Journal of Physical Chemistry C*, 116(7):4408–4415, 2012.

[130] H. Momida, T. Hamada, Y. Takagi, T. Yamamoto, T. Uda, and T. Ohno. Theoretical study on dielectric response of amorphous alumina. *Physical Review B*, 73(5):054108, 2006.

[131] E.A. Chagarov and A.C. Kummel. Ab initio molecular dynamics simulations of properties of a-Al_2O_3/vacuum and a-ZrO_2/vacuum vs a-Al_2O_3/Ge(100)(2×1) and a-ZrO_2/Ge(100)(2×1) interfaces. *The Journal of Chemical Physics*, 130:124717, 2009.

[132] P. Lamparter and R. Kniep. Structure of amorphous Al_2O_3. *Physica B: Condensed Matter*, 234:405–406, 1997.

[133] C.C. Battaile, D.J. Srolovitz, and J.E. Butler. A kinetic Monte Carlo method for the atomic-scale simulation of chemical vapor deposition: application to diamond. *Journal of Applied Physics*, 82(12):6293–6300, 1997.

[134] P.W. Peacock and J. Robertson. Structure, bonding, and band offsets of (100) $SrTiO_3$–silicon interfaces. *Applied Physics Letters*, 83(26):5497–5499, 2003.

[135] Y.F. Dong, Y.P. Feng, S.J. Wang, and A.C.H. Huan. First-principles study of ZrO_2/Si interfaces: energetics and band offsets. *Physical Review B*, 72(4):045327, 2005.

[136] D. Zhao, C. Chen, Y. Wang, W. Ma, J. Zhao, T. Rajh, and L. Zang. Enhanced photocatalytic degradation of dye pollutants under visible irradiation on Al(III)-modified TiO_2: structure, interaction, and interfacial electron transfer. *Environmental Science & Technology*, 42(1):308–314, 2008.

[137] G.B. Deacon and R.J. Phillips. Relationships between the carbon-oxygen stretching frequencies of carboxylato complexes and the type of carboxylate coordination. *Coordination Chemistry Reviews*, 33(3):227–250, 1980.

[138] J.P.M. Maas. The far infrared absorption spectrum and the assignment of the lattice modes of sodium formate. *Spectrochimica Acta Part A: Molecular Spectroscopy*, 33(8):761–765, 1977.

[139] F. Schiffmann, J. VandeVondele, J. Hutter, R. Wirz, A. Urakawa, and A. Baiker. Protonation-dependent binding of ruthenium bipyridyl complexes to the anatase (101) surface. *The Journal of Physical Chemistry C*, 114(18):8398–8404, 2010.

[140] T.C. Tien, F.M. Pan, L.P. Wang, C.H. Lee, Y.L. Tung, S.Y. Tsai, C. Lin, F.Y. Tsai, and S.J. Chen. Interfacial energy levels and related properties of atomic-layer-deposited Al_2O_3 films on nanoporous TiO_2 electrodes of dye-sensitized solar cells. *Nanotechnology*, 20:305201, 2009.

[141] T.C. Tien, F.M. Pan, L.P. Wang, F.Y. Tsai, and C. Lin. Coverage analysis for the core/shell electrode of dye-sensitized solar cells. *The Journal of Physical Chemistry C*, 114(21):10048–10053, 2010.

[142] H. Cheng and A. Selloni. Surface and subsurface oxygen vacancies in anatase TiO_2 and differences with rutile. *Physical Review B*, 79(9):92101, 2009.

[143] U. Aschauer, Y. He, H. Cheng, S.C. Li, U. Diebold, and A. Selloni. Influence of subsurface defects on the surface reactivity of TiO_2: water on anatase (101). *The Journal of Physical Chemistry C*, 114(2):1278–1284, 2010.

[144] W. Hebenstreit, N. Ruzycki, G.S. Herman, Y. Gao, and U. Diebold. Scanning tunneling microscopy investigation of the TiO_2 anatase (101) surface. *Physical Review B*, 62(24):16334–16336, 2000.

[145] K. Reuter and M. Scheffler. Composition, structure, and stability of RuO_2 (110) as a function of oxygen pressure. *Physical Review B*, 65(3):35406, 2001.

[146] J. Rogal, K. Reuter, and M. Scheffler. CO oxidation at Pd (100): A first-principles constrained thermodynamics study. *Physical Review B*, 75(20):205433, 2007.

[147] D.R. Lide Ed. *CRC Handbook of chemistry and physics.* CRC Press, 2003.

[148] C. Arrouvel, M. Digne, M. Breysse, H. Toulhoat, and P. Raybaud. Effects of morphology on surface hydroxyl concentration: a DFT comparison of anatase-TiO_2 and γ-alumina catalytic supports. *Journal of Catalysis*, 222(1):152–166, 2004.

[149] G.S. Herman, Z. Dohnalek, N. Ruzycki, and U. Diebold. Experimental investigation of the interaction of water and methanol with anatase-TiO_2 (101). *The Journal of Physical Chemistry B*, 107(12):2788–2795, 2003.

[150] A. Vittadini, A. Selloni, F.P. Rotzinger, and M. Grätzel. Structure and energetics of water adsorbed at TiO_2 anatase (101) and (001) surfaces. *Physical Review Letters*, 81(14):2954–2957, 1998.

[151] U. Terranova and D.R. Bowler. Effect of hydration of the TiO_2 anatase (101) substrate on the atomic layer deposition of alumina films. *Journal of Materials Chemistry*, 21(12):4197–4203, 2011.

[152] L.J. Antila, M.J. Heikkilä, V. Aumanen, M. Kemell, P. Myllyperkiö, M. Leskela, and J.E.I. Korppi-Tommola. Suppression of forward electron injection from $Ru(dcbpy)_2(NCS)_2$ to nanocrystalline TiO_2 film as a result of an interfacial Al_2O_3 barrier layer prepared with atomic layer deposition. *The Journal of Physical Chemistry Letters*, 1(2):536–539, 2009.

[153] D. Jacquemin, V. Wathelet, E.A. Perpete, and C. Adamo. Extensive TD-DFT benchmark: singlet-excited states of organic molecules. *Journal of Chemical Theory and Computation*, 5(9):2420, 2009.

[154] D. Guillaumont and S. Nakamura. Calculation of the absorption wavelength of dyes using time-dependent density-functional theory (TD-DFT). *Dyes and Pigments*, 46(2):85–92, 2000.

[155] A. Dreuw and M. Head-Gordon. Failure of time-dependent density functional theory for long-range charge-transfer excited states: The zincbacteriochlorin-bacteriochlorin and bacteriochlorophyll-spheroidene complexes. *Journal of the American Chemical Society*, 126(12):4007–4016, 2004.

[156] P.H. Dederichs, S. Blügel, R. Zeller, and H. Akai. Ground states of constrained systems: Application to cerium impurities. *Physical review letters*, 53(26):2512–2515, 1984.

[157] Q. Wu and T. Van Voorhis. Constrained density functional theory and its application in long-range electron transfer. *Journal of Chemical Theory and Computation*, 2(3):765–774, 2006.

[158] A.M.P. Sena, T. Miyazaki, and D.R. Bowler. Linear scaling constrained density functional theory in CONQUEST. *Journal of Chemical Theory and Computation*, 7(4):884–889, 2011.

[159] H. Oberhofer and J. Blumberger. Charge constrained density functional molecular dynamics for simulation of condensed phase electron transfer reactions. *The Journal of Chemical Physics*, 131:064101, 2009.

[160] A. Hellman, B. Razaznejad, and B.I. Lundqvist. Potential-energy surfaces for excited states in extended systems. *The Journal of Chemical Physics*, 120(10):4593–4602, 2004.

[161] J. Gavnholt, T. Olsen, M. Engelund, and J. Schiøtz. Δ self-consistent field method to obtain potential energy surfaces of excited molecules on surfaces. *Physical Review B*, 78(7):075441, 2008.

[162] T. Kowalczyk, S.R. Yost, and T.V. Voorhis. Assessment of the ΔSCF density functional theory approach for electronic excitations in organic dyes. *The Journal of Chemical Physics*, 134(5):054128–054128, 2011.

[163] R.J. Maurer and K. Reuter. Assessing computationally efficient isomerization dynamics: ΔSCF density-functional theory study of azobenzene molecular switching. *The Journal of Chemical Physics*, 135:224303, 2011.

[164] T. Ziegler, A. Rauk, and E.J. Baerends. On the calculation of multiplet energies by the Hartree-Fock-Slater method. *Theoretica Chimica Acta*, 43(3):261–271, 1977.

[165] N. Troullier and J.L. Martins. Efficient pseudopotentials for plane-wave calculations. *Physical Review B*, 43(3):1993–2006, 1991.

[166] T. Grabo, M. Petersilka, and E.K.U. Gross. Molecular excitation energies from time-dependent density functional theory. *Journal of Molecular Structure: THEOCHEM*, 501:353–367, 2000.

[167] D. Marshall. Computational studies of CO and CO^+: Density functional theory and time-dependent density functional theory. *Journal of Quantitative Spectroscopy and Radiative Transfer*, 109(15):2546–2560, 2008.

[168] E.S. Nielsen, P. Jørgensen, and J. Oddershede. Transition moments and dynamic polarizabilities in a second order polarization propagator approach. *The Journal of Chemical Physics*, 73:6238, 1980.

[169] A. Calzolari, D. Varsano, A. Ruini, A. Catellani, R. Tel-Vered, H.B. Yildiz, O. Ovits, and I. Willner. Optoelectronic properties of natural cyanin dyes. *The Journal of Physical Chemistry A*, 113(30):8801–8810, 2009.

[170] J.B. Harborne. Spectral methods of characterizing anthocyanins. *Biochemical Journal*, 70(1):22, 1958.

[171] L. Jurd and J.B. Harborne. The structure of aurantinidin. *Phytochemistry*, 7(7):1209–1211, 1968.

[172] K. Sakata, N. Saito, and T. Honda. Ab initio study of molecular structures and excited states in anthocyanidins. *Tetrahedron*, 62(15):3721–3731, 2006.

[173] E.L.H. Anouar, J. Gierschner, J.L. Duroux, and P. Trouillas. UV/visible spectra of natural polyphenols: a time-dependent density functional theory study. *Food Chemistry*, 131(1):79–89, 2012.

[174] O.B. Malcıoglu, A. Calzolari, R. Gebauer, D. Varsano, and S. Baroni. Dielectric and thermal effects on the optical properties of natural dyes: a case study on solvated cyanin. *Journal of the American Chemical Society*, 2011.

[175] F.T. Wolf. Absorption spectra of the anthocyanin pigment of red cabbage: a natural wide-range pH indicator. *Physiologia Plantarum*, 9(4):559–566, 1956.

[176] S. Meng, J. Ren, and E. Kaxiras. Natural dyes adsorbed on TiO_2 nanowire for photovoltaic applications: enhanced light absorption and ultrafast electron injection. *Nano Letters*, 8(10):3266–3272, 2008.

[177] B. Liu and E.S. Aydil. Growth of oriented single-crystalline rutile TiO_2 nanorods on transparent conducting substrates for dye-sensitized solar cells. *Journal of the American Chemical Society*, 131(11):3985–3990, 2009.

[178] C.Y. Yuan and D. Dornfeld. Integrated sustainability analysis of atomic layer deposition for microelectronics manufacturing. *Journal of Manufacturing Science and Engineering*, 132(3):030918, 2010.